AD-A186 441 INTERFACE CHARACTERISTICS AND THE MECHANICAL PROPERTIES 1/2
OF METAL MATRIX C..(U) TEXAS UNIV AT AUSTIN CENTER FOR
MATERIALS SCIENCE AND ENGINEE.. H L MARCUS ET AL.
UNCLASSIFIED 28 SEP 87 UTCMSE-87-3 N00014-84-K-0687 F/G 11/4 NL

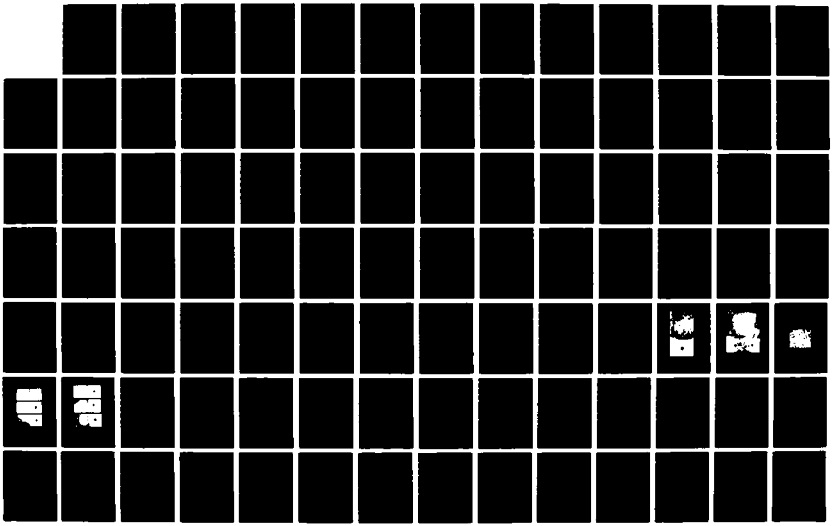

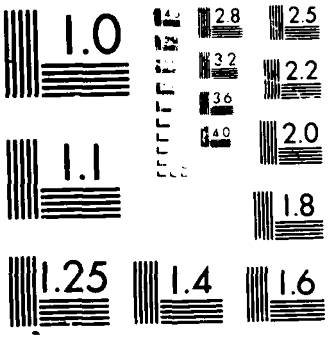
1.0
2.8
2.5
3.2
2.2
3.6
4.0
2.0
1.1
1.8
1.25
1.4
1.6

AD-A186 441

DTIC FILE COPY

(12)

Materials Science and Engineering

The University of Texas at Austin

INTERFACE CHARACTERISTICS AND THE MECHANICAL PROPERTIES OF METAL MATRIX COMPOSITES

UTCMSE-87-3
Technical Report

Office of Naval Research
Contract N00014-84-K-0687

PRINCIPAL INVESTIGATORS: HARRIS L. MARCUS AND LLEWELLYN K. RABENBERG

Mechanical Engineering/Center for Materials Science and Engineering

---

[illegible] has been approved
[illegible] and sale; its
[illegible] nlimited.

DTIC
ELECTE
OCT 2 0 1987
A

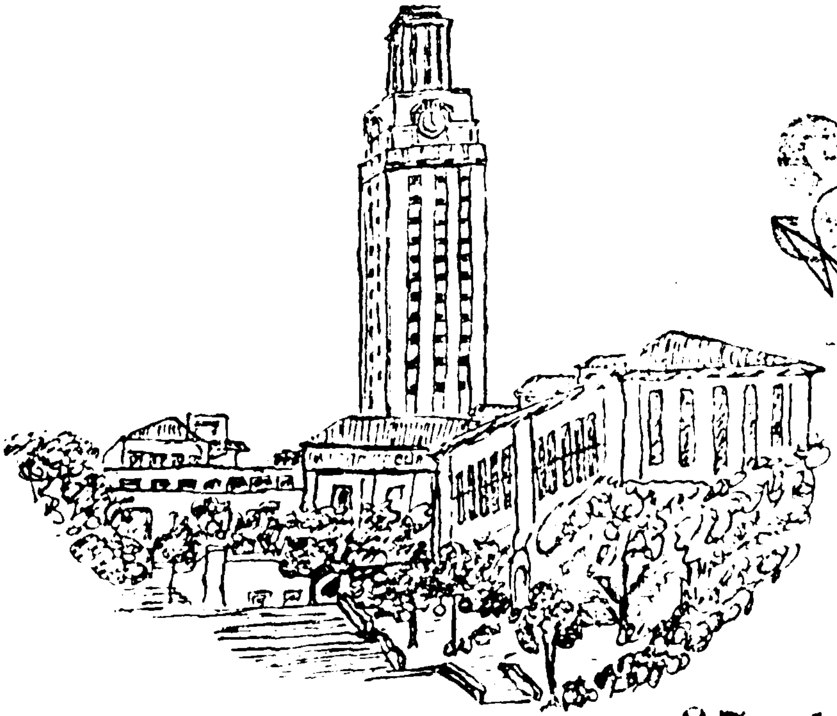

87 10 19 086

SECURITY CLASSIFICATION OF THIS PAGE (*When Data Entered*)

REPORT DOCUMENTATION PAGE	READ INSTRUCTIONS BEFORE COMPLETING FORM
1. REPORT NUMBER UTCMSE-87-3	2. GOVT ACCESSION NO.
	3. RECIPIENT'S CATALOG NUMBER
4. TITLE (*and Subtitle*) Interface Characteristics and the Mechanical Properties of Metal Matrix Composites	5. TYPE OF REPORT & PERIOD COVERED Technical Report 1 AUG 84 to 31 JUL 87
	6. PERFORMING ORG. REPORT NUMBER
7. AUTHOR(*s*) Harris L. Marcus and Llewellyn K. Rabenberg	8. CONTRACT OR GRANT NUMBER(*s*) DARPA/ONR N00014-84-K-0687
9. PERFORMING ORGANIZATION NAME AND ADDRESS The University of Texas Mechanical Eng./ Center for Materials Science & Eng. ETC 5.160, Austin, TX 78712	10. PROGRAM ELEMENT, PROJECT, TASK AREA & WORK UNIT NUMBERS
11. CONTROLLING OFFICE NAME AND ADDRESS Dr. Philip Parrish (DARPA) 1400 Wilson Blvd. Arlington, VA 22209	12. REPORT DATE September 28, 1987
	13. NUMBER OF PAGES 169
14. MONITORING AGENCY NAME & ADDRESS(*if different from Controlling Office*) Dr. Steve Fishman Office of Naval Research Department of the Navy Arlington, VA 22217	15. SECURITY CLASS. (*of this report*)
	15a. DECLASSIFICATION DOWNGRADING SCHEDULE

16. DISTRIBUTION STATEMENT (*of this Report*)

Approved for public release; Distribution unlimited.

17. DISTRIBUTION STATEMENT (*of the abstract entered in Block 20, if different from Report*)

18. SUPPLEMENTARY NOTES

19. KEY WORDS (*Continue on reverse side if necessary and identify by block number*)

Auger Electron Spectroscopy, Interface Characteristics, Interface Fracture, Scanning Auger Microscopy, I/V Switching, Metal Matrix Composites, Aluminum/Graphite Composites, Residual Stresses, X-Ray Diffraction, Raman Spectroscopy, Graphite Oxidation, Aluminum Oxide Catalysts

20. ABSTRACT (*Continue on reverse side if necessary and identify by block number*)

The research reported here is concerned with the relationships between interface characteristics and mechanical properties of metal matrix composites. Because composite interfaces are, in general, complex non-equilibrium structures, this research has emphasized the use of simplified, model specimens and direct characterization techniques to extract a range of information from the interfaces themselves.

DD FORM 1 JAN 73 1473 EDITION OF 1 NOV 65 IS OBSOLETE

SECURITY CLASSIFICATION OF THIS PAGE (When Data Entered)

This research has shown that the previously observed relationship between interface electrical conductivity and fracture path locus is complicated by the presence of impurities and by a variety of different interfacial structures. Fracture of an Al/Graphite interface through the graphite has been observed to have the highest fracture stress. The reaction of Al and graphite to form aluminum carbide has been shown to be catalyzed by the presence of a very thin film of Al oxide. This Al oxide removes electrons from C-C bonds within the graphite, increasing the rate of breakdown of the graphite. Residual stresses in Al/Graphite composites were measured by conventional x-ray techniques, and laser Raman spectroscopy has been shown to be able to characterize stress states in the vicinity of the interface of laminate aluminum/quartz composites. The interfaces in rapidly consolidated Al/discontinuous SiC have been characterized and the effects of rigid inclusions (discontinous SiC reinforcement) on precipitation kinetics are being delineated.

TABLE OF CONTENTS

Page		
1	I.	Introduction
2	II.	Electrostatic Adhesion and Cohesion at the Al/Graphite Interface
4	III.	Oxidation Model of Interface Reactions in Al/Graphite Composites
5	IV.	Residual Stresses
5	V.	Effects of Reinforcement on the Aging Response of the Matrix
6	VI.	High Energy-High Rate Powder Processing of Aluminum/Silicon Carbide Metal Matrix Composites
9	Appendix A	Metal Matrix Interfaces and Their Impact on the Mechanical Behavior of Composites
18	Appendix B	Interfaces in Aluminum Metal Matrix Composites
28	Appendix C	Interface Failure in Planar Aluminum-Graphite Composites
34	Appendix D	Electrical and Mechanical Characterization of Al/AlO_x/Graphite Planar Composites
47	Appendix E	Oxidation Model of Interface Reactions in Aluminum/Graphite Composites
53	Appendix F	Influence of Aluminum Oxide on the Formation of Aluminum Carbide in the Aluminum-Carbon System
69	Appendix G	Residual Stresses in Composite Materials: An Overview of Measurements Used
92	Appendix H	Raman Microprobe Measurements of Residual Stresses at the Interfaces
111	Appendix I	A Theoretical Investigation of Accelerated Aging in Metal-Matrix Composites
145	Appendix J	A Theoretical and Experimental Study of 6061 Al-SiC MMC to Identify the Operative Mechanism for Accelerated Aging
160	Appendix K	High Energy-High Rate Powder Processing of Aluminum/Silicon Carbicle Composites

Interface Characteristics and the Mechanical Properties of Metal Matrix Composites

I. Introduction

This is the third and final report on this research program that has as its overall objective to detail how conditions at the interfaces influence mechanical properties of metal matrix composites (MMC). This program has been funded by DARPA and monitored by ONR.

Throughout the experimental program there has been a heavy emphasis on modelling and directly probing various aspects of composite interfaces using a variety of experimental techniques, including AES, STEM, TEM, I/V and dynamic capacitance measurements, x-ray and laser-Raman residual stress measurements, and mechanical evaluation. This heavy emphasis on experimental probes was motivated by the fact that interfaces are complex, non-equilibrium structures, and that a range of information describing the interfaces is required before their influence on mechanical properties can begin to be comprehended. The information required includes such things as the chemistry at the interface, the crystal structures of interface phases, residual stresses across the interfaces, the thermomechanical history of the matrix adjacent to the interface and how all of these affect the cohesive strength and energy of the interface.

The bulk of the effort has concentrated on the Al/Graphite system, both in the form of composites and in the form of planar model specimens. The Al/discontinuous SiC system has also been examined and residual stress measurements have been made on Al/quartz composites.

Several interfacial phenomena have been investigated throughout the duration of this program. The dependence of fracture characteristics on interface electrical conductivity has been studied by first proposing an experimentally testable model and then by building a system to test it. The relationship between bonding and interfacial chemical reactivity has been investigated by observing the effects dopant elements have on the interfacial reaction zone. A third effort has been directed toward the characterization of residual stresses at interfaces. The effects of interfacial incompatibility strains on the metallurgical development of the matrix has been studied, and the interfaces in rapidly consolidated Al/discontinuous SiC composites have been characterized. Several of these ideas have been reviewed (Appendix A & B). In the next few pages they will be briefly summarized.

II. Electrostatic Adhesion and Cohesion at the Al/Graphite Interface

A major effort throughout this program has been to develop a detailed quantitative model of adhesion and bonding at the Al/Graphite interface (Appendix C), and then to use the model to direct the design of an experimental apparatus which can be used to thoroughly test the model. The model which has been developed takes into account the following observations: 1) The bond between Al and graphite is intrinsically weak; it seems to involve no primary chemical bonds. 2) A structurally disordered, possibly hydrated aluminum oxide film is present at the interface. 3) If the electrical conductivity across the interface is high, fracture occurs at the oxide-graphite interface or through the graphite. If the conductivity is low, cracks prefer to propagate through the oxide. Applying a large electric field across the interface can cause it to switch from the low conductivity state to the high conductivity state and, correspondingly, to alter the path of the crack. The proposed model explains these observations in terms of a space charge accumulation across the interface due to charge transfer from the graphite to the oxide; this space charge results in an electrostatic attraction between the oxide and graphite of magnitude in the range 4 kPa to 400 kPa, the actual value depending on the density of charge traps in the oxide. Since the measured force of adhesion across a low conductivity oxide is approximately 20 kPa, the prediction seems to be in the correct range. In addition to this direct electrostatic attraction, the space charge establishes an electric field of approximately 10^5 volts/cm across the oxide; a field of this magnitude can significantly polarize the charged defects in the oxide, possibly weakening it mechanically. Thus, a strong attraction exists between the weakened oxide and the graphite in the low conductivity state, and fracture occurs through the oxide. Conversely, if a large voltage is applied across the oxide, it is switched to the high conductivity state, allowing the space charge to be depleted. The electrostatic force of adhesion is reduced, and fracture tends to occur along the oxide-graphite interface. In this way, the model predicts that the mechanical properties of the interfacial zone depend on the density and electrical activity of defect states within the oxide; these states may be due to structural defects or chemical impurities, especially OH^- or H^+ ions.

The basic ideas used in the model of adhesion have been used to direct the development of an experimental apparatus designed to test the model. This consists of a computer-controlled a.c. and d.c. impedance measuring system which is used to measure and control the interface electrical properties during mechanical testing. This apparatus measures I/V characteristics of planar specimens to determine whether they are in the high, or low, conductivity states. It is capable of dynamic capacitance measurements to determine the density and distribution of electrically active charge traps in the oxide. The specimens are created and mechanically tested in the same atmosphere-controlled chamber which is used for the electrical tests.

Some of the fracture tests are performed in a special fracture stage in situ in the scanning Auger microprobe. This allows electrical characterization of the interface before fracture and fracture surface chemical analysis on both exposed surfaces after fracture.

The experimental results from the electrical charcterization system show that the interface in the Al/Al oxide/Graphite laminate system can be characterized with either high or low conductivity. The presence of oxygen or water vapor in the gas stream in the deposition chamber creates varying levels of resistivity, with the higher resistivity observed in the case of water in the gas stream. The fracture strength was highest in samples that fractured predominantly within the graphite. The interface switching was observed to be localized in multiple probe measurements (Appendix D).

III. Oxidation Model of Interface Reactions in Al/Graphite Composites

Regardless of the final reaction product, any chemical reaction with solid graphite must involve the breaking of C-C covalent bonds.

This idea forms the basis for the Oxidation Model of Interface Reactions in Al/Graphite Composites (Appendix E) and provides a useful paradigm on which to base a series of experiments into the chemical reactions which occur at the Al-C interface. The aim of the experiments is to understand and possibly control the reactions between Al and C which occur during high temperature processing of Al/graphite composites.

The oxidation model suggests that the electrophyllic nature of Al or its oxides causes transfer of electrons form subsurface C-C bonds, effectively catalyzing the breakdown of the graphite. It also identifies certain species which will stabilize graphite, poisoning any carbide-forming reaction. Thus, it provides a conceptual basis for processes aimed at improving the high temperature stability of Al/G composites.

To test these hypotheses, planar specimens have been made, reacted, and examined in STEM and AES. The planar specimens are made by depositing Al and/or Al oxide on thin carbon films, modifying the interface by deposition of suitable elements or compounds and then depositing an overlayer of carbon to "sandwich" the specimen and prevent contamination. These thin sandwich specimens are examined in STEM to determine the extent and morphology of carbide formation.

The experiments have shown that the presence of a very thin, or a non-continuous film of aluminum oxide between Al and amorphous carbon catalyzes the breakdown of the carbon and allows reaction with the Al to form aluminum carbide (Al_4C_3) (Appendix F).

However, if the oxide is thick (> 200Å) and continuous, it acts as a barrier to diffusion and limits the rate of reaction.

IV. Residual Stresses

In addition to the electrical and chemical aspects of composite interfaces as discussed above, the mechanical properties of composite interfaces certainly depend on their state of residual stress (Appendix G). Residual stresses are formed in composites during processing or in service due to thermal strain incompatibilities between matrix and reinforcing phase. They are superimposed on any applied stresses to yield the complete state of stress of the composite; thus, their effect on mechanical properties is straightforward and direct. Unfortunately, they are not easily measured.

Because measurement of residual stresses is difficult, a significant effort has been directed toward devising new methods for their characterization. In particular, the feasibility of using a laser-Raman microprobe to measure residual stresses has been examined. For the planar model system of Al on quartz, residual stresses are detectable and measurable (Appendix H).

V. Effects of Reinforcement Phase on the Aging Response of the Matrix

The presence of a hard, nondeformable phase within a ductile metallic matrix can have effects on the metallurgical development of the matrix. For the case of discontinuous SiC fibers in an age-hardening matrix, the thermal expansion mismatch between fiber and matrix can lead to plastic flow of the matrix during homogenize-and-quench treatments. The resulting dislocation field around each SiC particle enhances diffusivity of substitutional elements, shortening the time for peak aging. In addition, the dislocations provide heterogeneous nucleation sites for the precipitation process, and so effect the overall transformation kinetics (Appendix J). The plastic strain fields around discontinuous SiC fibers of varying lengths are being computed and used to model the effects of plastic deformation on precipitation kinetics. The models reasonably predict the overall transformation curves as measured calorimetrically.

VI. High Energy-High Rate Powder Processing of Aluminum/Silicon Carbide Metal Matrix Composites

Discontinuous, silicon carbide reinforced, aluminum metal-matrix composite metals were made by consolidating powder constituents using a novel high energy-high rate process which employs a fast-rising high-current pulse. The powder mixtures were contained in an insulated die, under pressure, and were rapidly densified during the discharge from a homopolar generator, in a processing time of about one second. Several types of rapidly solidified Al-based powders, X7091, CW67 and 7064 were reinforced with different types and volume fractions of discontinuous SiC. The consolidated materials were evaluated using optical and analytical electron microscopy and Auger spectroscopy to determine the microstructure and to identify the phases evolved.
Processing/structure/property interrelationships were established. Energy inputs of 400 kJ/kg to 2,500 kJ/kg at applied pressures of 105 to 315 MPa resulted in consolidated forms, having a homogeneous distribution of the SiC particles within the composite. Densities of 95% to 99% of theoretical were obtained with local interparticle melting contributing to densification at the highest energy levels. A direct correlation exists between the density, hardness and fracture tensile strength, and the specific input energy, indicating that metallurgical bonding and densification scaled with input energy. Materials consolidated at specific input energy under 400 kJ/kg retained the original powder microstructure. At higher energy input the pre-existing solute-rich phase between the dendrite arms decomposes and small dispersoids are retained. Dispersoids were $(Co, Fe)_2$

Al_9 and $(Ni, Fe)_2 Al_9$ having spherical or ellipsoidal shape with size ranging from 0.05 μm to 0.20 μm. Materials consolidated at the highest energy levels revealed fine, needleshaped precipitates identified as the metastable, coherent, η'-phase ($MgZn_2$). This structure feature is consistent with a rapid heating to high temperature - fast cooling cycle. Auger electron spectroscopy of in-situ fracture surfaces shows metal-ceramic interface fracture associated with a 100-150 Å oxide layer, rich in Al, Mg, O and "graphitic" C. Analytical electron microscopy indicated that this layer was largely amorphous. Microcrystalline regions of the oxide were identified to most probably be γ - Al_2O_3 or the $MgAl_2O_4$ type spinel. Details are given in Appendix K.

Summary

The research reported here has applied a variety of tools and techniques to the characterization of composite interfaces. This has allowed several interfacial phenomena to be described. The effects of oxide phases and impurities on the electrical resistivity of Al/graphite interfaces has been described. This careful characterization of interface charges and their effects is allowing the mechanical properties to be more fully comprehended. The catalytic action of Al oxide on the breakdown of carbon to form graphite has been demonstrated. Significant progress has been made in the characterization of residual stresses in composites. The effects of interface incompatibility and plastic flow on matrix metallurgy has been investigated. Finally, the interfacial character of rapidly consolidated Al-SiC has been investigated.

Appendices

A. L. D. Brown, B. Maruyama, Y. M. Cheong, L. K. Rabenberg, and H. L. Marcus, "Metal Matrix Interfaces and Their Impact on the Mechanical Behavior of Composites," Composite Interfaces, Vol. I, H. Ishida and J. L. Koenig, eds., (Elsevier Science Publishing Co., New York, 1986), p. 27.

B. H. L. Marcus, L. Rabenberg, L. D. Brown, G. Elkabir, and Y. M. Cheong, "Interfaces in Metal Matrix Composites," Proc. of the Sixth International Conference on Composite Materials/Second European Conference on Composite Materials ICCM VI/ECCM 2. (Elsevier Science Publishers, Amsterdam), Vol. 2, p. 2.459.

C. L. D. Brown, C. L. Grove, and H. L. Marcus, "Interface Failure in Planar Aluminum-Graphite Composites" in Interfaces in Metal Matrix Composites, A. K. Dhingra and S. G. Fishman eds. (AIME, Warrendale, 1986), p. 205.

D. L. D. Brown and H. L. Marcus, "Electrical and Mechanical Characterization of Al/AlO_x/Graphite Planar Composites."

E. B. Maruyama and L. Rabenberg, "Oxidation Model of Interface Reactions in Aluminum/Graphite Composites" in Interfaces in Metal Matrix Composites, A. K. Dhingra and S. G. Fishman eds. (AIME, Warrendale, 1986), p. 233.

F. B. Maruyama, L. D. Brown and L. Rabenberg, "Influence of Aluminum Oxide on the Formation of Aluminum Carbide in the Aluminum-Carbon System."

G. Yong-Moo Cheong and H. L. Marcus, "Residual Stresses in Composite Materials: An Overview of Measurements Used" in Advances in Surface Treatments, Vol. IV: "Residual Stresses." (Pergamon Press, N.Y., 1986), p. 115.

H. Y. M. Cheong, H. L. Marcus and F. Adar, "Raman Microprobe Measurements of Residual Stresses at the Interfaces" in Interfaces in Metal-Matrix Composites, A. K. Dhingra and S. G. Fishman, eds., (AIME, Warrendale, 1986), p. 147.

I. I. Dutta, D. L. Bourell and D. Latimer, "A Theoretical Investigation of Accelerated Aging in Metal-Matrix Composites." Submitted to J. Composite Materials.

J. I. Dutta and D. L. Bourell, "A Theoretical and Experimental Study of 6061 Al-SiC MMC to Identify the Operative Mechanism for Acclerated Aging."

K. G. Elkabir, C. Persad and H. L. Marcus, "High Energy-High Rate Powder Processing of Aluminum/Silicon Carbide Metal Matrix Composites."

APPENDIX A

METAL MATRIX INTERFACES AND THEIR IMPACT ON THE MECHANICAL BEHVIOR OF COMPOSITES

L.D. BROWN, B. MARUYAMA, Y.M. CHEONG, L.K. RABENBERG, AND H.L. MARCUS
Center for Materials Science and Engineering, Mechanical Engineering Department, The University of Texas, Austin, TX 78712

ABSTRACT

This paper will review the status of our understanding of the role the interface plays in the mechanical behavior of several metal matrix composites, MMC. The paper will include the fatigue crack propagation in Ti MMCs in terms of interface diffusion under isthermal and thermal cycling conditions; the role of the interfacial oxide in Al/Graphite in terms of its electrical state and its reactivity with graphite; the lack of a reaction zone in Al/SiC and its effect on failure path; and the state of residual stresses in MMCs. It is our point of view that optimum MMC properties are achieved by closely controlling and generally obtaining a reaction zone of optimum thickness at the interface.

INTRODUCTION

Metal matrix composites (MMC) are characterized by anisotropy, heterogeneity, and interfaces. As one investigates the attractive properties possible with MMCs one also becomes increasingly aware of the complexities associated with their character. Within this paper will be discussed a range of approaches used at the University of Texas to unravel some of the complexities associated with the MMC. The aluminum and the titanium matrices will be discussed in some detail.

For the Ti-MMC, the influence of various environments on the fracture and fatigue crack propagation behavior of the composites will be discussed. The primary emphasis is on observations that relate to the interactions between the matrix, the interface, and the environment. The environments studied here are vacuum, humid air, dry nitrogen, and sulfur.

In the Al-MMC, the emphasis will be the nature of the interface in the Al/Graphite system. Model laminate systems are used to simulate the actual fiber composite interfaces. This enables a systematic study of composite interfaces which cannot be achieved in the "as-fabricated" composite. The topics of discussion will be the electrical character of the interface, its relation to the interface's fracture behavior, and factors that impact the kinetics of interface reactions. Al/SiC discontinuous fiber composites will also be discussed with reference to the primary fracture path.

Measurement of residual stresses which originate due to the expansion coefficient mismatch of composite components will also be considered. In all the above the primary emphasis will be on the influence of the interface on the mechanical behavior of the MMC.

Titanium MMCs

The effects of environment on the Ti-6Al-4V/Boron and the Ti-6Al-4V/SiC composite systems illustrates the complex nature of the matrix-fiber interface by elucidation of the interactions between the matrix,

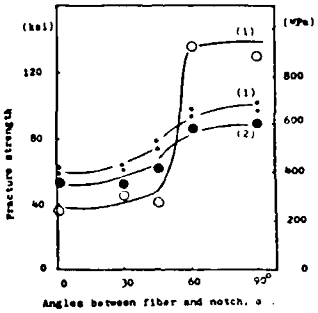

FIG. 1. Fracture strength of Ti-6Al-4V/SiC vs. loading angle (longitudinal, α = 90°; transverse, α = 0°) [from ref. 2]
o - as-received
* - isothermal heat treatment, 550°C/10 days
● - thermally cycled treatment,550°C/10 days

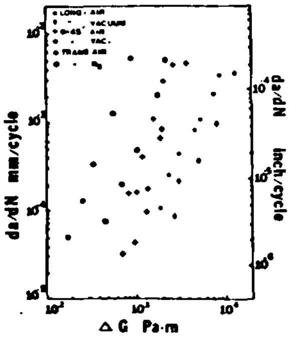

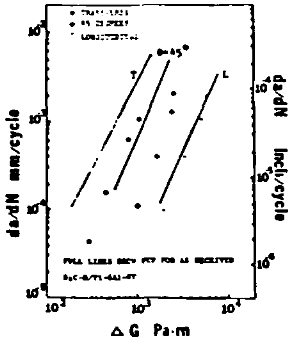

FIG. 2. Mixed Mode FCP for as-received Ti-6Al-4V B_4C-B in environments of different relative humidities (R - 0.1) [from ref. 1]

FIG. 3. Mixed mode FCP for Ti-6A-4V/B_4C-C heat treatment at 885°C/6 hours in vacuum, tested in humid air (R - 0.1) [from ref. 1]

the fiber, and the environment. Longitudinal and transverse failure modes, failure stress, and fatigue crack propagation in these two MMC systems were measured in vacuum, humid air, and dry nitrogen environments [1]. The effects of isothermal and thermally cycled heat treatments on the mechanical properties were also investigated [2]. The most general observation from these studies is that any heat treatment on the titanium based MMCs substantially degrades the MMC's longitudinal strength while not significantly affecting the already poor transverse strength. This is shown in Fig 1. Similar results are observed in many other MMC systems [3]. The degradation is directly attributable to interactions at the matrix-fiber interface. However, the less reactive the heat treating environment (i.e. vacuum), the less the effect on the MMC's longitudinal strength. The interaction between testing environments and heat treatments is not so easily generalized.

Fatigue crack propagation (FCP) of Ti-6Al-4V/Boron in both longitudinal and mixed mode loading is affected by heat treatments and environments. When a humid testing environment was used, the FCP increased relative to that in an inert testing environment. The increase is most noticeable in off-axis loading as seen in Fig. 2. After heat treatment in vacuum or humid air and subsequent testing in humid air, the FCP was *reduced relative to as-fabricated specimens*. Fig. 3 shows that the decrease in FCP becomes more pronounced with greater off-axis loading. The $\Delta\mathcal{G}$ is the combined mixed mode energy which is more convenient to use than the stress intensity factor, ΔK, in mixed mode fatigue crack growth research.

Insight into the origins of these interactions was acquired through investigation of the modes of failure in these MMCs. Scanning electron microscopy and scanning auger microscopy revealed that the vacuum and the humid air heat treated composites tested in humid air failed predominantly along the matrix-fiber interface. For the as-fabricated composite tested in humid air, the failure mode was by both interface failure and a great deal of fiber splitting consistent with a strong interface. Fatigue crack closure test indicated that in the humid testing environment the freshly exposed plastically deformed titanium matrix oxidizes and compresses the boron or SiC fiber upon crack closure. This results in damage to the brittle fibers. Secondary cracks were observed in the failure paths of the heat treated composites suggesting an enhanced matrix-fiber interfacial bond which is not as easily susceptible to oxidation. Reduced-susceptibility of the failure path to oxidation through an interfacial reaction resulted in better fatigue resistance.

In contrast, after thermally cycled heat treatments in sulfur, a Ti-6Al-4V/B_4C-B composite's FCP was greater when tested in humid air than when fatigued in dry nitrogen. An explanation for this behavior requires a closer examination of the matrix-fiber interface [2]. The penetration of sulfur into the matrix from the matrix-fiber interface is much greater for thermal cycling than for isothermal heat treatments in sulfur. This is shown in Fig 4. This in itself might be explained in terms of plastic deformation of the matrix during thermal fatigue due to differences in the coefficient of thermal expansion of the matrix and the fiber. Active dislocation motion would facilitate transport of sulfur into the matrix. Little sulfur was detected on the fiber side of the interface after failure in humid environments indicating a complete loss of adhesion at the matrix-fiber interface. As a result, the failure load was carried solely by the matrix. An interaction between hydrogen and the sulfur is suspected but not as yet determined.

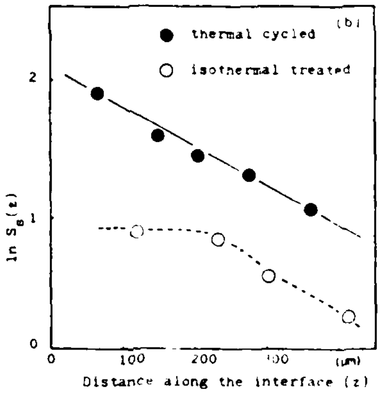

FIG. 4. Sulfur concentration on matrix side of Ti-6A-4V/SiC heat treated in sulfur vs. distance from free surface [from ref. 2].

The interface in titanium composites, as well as many others, appears to be a preferential diffusion sink for all impurities associated with the matrix, the fiber, the processing, and the environment. In the titanium system, various forms of titanium carbides, titanium borides, titanium oxides, titanium sulfides, and calcium have been observed in various morphologies and concentrations varying with matrix microstructures and fiber treatment [2,4]. A better understanding of the nature of the matrix-fiber interface through careful systematic studies is clearly needed.

Aluminum MMCs

The Al/Graphite MMC system is plagued by poor interfacial properties. Poor wettability, poor bonding, and a high instability of the interface on heat treatment result in less than optimum physical properties. In order to explore the interface properties more fundamentally, research at the University of Texas has keyed on observations of the interface subjected to electrical, thermal, and chemical perturbation. In particular, the topics discussed here will be the correlation between the electronic nature of the interface and the interface's locus of failure; an oxidation model of matrix-fiber reactions and chemical treatments to control interfacial reations; and the reaction zone in Al/SiC composites.

During the study of fiber-matrix interfacial characteristics in Al/Graphite MMCs, a correlation between the electrical state of a planar Al/Al oxide/Graphite model and its failure mode in tension was observed [5,6]. As shown in Fig. 5, when the aluminum oxide in the planar model was in a high impedance electrical state, failure occured by fracture through the oxide. However, the oxide could be voltage switched to a low impedance electrical state where failure occured by fracture through the graphite-oxide interface or through the graphite. An oxide previously in the low impedance state would relax to its original high impedance state over a period of time and failure occured again by fracture through the oxide.

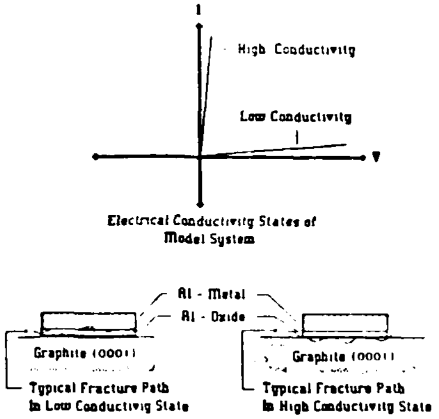
I
High Conductivity
Low Conductivity
V
Electrical Conductivity States of Model System
Al - Metal
Al - Oxide
Graphite (0001)
Graphite (0001)
Typical Fracture Path In Low Conductivity State
Typical Fracture Path In High Conductivity State

FIG. 5. Schematic representation of the electrical state vs. locus of failure in model Al/Al oxide/Graphite thin film composites.

A macroscopic model utilizing electrostatic forces has been proposed to account for this observed phenomena [7]. When the mechanical interaction between a dielectric and an electric field is not a first order effect (e.g. *piezoelectric, ferroelectric,* etc.), there is a second order interaction which is proportional to the field squared. For this effect to be appreciable, the electric field must be on the order of 10^5V/cm. It is not necessary to apply a voltage across the planar model to produce this field. It may arise as a natural consequence of charge transfer between the disordered oxide and the aluminum or the graphite. The charge is believed to be localized within 5nm of the respective interface. Due to the trapped charge, the compressive stresses across the interface may be as large as 500 kPa. As the graphite-oxide interface is fairly non-reactive in comparison to the oxide-aluminum interface, this stress may be the determining factor between failure at the interface or failure in the inherently weak disordered oxide. Experiments are currently underway to investigate the phenomena and test this model's validity.

Aluminum carbide forms at aluminum-graphite interfaces in these MMCs when heated above 500°C [8-10]. The formation of aluminum carbide is detrimental to the composite's strength, as seen in Fig. 6, because of stress concentrations both at surface pits formed in the consumption of the graphite and at the sharp aluminum carbide crystals. The kinetics of the reaction are believed to be accurately described by the analogous process of oxidation of graphite in air [11]. Furthermore, the role of various species in enhancing or diminishing the reactivity as well as wettability can be described by analogy to air oxidation.

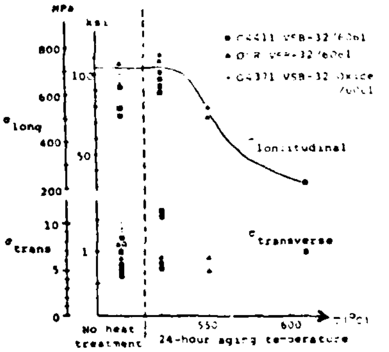

FIG. 6. Fracture strength of Al(6061)/Graphite heat treatment temperature (rough vacuum environment) [from ref. 10]

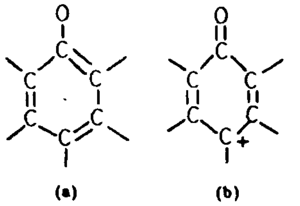

FIG. 7. Air oxidation model of graphite [from ref. 9]
(a) graphite stable
(b) graphite unstable, CO stable

The pertinent step in the oxidation of graphite in air is the transition from oxygen chemisorbed onto active sites on the graphite surface edge to carbon monoxide chemisorbed on the surface edge of graphite [12-14], as seen in Fig. 7. Notice that the transition is accomplished by transferring an electron from the matrix to the carbon-oxygen pair [13]. This results in a severe weakening of the bond between the surface carbon atom and the matrix. The stability of either bonding structure (a) or (b) and therefore the reactivity can be altered by modifying the interaction of oxygen with other compounds. A metal oxide, for example will increase the electrophilic nature of the oxygen, thus stabilizing bond configuration (b) and increasing the rate of oxidation. At an aluminum-graphite interface, the oxygen is present in the form of a free radical of aluminum oxide which might subsequently transform into aluminum oxycarbide. In contrast, the stabilization of bond configuration (a) should lead to a decrease in the reactivity. This can be accomplished by treating the graphite with phosphorus and/or boron [12]. The degree of the influence of these substances on the oxidation rate of graphite in air is shown in Table 1. An alternate

TABLE I. Oxidation rates of graphite in air at 700°C [From ref. 9].

Additive	Rate (hr^{-1})	Rate Rel. to Pure Graphite
None	0.072	1.0
Al	0.118	1.64
Al_2O_3	0.181	2.52
B	0.032	0.44
B_2O_3	0.033	0.46
P	0.017	0.24
P_2O_5	0.016	0.23

0.1 mole per cent added to graphite powder.

method of stabilizing configuration (a) is by increasing the electrophilic nature of the graphite by using an acceptor intercalation compound. Intercalated graphite compounds are also known to have reduced oxidation rates. [15].

Applying these ideas to the practical application of Ti_2B to graphite, one may infer from this discussion that the success of TiB_2 as wetting agent and a reaction inhibitor may be related to its ability to mediate the strength of the carbon-oxygen bond to a level which enhances wettability and diminishes reactivity. Furthermore, better bonding and interface integrity may be achieved by placing boron and/or phosphorus compounds at the interface either by a fiber coating or by dissolution in the matrix and/or the fiber [11]. Intercalation compounds of graphite may achieve the same results.

In Al/SiC discontinous fiber MMCs, the aluminum matrix and the SiC fiber are much less reactive at the interface. The reaction zone is atomistic in extent with only a scattered presence of gamma-Al_2O_3 after a 550°C heat treatment in a vacuum of 10 millitorr [16]. There is evidence of some degradation at 600°C [17]. Auger analysis of in-situ fractured material indicates a strong aluminum-SiC interface. The fresh failure path was primarily aluminum and substantial sputtering was required to detect the average composition of silicon or carbon. It should be noted that this interface strength is a function of the processing used. These observations are consistent with the point of view that the optimum MMC properties are achieved by closely controlling and in general obtaining a reaction zone of optimum thickness at the interface. This is system dependent.

Residual Stress Measurements

The stress at the interface between the matrix and the fiber have been known to influence the mechanical properties of composites [10]. A large residual stress is believed to originate from the difference of thermal expansion coefficients between fiber and the matrix. Plastic flow is expected in the vicinity of the interface if the thermally induced stresses are well above the yield strength of the matrix. Calculations indicate this may be the case in the Al/Graphite composite system. [18]. X-ray diffraction by the $\sin^2\psi$ method was used for the measurement of residual stresses in the aluminum metal matrix of this MMC system [19]. Large longitudinal residual stresses, approximately 200 MPa, were obtained. These residual stresses were reduced approximately 30% by quenching the composite in liquid nitrogen and measuring the stresses at room temperature. Additional plastic deformation in the aluminum matrix, during cooling occurs and the elastic relaxation on returning to room temperature may explain these results. It is important to note that only volume average stresses can be measured by the x-ray diffraction method because the x-ray penetration depths, approximately 50 microns for aluminum, are greater than the average distance between the fibers. However, stresses at the interface are expected to be different from the volume average stress. The thermal mismatch is at the interface, but the fixed strain conditions at the composite boundary would tend to volume average the residual stress patterns.

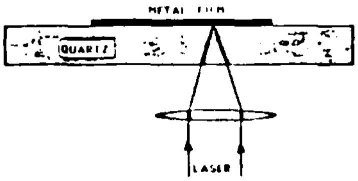

FIG. 8. Schematic of Raman microprobe analysis [from ref. 21].

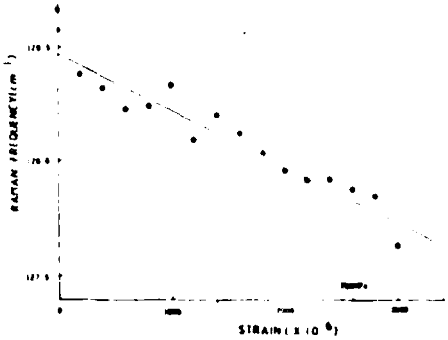

FIG. 9. Strain vs. Raman frequency shift calibration for quartz plate in four-point bending [from ref. 21]

Raman microprobe analysis, as shown schematically in Fig. 8, can be used for the measurement of localized residual stresses at interfaces in Raman active materials. Raman spectroscopy is sensitive to the respective surfaces or interfaces and the laser beam can provide a one micron resolution. Shifts in the frequency of the reflected beam are proportional to the surface strain. This has been formulated theoretically [20] and demonstrated experimentally, as seen in Fig. 9. In this way, localized residual stresses can be measured.

For the further development of the Raman microprobe technique, the aluminum/quartz system has been used [21]. A linear relation between the Raman shift and strains was obtained on a quartz plate using strain guages and a four-point bending jig. This calibration was shown in Fig. 9. After thermal evaporation of aluminum onto the quartz plate, residual tensile stresses, in the range of 250MPa - 350MPa, were determined to exist at the aluminum-quartz interface. The technique of using the Raman microprobe to investigate residual stresses at interfaces in systems containing Raman active components is undergoing further development at the University of Texas.

CONCLUSION

Metal matrix composites are characterized by anisotropy, heterogeneity, and interfaces. The matrix-fiber interface thickness and composition affect the overall mechanical strength of the MMC. Uncontrolled interfacial reactions initiate stress concentrations, enhance parallel and perpendicular diffusion between the matrix and the environment; and generally degrade a MMC's mechanical properties. The heat treatment environment, the heat treatment technique, and the testing environment also affect the observed mechanical properties. The interface is also responsible for complex residual stress states which are not easily characterized.

Several models and techniques for measuring and modifying the characteristics of the interface have been mentioned. The thin film laminate model of the interface has allowed a systematic study of the interface's diverse character. This would be difficult with "as-fabricated" composites due to the interfacial character. It is not possible to discuss each topic presented in adequate detail due to space limitations. It is hoped that interested readers may find sufficient detail in the references. In any event, composite interfaces will provide a fruitful area of research, both basic and applied, for years to come.

ACKNOWLEDGMENT

The authors would like to thank the many investigators whose diligent research made this overview possible. The overview was written with financial support by the DARPA under ONR contract N00014-84-K-0687.

REFERENCES

1. D.S. Mahulikar, Ph.D. Dissertation, The University of Texas, 1981.
2. Y.H. Park, Ph.D. Dissertation, The University of Texas, 1983.
3. A.G. Metcalfe, Interfaces in Metal Matrix Composites, Vol 1 (Academic Press, 1974).
4. C.G. Rhodes and R.A. Spurling, ASTM STP 864, *Philadelphia*, 1983.
5. S.D. Tsai, Ph.D. Dissertation, The University of Texas, 1980.
6. H. Mendez, D. Finello, R. Walser and H.L. Marcus, Scripta Met., 16 (1982), 855.
7. L.D. Brown, C.L. Grove and H.L. Marcus, Composite Proceedings of Spring 1986 AIME Conference, New Orleans, LA, to be published.
8. I.H. Kohn, Met. Trans., 7A (1976), 1281.
9. Rakszawski, Parker, Carbon, 2 (1964), 53.
10. D. Finello, Ph.D. Dissertation, The University of Texas, 1982.
11. B. Maruyama, L. Rabenberg, Composite Proceedings of Spring 1986 AIME Conference, New Orleans, LA, to be published.
12. D.W. McKee, C.L. Spiro and E.J. Lamby, Carbon, 22 (1984), 285.
13. D.W. McKee, C.L. Spiro and E.J. Lamby, Carbon, 22 (1984), 507.
14. F.J. Long and K.W. Sykes, Proc. Roy. Soc. Lond., 215A (1952), 100.
15. F.L. Vogel, Intercal Corp., Port Huron, MI, Personal Communication, (1986).
16. L.J. Fu, M. Schmerling and H.L. Marcus, ASTM STP 907, 51.
17. S. Kohara, Proceedings, Japan-U.S. Conf. on Composite Materials, Tokyo, 1981, K. Kawata, T. Akasaka, Eds., 224.
18. S.D. Tsai, D. Mahulikar, H.L. Marcus, I.C. Noyan and J.B. Cohen, Matl. Sci. & Eng., 47 (1981) 145.
19. S.D. Tsai, M. Schmerling and H.L. Marcus, Residual Stress and Stress Relaxation (E. Kula and V. Weiss, Eds., 1982, 425).
20. V.J. Tekippe, A.K. Ramadas and S. Rodriguez, Phys. Rev. B, 16(8), (1977), 3815.
21. Y.M. Cheong, H.L. Marcus and F. Adar, Composite Proceedings of Spring 1986 AIME Conference, New Orleans, LA, to be published.

APPENDIX B

INTERFACES IN ALUMINUM METAL MATRIX COMPOSITES

H.L. Marcus, L. Rabenberg, L.D. Brown,
G. Elkabir and Y.M. Cheong
Department of Mechanical Engineering and
Center for Materials Science and Engineering,
The University of Texas,
Austin, TX 78712
USA

ABSTRACT

This paper describes some of the aluminum metal matrix composite research being carried out at the Center for Materials Science and Engineering at The University of Texas at Austin. Three specific subtopics are emphasized. The first subtopic describes how the electrical character of the metal/graphite interface impacts the nature of the fracture mode. The results are modeled in terms of the electrostatic forces associated with a metal-insulator-semiconductor (MIS) interface. The second part of the paper deals with the residual stresses present in the aluminum/graphite MMC and describes some x-ray measurements of the residual stresses as a function of the thermal history of the MMC. The final subject discussed is the new high energy, high rate processing method used to consolidate aluminum/SiC composites. The approach has been shown to have promise in maintaining desirable microstructures present in the aluminum powders through the consolidation process.

INTRODUCTION

The interface between the reinforcement phase and the metal matrix plays a key role in the mechanical behavior of a metal matrix composite. The fracture strength, tensile strength, fatigue and crack growth behavior in both inert and aggressive environments are all influenced by the nature of the metal matrix composite interfaces. This is true, whether the reinforcing phase is present as a continuous or as a discontinuous second phase, because it is present in large volume fractions.

Aspects of the interface that play a major role in the properties include the following. The local chemistry of the interface can have a major impact on strength of the bonding at the interface. The crystal structure or noncrystalline nature of nanometer thin, almost two dimensional phases at the interface can have a significant influence on the mechanical response of the interface. As suggested below, the electrical properties of the interface can also be reflected in the strength of the interface. Morphological features of the interface can play a significant role in the composite mechanical behavior, especially if chemical interaction takes place between the matrix and the reinforcing phase. Finally, interfacial material indirectly affects local chemistry and electrical characteristics through its effect on transport phenomena.

Another very important aspect of the interface is the fact that it represents the region of discontinuity of properties. This very obvious statement is extremely important in the determination of the resulting composite properties. It is the interface that must transfer the load between the usually lower modulus matrix into the higher elastic modulus reinforcing phase. This load transfer also raises the strength of the composite. In addition, the interface is the region where dislocations present in the ductile matrix sense the reinforcing phases which are usually not responsive to plastic deformation. This leads to both strengthening and limited ductility. From a fracture viewpoint, this condition limits the local deformation in the vicinity of a flaw and greatly reduces the fracture toughness of the composites. Differences in the coefficients of thermal expansion across the interface also have an impact on the mechanical response of the composite. Since most composites are processed at some elevated temperature, the subsequent cooling leads to a significant residual stress pattern in the composite arising from the $\Delta\alpha\Delta T$ existing at the interface. In many metal matrix composites, this can lead to residual stresses at the interface at or above the flow stress of the matrix. In addition to the above, the interface region is very often a multiple layered structure such that the discontinuities in properties may be much more complex then those defined by just considering the two primary components of the composite.

In this paper, research on three major topics associated with aluminum metal matrix composites will be described. The first will discuss the impact the conducuvity of the interface phases in aluminum graphite composites has on the fracture behavior of the interface. The second will describe measurements of residual stresses in aluminum graphite metal matrix composites. The final topic will address a new processing approach to making discontinuous Al/SiC composites from particulates using high energy high rate processing.

Interface Failure in Al/Graphite MMC

It is well-known that the interface in Al/Graphite MMCs usually has associated with it an oxide layer [1]. This oxide layer can either be non-crystalline or crystalline. The crystalline form is usually observed to be a deformed spinel crystal structure associated with the transition aluminas or oxy-carbides. It has been shown that the conductivity of the interface region can be switched from a low conductive state to a high conductive state by an applied voltage across the interface [2]. With this shift in conductivity there is a change in the fracture path from within the oxide layer to a fracture path at the interface or within the graphite [3]. The locus of failure in these thin film models is determined by Auger spectroscopy.

Fig. 1 is a schematic of the interface model used in this type of study. The sample consists of a basal plane oriented single crystal Ticonderoga graphite with 20 to 50nm of reactively evaporated oxide followed by an evaporated layer of aluminum. The conductivity is probed as shown. As the applied voltage across the sample is increased, the conductivity will switch when the electric field is sufficiently high. The character of the interface is modeled as a metal-insulator-metal (MIM) under applied voltage. The two dimensional, semi-metal nature of graphite modifies this somewhat providing lateral conduction probing of the interface. Fig. 2 shows a Metal-Insulator-Semiconductor (MIS) analogue of the interface model.

The electrical-mechanical switching characteristic of the interface is being modeled using electrostatically induced adhesive forces. These result from a space charge accumulation at the graphite-oxide interface [4]. With space charge densities of $10^{19}/cm^3$ or interface state densities of $10^{13}cm^2$, the interface can be under significant compressive stress, and the probability of crack propagation along the oxide-graphite interface is reduced. The highly defective nature of the oxide layer generates large internal field gradients acting on the hydrated oxide resulting in large crack promoting electrostatic forces. The competing interfacial and internal forces combine with the externally applied forces to induce failure within the oxide in the low conductive state. The influence of the applied field is then to continually modify the field gradients within the model structure. The applied field reduces both the decohesive force within the oxide and the adhesive force in the vicinity of the oxide-graphite interface.

If the above model does explain the failure behavior of the interface in the Al/Graphite composites, it can be used to design a "proper" interface. This would involve the choice an interface layer between the metal and the graphite that has the proper homogeneity and appropriate thickness to optimize the adhesion/cohesion behavior.

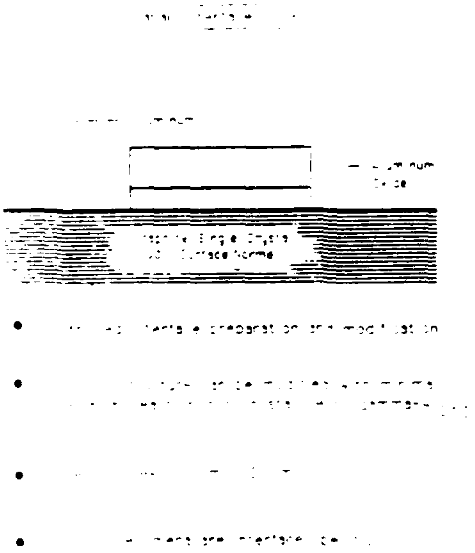

Fig. 1 Schematic diagram of the planar model of the aluminum-oxide-graphite interface.

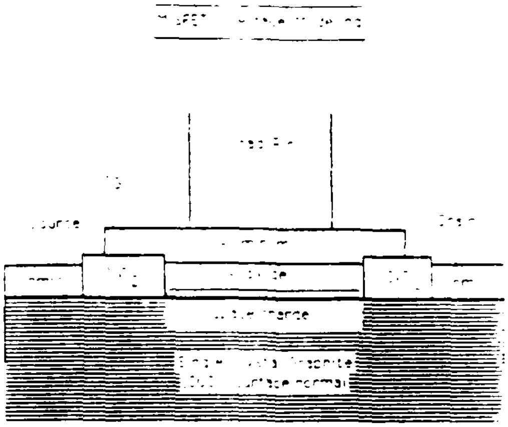

Fig. 2 Schematic diagram of the metal-insulator-semiconductor analog used to model space charge-induced failure at the oxide-graphite interface.

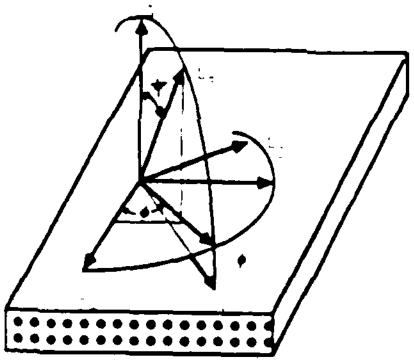

Fig. 3 Definition of the angles and orientation of the Laboratory system L_i with respect to the sample system S_i.

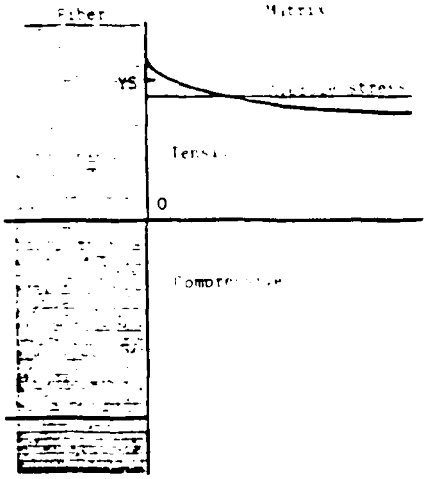

Fig. 4 Model of residual stress distribution in Metal Matrix Composites due to cooling.

RESIDUAL STRESSES IN ALUMINUM GRAPHITE METAL MATRIX COMPOSITES

The continuous graphite fiber aluminum MMC has one of the largest mismatches of coefficients of thermal expansion of any MMC. As the modulus of the graphite fibers increases to greater than 700 GPa(100 x 10^6 psi) the basal plane orientation is almost completely parallel to the axis of the fibers. This results in a well defined negative coefficient of expansion along the fiber axis. With the coefficient of expansion of the aluminum being approximately 20 X 10^{-6}/∞C, cooling of the composite from the elevated processing temperatures results in a very large residual stress being produced within the MMC. The stress can be larger than the flow stress of the matrix [5]. Subsequent lowering of the temperature from ambient to liquid nitrogen temperature and reheating back to ambient greatly reduces the tensile stress in the matrix. In the work cited [5] x-ray diffraction techniques were used to measure the average stress in the matrix. The stress state is very complex since each fiber with its surrounding matrix behaves almost as a separate stress system. The x-ray measurements in the 10 μm diameter graphite fiber aluminum matrix composites effectively average the stress states of several fiber volumes.

Residual stresses can be calculated from the variation of an interplanar spacing, d, with tilt of the specimen relative to the x-ray beam. Two typical types of goniometer (Ψ or ω goniometer depending on the relative tilting direction) can be used. The residual stress level is calculated from the slope of d (interplanar spacing) vs. $\sin^2\Psi$ where ψ is the tilting angle defined in Fig. 3 assuming that a biaxial stress state exists in the near surface volume of material probed by the x-ray. This method does not need standardization or calibration of the system. Residual stresses are determined using the following relation [6,7]

$$\sigma = \frac{E}{1+\nu}\; m \;\frac{1}{d_{\phi,\Psi=0}}$$

σ, E, ν, m, and d are stress, Young's modulus, Poisson's ratio, slope of $d_{\phi,\psi}$ vs. $\sin^2\Psi$, and interplanar spacing. φ and Ψ are the angles referred to Fig. 3. Nonlinear d vs. $\sin^2\Psi$ distributions which cannot be explained by classical biaxial stress theory have often been observed in stressed materials. This may be due to the fact that x-rays penetrate many micrometers into the material and sample the stress state in the interior which may be complex and multiaxial even though the surface is biaxial. In this case, d is no longer inear vs. $\sin^2\Psi$. By introducing the concepts of an average strain and deviation, six stress ensor values can be determined [7].

The aluminum MMC that was evaluated for residual stress was comprised of P100 itch derivative graphite fiber and 6061 Al alloy. The two thermal treatments reported on ere are on samples given thermal treatments performed in a vacuum of 1 - 2 X 10^{-6} Torr Treatment A involved heating to 500°C for 30 min. and water quenching. Treament B was eatment A plus a 200°C heat treatment for 30 min. followed by water quenching.

The residual stresses found for these conditions are shown in Table 1. As shown in ig. 4, the stress is tensile in the matrix, the only part of the composite in which the esidual stress measurements were made. For force equilibrium, the stresses in the fibers must then be compressive in nature. Extensive measurements are still required to etermine the applicability of the three dimensional stress model to the heavily constrained atrix in the MMC as well as to explain why the measured stresses are well below the xpected values.

Table 1
XRD measured residual stresses in P100 graphite/6061 aluminum MMC for thermal treatments A and B

ample	σ_{11}	σ_{22}	σ_{33}	σ_{12}	σ_{13}	σ_{23} (MPa)
A	70 ± 14	48 ± 10	37 ± 8	-2 ± 12	0 ± 2	6 ± 2
B	37 ± 19	14 ± 19	17 ± 14	21 ± 4	4 ± 1	8 ± 5

σ_{11}, σ_{22}, σ_{33} are stresses parallel to the fibers in the plate, normal to fibers in the plate an ormal to the plate, respectively.

High-Energy, High Rate Processing of Aluminum SiC Particulate Metal-Matrix Composites

For many of the rapid solidification rate (RSR) powdered aluminum alloys that are candidates for the matrix in aluminum metal-matrix composites (MMCs), prolonged high temperature exposure during consolidation prevents the optimization of the matrix properties. This basic powder processing drawback has led to an attempt to reduce the time at temperature during consolidation by employing high energy high rate (HEHR) processing of aluminum-based MMCs [9].

This study presents a novel HEHR process using a homopolar generator (HPG) as the power source to consolidate Al-SiC system composites. The process employs a fast-rising high-current pulse to heat and consolidate powders. The HPG converts stored rotational kinetic energy into electrical energy using the Faraday effect [10]. During consolidation the HPG current is passed through the mixed powders. The bonding achieved by this technique results from the pulse resistive heating which is produced at interparticle interfaces. Because the hot thermal cycle is of the order of one second and the fact that the energy is concentrated at interfaces, bonding of the compact can occur without the powder interiors seeing significant time at temperature. This provides the possibility of maintaining the desired microstructural features associated with the original RSP processed powders. The powders are contained in an electrically insulated die under pressure and are rapidly densified during the HPG pulse discharge. A schematic of the consolidation die arrangement is shown in Fig. 5. For a typical pulse, sketched schematically in Fig. 6, the peak energy input occurs 200 milliseconds after the pulse is initiated, at which time the pressure is increased. Energy inputs of 400 kJ/Kg to 2500 kJ/Kg at applied pressures of 100 MPa to 300 MPa have resulted in consolidated forms with densities of approximately 80% to 99% of theoretical. For low energy compaction (≅800kJ/Kg) the consolidated material has a low density (≅88% of theoretical) and is still green, see Figure 7a. At higher compaction energies (up to 2500 kJ/Kg) densities greater than 95% of the theoretical value have been achieved, see Figure 7b. At the highest energy input some interparticle melting can contribute to densification. Figure 8a and 8b show the microstructure of the RSR ALCOA CW67 powder alloy before and after HEHR consolidation where most of the microstructure has low energy compaction (≅800kJ/Kg) the consolidated material has a low density (≅88% of theoretical) and is still green, see Figure 7a. At higher compaction energies (up to 2500 kJ/Kg) densities greater than 95% of the theoretical value have been achieved, see Figure 7b. At the highest energy input some interparticle melting can contribute to densification. Figure 8a and 8b show the microstructure of the RSR ALCOA CW67 powder alloy before and after HEHR consolidation where most of the

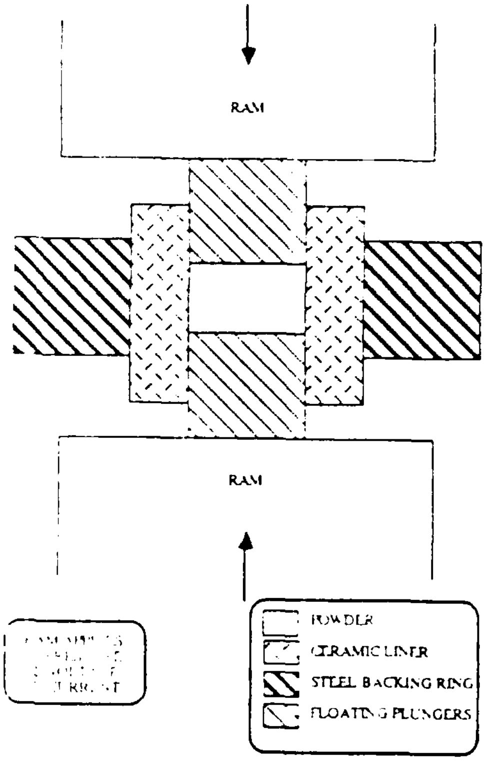
RAM
RAM
POWDER
CERAMIC LINER
STEEL BACKING RING
FLOATING PLUNGERS

Fig. 5 Schematic of die used for materials consolidation.

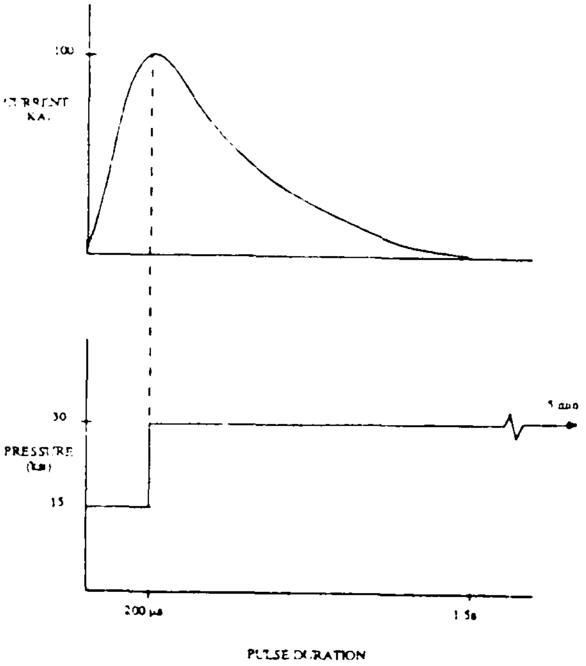

Fig. 6 Schematic diagram showing the variation of current and pressure during consolidation.

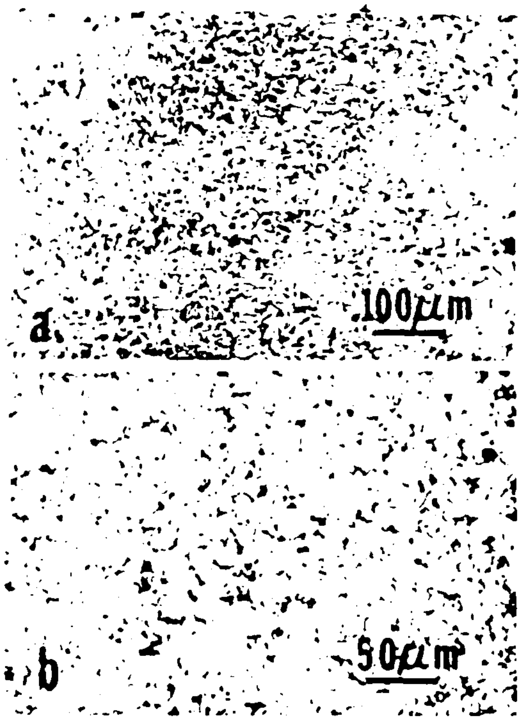
a
100μm
b
50μm

Fig. 7 Optical micrographs showing consolidated material after (a) low energy (500 kJ/Kg) and (b) high energy (2500 kJ/Kg)

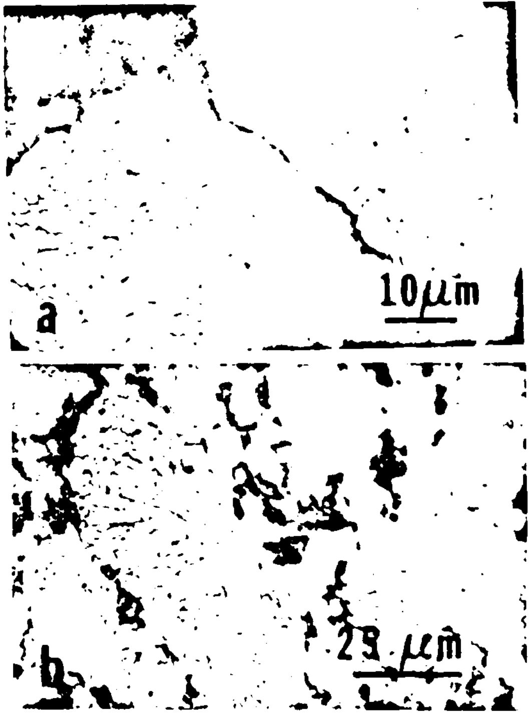
a
10μm
b
25 μm

Fig. 8 Optical micrographs of sections through (a) the as received CW67 powder and (b) the consolidated material.

microstructure has been retained. The material systems that have been processed to date include the X7091, CW67 and Al-Fe-Ce P/M aluminum alloys combined with different types and grades of particulate form of SiC with both the α and β crystal structures. This research effort has only recently been initiated, but the promise of the HEHR consolidation approach has been demonstrated. To improve the mechanical properties of the composites subsequent HRHE forging and extrusion processes using the HPG are also being explored.

ACKNOWLEDGEMENTS

The authors want to acknowledge the assistance of T. Aanstoos of The Center of Electromechanics at The University of Texas and the support of Dr. C. Persad in the processing of the Al/SiC discontinuous composites. The aluminum alloy powders were supplied by ALCOA. This research was supported in part under the DARPA/ONR contract N00014-84-K-0687

References

1. Lo, J., Finello, D., Schmerling, M. and Marcus, H. L., 'Interface Structure of Heat Treated Aluminum Graphite Fiber Composites', in *Mechanical Behavior of Metal-Matrix Composites*, eds. J. E. Hack and M. F. Amateau, ASM-AIME: New York, 1983, pp. 77-81

2. Tsai, S. D., *The Characterization of the Interface in Graphite Aluminum Composite Systems*, Ph.D. Dissertation, The University of Texas at Austin, Austin, Texas, 1980.

3. Mendez, H., Finello, D., Walser, R. and Marcus, H.L., 'Correlation of Electronic State and Fracture Path of Aluminum-Graphite Interface', *Scripta Met.*, Vol. 16, 1982, pp. 855-58.

4. Skinner, S., Savage, R.L., and Rutzler, J.E., Jr., 'Electronic Phenomena in Adhesion. I. Electron Atmospheres in Dielectrics', *J. Appl. Phys.*, Vol. 24 No. 4, April, 1953, pp. 438-450.

5. Tsai, S. D., Schmerling, M. and Marcus, H.L., Proc. of the 28th Sagamore Army Materials Research Conf. entitled "Residual Stress and Stress Relaxation," July (1981) Lake Placid NY, ed. E. Kula and V. Weiss, pp. 425, Plenum Press, 1982.

6. James, M.R. and Cohen, J.B., "The Measurement of Residual Stresses by X-ray Diffraction Technique." Experimental Methods of Material Science, vol. 1, 1978.

7. Hilley, M.E., "Residual Stress Measurement by X-ray Diffraction", SAEJ784a, Soc. Automotive Eng., 1971, 16.

8. Dolle, H., "The Influence of Multiaxial Stress State, Stress Gradients and Elastic Anisotropy on the Evaluation of (Residual) Stresses by X rays", *J. Appl. Cryst. 12*, 1979, pp. 489-501.

9. Elkabir, G., Rabenberg, L., Persad, C. and Marcus, H.L., 'Microstructural Evaluation of High-Energy High-Rate P/M Processed Aluminum Alloy', *Scripta Met., 20*, 1986, 1411-16.

10. Walters, J.B. and Aanstoos, T.A., 'Welding and Billet Heating with Homopolar Generators', *Met. Prog.127*, 1985, 25.

INTERFACES IN METAL MATRIX COMPOSITES, ed. A.K. Dhingra and S.G. Fishman, 1986, p. 205.

APPENDIX C

INTERFACE FAILURE IN PLANAR ALUMINUM-GRAPHITE COMPOSITES

L. D. Brown, C. L. Grove, and H. L. Marcus

Department of Mechanical Engineering/ Center for
Materials Science and Engineering
The University of Texas
Austin, Texas 78712

Abstract

The interfacial adhesion and cohesion of planar aluminum-graphite metal matrix composites (MMC) in transverse loading are investigated with respect to the electrical characteristics of a planar device model of the aluminum/aluminum oxide/graphite system. The planar model is composed of a reactively evaporated oxide on single crystal graphite with an evaporated aluminum overlayer. This paper focuses on the role that electrostatic forces play in elucidating a correlation between the electrical properties and the mechanical properties of the (MMC) model.

Introduction

Tsai (1) and Mendez, et al. (2), during the study of fiber-matrix interfacial characteristics in aluminum-graphite metal matrix composites (MMC), observed a correlation between the electrical state of a planar model graphite/aluminum oxide/graphie interface and its failure mode in tension. As shown in Fig. 1, when the aluminum oxide in the planar model was in a low conductive electrical state, failure occured by fracture through the oxide. However, the oxide could be voltage switched to a high conductive electrical state where failure occured by fracture through the graphite-oxide interface or possibly through the graphite. An oxide previously in the high conductive state would relax to its original low conductive state over a period of time and failure occured again by fracture through the oxide. Analogous changes in fracture path were also observed by varying the conductivity with oxide thickness. In this paper, we will suggest electrostatic adhesion as a possible explanation for the observed correlation between electronic state and fracture path.

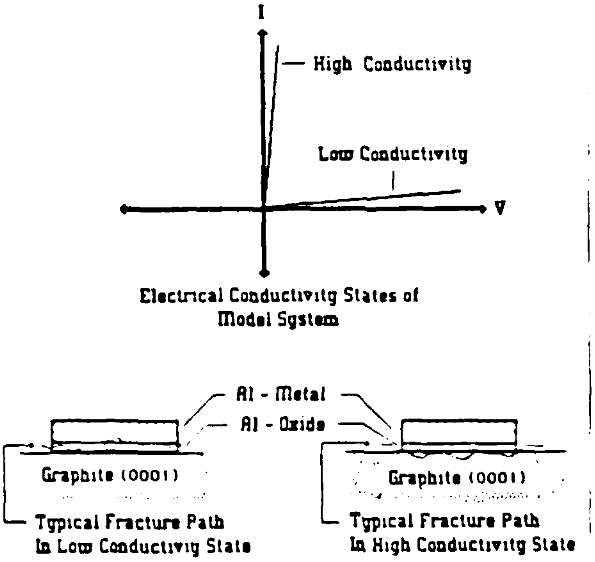

Figure 1 - The electrical conductivity states and fracture states of an MMC planar model.

Electrical Characteristics

Let us first consider the switching characteristics of the aluminum oxide as has been observed by others (3,4,5). The electrical switching is always observed in generally non-crystalline thin films which have been prepared under conditions of non-stoichiometry. As such their electrical characteristics are modified by defect states in the band gap of the insulator (6). These defect states represent low mobility states (i.e. traps) which isolate charge carriers (i.e. electrons and holes) from the high mobility conduction bands (i.e. conduction band for electrons and valence band for holes). A 2eV conduction band tail in non-crystalline $Al_2)_3$ supports this model (7). Experimental evidence has shown that for amorphous chalcogenide thin films (i.e. S, Se, Te containing inorganic compounds) the defect state density at the Fermi level is in the range of $10^{16}/cm^3$ - $10^{19}cm^3$ (6). This large defect density may not be strictly limited to an amorphous phase, as the gamma-Al_2O_3 observed by Mendez (2) has a spinel structure with heavily disordered tetrahedral sites (8).

With this model of possible gap states in the oxide, current injection becomes a distinct possibility for the observed I-V characteristics of the MMC planar model (9). The I-V characteristics of current injection, as shown in Fig. 2, are bounded by three limits: Ohmic conduction, Child's law, and the trap-filled-limit (TFL). The trap-filled-limit is the one of interest since this would represent the onset of the high conductive state and estimates the trap density not filled at zero voltage. Using the threshold voltage of 0.8 volts as observed by Tsai (1), the unfilled trap density is estimated to be in the range of $10^{16}/cm^3$. It is then possible that a large space charge density exists at the oxide-graphite interface prior to the electrical testing. These large trap densities are not unreasonable in view of the structural and chemical disorder found in the observed phases of aluminum oxide (8).

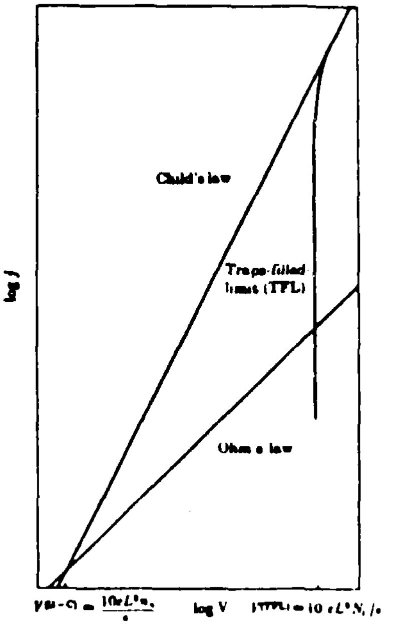

Figure 2 - The current-voltage response boundaries for current injection into solids. (After ref. 9)

Adhesion

The idea of electrical phenomena in adhesion was initailly studied by Skinner, et al. (10). The adhesive forces estimated by Skinner result from electrostatic considerations of a space charge accumulation at a metal-insulator interface due to charge transfer from the metal to the insulator. These charge transfer concepts wre first proposed by Mott and Gurney (11) and earlier, Fowler (12) coupled the concept of thermionic space charges to electrostatic forces in a parallel plate capacitor. Skinner's theoretical estimates showed that the adhesive electrostatic forces are only of significance when the space charge density is quite large, on the order of $10^{19}/cm^3$. Due to his work with adhesives as his insulator, where other factors contribute significatly (e.g. London dispersion forces, chemical bonding, elasticity, etc.), the electrostatic adhesion force was never considered more than a "negligible" contribution (13). However, as was just discussed this may not be the case in the oxide-graphite system.

Using values of space charge density between 10^{18} and 10^{20}, Fowler's approximations as to their extent into the oxide, Poisson's equation, and Maxwell's stress equations (14), a compressive stress of 4kPa to 400kPa is estimated to exist at the oxide-graphite interface in the low conductive state. In the high conductive state, there should be a significant cancellation of the bounding plate surface charges which should neutralize the electrostatic adhesion between the oxide and graphite. Mechanical measurements of the strength of aluminum/aluminum oxide/graphite planar model MMC's in the high conductive electrical state indicate a failure stress in the range of 20kPa (15) with the location of failure at the oxide-graphite interface. So within the confines of the difficulties of interpreting mechanical strength measurements of thin films, this failure stress is in qualitative agreement with the lower limit of the estimated electrostatic stresses.

Cohesion

Although the previous discussion gives an estimate of the strength of the aluminum oxide-graphite interface due to electrostatic forces, they are not sufficiently large to explain why failure should occur in the oxide when the MMC model is in the low conductive state. The presumption that the interface is stronger than the oxide, based upon bulk oxide strengths, may be misleading. It is possible that the oxide is inherently weak due to the macroscopic electric field gradient resulting from the space charge distribution in the oxide volume.

Considerations of dipoles in an inhomogeneous electric field, such as in the space charge region, invokes an electrostrictive contribution to the body force in a dielectric (14). It is proportional to the gradient of the electric field squared. The dipoles are always pulled into regions of increasing field magnitude. For hydrated oxides, as in the case in aluminum oxides, this contribution may be significant in modifying the oxides apparent strength. For the charge densities discussed above, an electrical field of the order of 10^5 volts/cm is produced in a linear approximation. The gradient of this field squared produces a force of 60kPa. However, because this assumes a uniform field across the space charge, it should be considered a minimum. Non-linear fields and space charge distributions that are not well behaved would produce much greater forces locally within the charged region.

This electrostrictive force could affect the oxide in two ways. First the oxide may be weakened locally in regions of increasing field gradient. Dipoles, such as bound hydroxides and localized charges would be stressed during and after fabrication. This effect could be amplified in the vicinity of pre-existing crack tips. These conditions then provide regions of locally "flawed" oxide or local stress concentrations possibly capable of causing failure below the stresses previously estimated. Secondly since the field generally increases as the oxide-graphite interface is approached, the electrostrictive force also contributes to the compressive stress field at the interface. The result of these considerations is to increase the failure stress of the interface while decreasing the failure stress of the oxide.

Summary

In this note, we have discussed macroscopic origins and effects which might possibly produce the electrical switching-fracture path phenomena observed by Tsai (1) and Mendez, et al. (2). The mechanisms of the change in fracture path are based on the electrostatic contributions of the space charge within the oxide acquired through charge transfer with the electrodes. This electrostatic force may be greater than 400kPa and compressive at the graphite-oxide interface. The magnitude of the forces are believed to be a direct result of the large chemical and structrual disorder of the insulating oxide. The adhesive interfacial forces were not presumed to be greater than an unflawed oxide's strength, but rather weakening mechanisms were postulated which indicated that the oxide could be "flawed" before mechanical testing. Failure occurs through the oxide, in the low conductive state, primarily due to this weakening effect and the "strong" compressive forces at the interface. In the high conductive state, the graphite and aluminum are electrically shorted by the oxide's conduction band and their respective space charges or surface charges cancel out. Since the balancing compressive stresses in the electrodes have disappeared, the electrostatic adhesive force disappears and failure occurs at the graphite-oxide interface or within the graphite. It is consistent that the electrostatic contributions to adhesion should be exhibited at the graphite-oxide interface rather than the oxide-aluminum interface since the graphite basal plane is less reactive than the aluminum metal surface.

A detailed and mathematically complete description of the above phenomena is not tractable at this time due to the complexity of the interdependent contributing concepts and unknown mateial properties, mainly associated with the interfacial oxide. The approximations given in this note can unquestionably be refined with appropriate experimental evidence. However, the given estimates of strengths to be expected indicate that this concept is worthy of further investigation. Experiments aimed at evaluating these concepts are now in progress. Acknowledgement: This research was supported by the DARPA under the ONR contract N00014-84-K-0687 at the University of Texas at Austin.

References

1. S. W. Tsai, "The Characterization of the Interface in Graphite-Aluminum Composite Systems" (Ph.D. thesis, The University of Texas at Austin, 1980).

2. H. Mendez, D. Finello, R. M. Walser, and H. L. Marcus, "Correlation of Electronic State and Fracture Path of Aluminum-Graphite Interfaces," Scripta Met., 16 (1982) 855-858.

3. H. Birey, "High Field Transport Properties of Aluminum-Embedded Aluminum Oxide Films," Appl. Phys. Lett., 23(6)(1973), 316-318.

4. H. Demiryont and N. Tezey, "Characterization of Al-AlO_x and Sn-SnO_x Cermet Films Deposited by Reactive Evaporation," Thin Film Solids, 101 (1983) 345-356.

5. S. Nakahara and A. F. Hebard, "Microstructure Trends in Metal (Aluminum Copper, Indium, Lead, Tin)-Metal Oxide Thin Films Prepared by Reactive Ion Beam Sputter Deposition," Thin Film Solids, 102 (1983) 345-360.

6. N. F. Mott and E. A. Davis, Electronic Processes in Non-Crystalline Materials (Oxford University Press, 1971).

7. A. Balzarotti and A. Bianconi, "Electronic Structure of Aluminum Oxide as Determined by X-Ray Photoemission," Phys. Stat Sol (b), 76 (1976) 689-694.

8. K. Wefers and G. M. Bell, "Oxides and Hydroxides of Aluminum" (Tech. Paper No. 19, Alcoa Research Laboratories, 1972).

9. M. A. Lampert and P. Mark, Current Injection in Solids, (New York, NY: Academic Press, 1970).

10. S. M. Skinner, R. L. Savage, and J. E. Rutzler, Jr., "Electrical Phenomena in Adhesion.I.Electron Atmospheres in Dielectrics," J. Appl. Phy, 24(4)(1953), 438-450.

11. N. F. Mott and R. W. Gurney, Electronic Processes in Ionic Crystals, 2nd ed. (New York, NY: Dover Publications, 1948), 152-201.

12. R. H. Fowler, Statistical Mechanics, 2nd ed. (New York, NY: McMallian Co., University Press, 1936), 364-369.

13. J. R. Huntsberger, "The Mechanisms of Adhesion," Treatise on Adhesion and Adhesives, vol. 1, ed. R. L. Patrick (New York, NY: Marcel Dekker, 1966), 137-143.

14. W. H. Panofsky and M. Phillips, Classical Electricity and Magnetism, 2nd ed., (Reading, MA: Addison-Wesley, 1962), 103-110.

15. L. D. Brown, unpublished research.

Appendix D

Electrical-Mechanical Oxide Switching in Thin Film Aluminum-Al Oxide-Graphite Composites

L.D. Brown and H.L. Marcus

INTRODUCTION

To study the electrical-mechanical switching characteristics of the aluminum-oxide-graphite composite model, several experimental systems were designed and constructed. These systems and their basis will be briefly discussed. The electrostatic adhesion-cohesion model and its basis will then be summarized. Next the recent observations on the electrical and mechanical properties of the composite system are presented. Finally these are discussed with respect to an understanding of the oxide-graphite interface.

Thin film aluminum oxides are generally prepared by reactive depositions in various forms: anodization, thermal evaporation, DC sputtering, RF sputtering, plasma anodization, and electron beam evaporation are the major methods. Each has its own variations. The predominant method is still anodization of thin aluminum films, but this is not directly applicable to this study. The electrical switching phenomena has only been reported for thin aluminum oxide films prepared by reactive thermal evaporation.[1,2] The film preparation was not carefully controlled. It is reported as aluminum evaporated in increasingly poor vacuums of a diffusion pumped bell jar system.

A reactively evaporated oxide morphology is strongly dependent on the partial pressure of any reacting species in the vacuum system. The metallic character exists at low O_2 partial pressures. The morphology transforms to that an oxide cermet at increasing partial pressures until a continous non-crystalline oxide forms at O_2 partial pressures in the range of 10^{-4} torr. The Al-Al oxide cermet morphology has only weak experimental evidence, but is consistent with other thin film oxide morphologies(Sn,Cu).[3] Conclusive studies of oxide films exhibiting electrical properties other than high resistivity, reasonable dielectric constants, and low loss tangent are scarce.

The overall factors governing film quality have been narrowed to five interdependent sources: 1) Reacting species partial pressure, 2) Deposition rate, 3) Substrate-to-source distance, 4) Substrate temperature, and 5) Ionizing potential. The last factor is relevant only to preparation techniques utilizing electric potentials(e.g. RF and DC biased sputtering, activated reactive evaporation, etc.) and was not used in this study so as to be consistent with earlier work.[2] The partial pressures were discussed previously. The deposition rate is determined by the reacting species partial pressure and for a constant film morphology, can be higher the greater the partial pressure. For pressures in the 10^{-4} torr range, the deposition should not exceed two angstroms per second to obtain a homogeneous non-crystalline film. Increasing the deposition rate is generally equivalent to decreasing the reacting species partial pressure. Due to source characteristics in thermal evaporation,the deposition rate can be difficult to accurately control over extended periods of time. The substrate-to-source distance should be at least 20 cm. This is for film uniformity as well as to minimize substrate heating by the source thermal radiation. The source and substrate should be as directly over each other as possible. Angular deposition will produce morphological anisotropic films. For homogenous films, the substrate temperature should be elevated above room temperature. The higher the temperature the more homogeneous the film. This precludes increased reaction with the substrate and phase changes in the film. The effect must be viewed within the context of a sense of the reaction rate, as conveyed by the first three factors, and the reacting species-substrate interaction(i.e adsorption,chemisorption, and wetting characteristics). This should be kept in mind when determining the substrate temperature. Elevated temperatures for reactive evaporation of Al-oxide have not been reported. However post-anneals have been reported as required to achieve stable electrical properties.[4] Post-anneals were not used in this study so as to remain consistent with the earlier observations.[2]

It is important to state that thin film characteristics, electrical and mechanical, are directly attributable to the method of preparation which is critical in determining the film's structural nature. The initial state of the oxide can be stated in general terms as being non-crystalline. However differences in initial state become apparent when films prepared by different methods, or even by the same method but different conditions, are subsequently processed.[4,5] Analgous systems would be that of metallic glasses or rapidly solidified powders. This may be attributed to slight atomic configuration variations in the non-crystalline film which favor certian reaction paths to equilibrium over others. The effect can be more pronounced in thin films where surface energy is a major consideration and in oxide systems where ionic-covalent bonding occurs. In addition the choice of substrate must be considered as perturbation to the transformation path as nucleation is generally initiated at the film-substrate interface. Most thin oxide films for electrical studies are deposited on Al, Si, or Au. Mechanical studies(i.e. residual stress) use insulators(i.e. glass plates). To this author's knowledge, graphite has not been used although it has been widely used in fundamental studies of tunneling microscopy, adsorption and wetting, and electrochemistry to name a few.

EXPERIMENTAL

In this study the deposition rate was held below one angstrom per second as averaged over the time of the reactive deposition. The substrate-to-source distance was set at 25 cm. The reacting gas was injected approximately 3 cm below the substrate in an annular fashion. The gases consisted of ultra-pure carrier grade O_2 and Ar with hydration accomplished via a reacting gas pressurized bubbler filled with doubley de-ionized water. Pattern definition on the substrate was achieved by using a rotating mask holder positioned approximately 0.3 cm below the substrate. In this way multiple patterns could be defined on the substrate without breaking vacuum. Film thickness was monitored by a quartz crystal oscillator. The substrate temperature, for the results reported here, was allowed to float during deposition. The temperature rise during reactive evaporation was a maximum of 20° C above ambient, 23° C. Temperature rise was monitored using a type K thermocouple attached to a copper foil pad situated between the two substrates. Holey carbon TEM grids were fixed onto this pad for subsequent film examination and Al-O-C reactions as discussed in other areas of this report. All films in this report were non-crystalline.

With the previous factors held constant from deposition to deposition, the reacting gas mixture was used as a variable. As stated earlier the switching phenomena has only been reported when aluminum was evaporated in increasingly poor vacuums. Gas injection was used to simulate, in a controlled manner, increasingly poor vacuums. Varying proportions of O_2:Ar:H_2O could be injected into the chamber. Maintaining an overall chamber vacuum of 10^{-4} torr during reactive evaporation kept any residual partial pressures at least constant from evaporation to evaporation. After a controlled film thickness was reactively evaporated an overlayer pattern of 100 nm of aluminum from a separate source was evaporated at rates in excess of 30 nm/min. in a vacuum of 10^{-6} torr. The base vacuum was no worse than $1x10^{-6}$ torr. The results reported here are for oxides prepared in 10^{-4} torr O_2 or H_2O saturated Ar at 10^{-4} torr.

The electrical characterization of dielectrics requires measurement of high voltages, low currents with source resistances in excess of 10^9 ohms. Low resistances were also encountered. These require relatively high currents and low voltages. In addition, thin film oxides can exhibit characterisitics of both semiconductors and insulators. As indicated in earlier reports and shortly to be reviewed, the switching phenomena is considered to be initiated by high interfacial fields. This suggests that interfacial barrier determinations might show a correlation to the mechanical failure behavior. In this study the oxide-graphite system's electrical nature was characterized by I-V and AC methods. Through the use of a Keithley 220 current source, a Keithley 230 voltage source, a Keithley 617 electrometer, a Hewlett-Packard 4192A impedance analyzer, an IBM XT computer,and a constructed test fixture, a wide range of electrical characteristics could be measured. The system is capable of measuring DC characteristics of picoamp to milliamp currents under micro-volt to 100 volt excitation and micro-volt to 200 volt potentials under picoamp to 100 milliamp excitation. AC characteristics can be measured from 5 Hz to 13 Mhz at 0.005 to 1.000

volt excitation with biasing from -35 to +35 volts. All electrical measurements are computer controlled for consistancy and ease of analysis. Temperatures can be varied from -100°C to +100°C in atmospheres from 1 torr vacuum to positive pressure gas. The purpose of the test fixture was to maintain the specimen in a dry, controlled, electromagnetically shielded, and light tight environment. All measurements reported here were made in chromatographic Ar or in vacuum at relative humidities less than 10%.

DC measurements were analyzed for Schottky emission, Fowler-Nordheim tunneling, Frenkel-Poole conduction, space-charge-limited conduction, dV/dI, dI/dV, and polarization response when displacement currents were a predominant response. AC measurements were analyzed using experimental impedance diagrams(e.g. Cole-Cole plots, Argand diagrams, capacitance-bias,etc.) in conjunction with model impedance diagrams using the PSPICE circuit modeling program.

Mechanical measurements consisted of failure stress determination by the direct-pull-off method. It is essentially the electrical test chamber with a load pin and chain assembly dropped through a center hole in the chamber lid aligned by a guide rod assembly. Sliding friction between the guide rod and the pull rod was kept below 0.001 N by using a boron nitride coated aluminum against brass combination. Pull rates were kept at 0.05mm/min.. Loads encountered were less than two newtons with load areas of 6 mm^2. Fracture areas were always less than this. Electrical testing was carried out prior to mechanical testing by using a room temperature CERAC Ag epoxy as a bonding agent between the specimen and the load pin. The load pin was electrically isolated form the chamber with a measured isolation resistance of > 10^{12} ohms. Optical and scanning electron microscopy were used to examine the fracture surfaces after mechanical testing.

ELECTROSTATIC ADHESION

As described in earlier reports, of all the accepted adhesion mechanisms, electrostatic adhesion is the most consistent with the observed electrical-mechanical switching phenomena.[6] Previous critisism of electrostatic adhesion seems more associated with the polymer systems where elasticity would dominate the failure process and measurement. [7] Where chemical bonding is present, electrostatic adhesion is not directly applicable but may be a precursor to wetting. In this sense it is more akin to dispersion forces of which van der Waals bonding is a subset. Van der Waals bonding is believed to be the predominant cohesion force between graphite basal planes.[8] To this authors knowledge, it has not been applied to brittle oxide films and seems especially noteworthy on inert substrates such as the graphite basal plane. It simultaneously satifies the localized nature of the electronic switching and the global nature of the mechanical switching.

Of fundamental importance to the Maxwell stress formulation of electrostatic adhesion are intrinsic electric fields in the vicinity of the interfaces of the film. The developed stress is proportional to the local field squared. The electrical fields are a result of the dipolar nature of charge separation. This charge separation would occur during film formation. The existence of low mobility quasi-stable defect states is a basic characteristic in switching thin films and believed to be the fundamental basis for the development of high interfacial fields which produce switching.[9] If these defect states were charged, then an image space charge would develop in the graphite surface layers resulting in an interfacial electric field. For any appreciable electrostatic stress to develop, there would have to be on the order of 10^{17}/eV/cm^3 defect states within the oxide film near the graphite. This seems plausible as evaporated non-crystalline films, chalcoengides, have this order of measurable states within their band gap at the midgap level.[10] The oxide films might be considered to be a case worse than this as chalcoengides are covalently bound, all the bonds are satisfied, and they are difficult to dope. Reasonable electrostatic adhesion stresses have been estimated to be in the range 20kPa to 500kPa.[7]

This may or may not be sufficient to maintain a larger interfacial strength over that of the oxide film's cohesive strength. Thin film oxide strength measurements have never been published. Failure within the oxide when the oxide is in an insulating state however has been observed.[2] It is plausible in view of the fact that the crystal structure of transition aluminum oxide phases are essentially layered structures bound by hydrogen bonds.[11] The lower the transition phase order the more hydrogen contributes to stabilizing the crystal structure. In this manner the electrostatic adhesion at the interface may be favored over the structural cohesion of the thin film. Within these considerations, electrostatic adhesion seems justified as a plausible explanation for the electrical-mechanical switching phenomena in the aluminum oxide-graphite system.

RESULTS

Electrical characterization of the oxide films reactively deposited on aluminum coated alumina where fairly consistent. A typical result was a measured capacitance at very low frequency, 10^{-3} Hz, and low frequency, 100 Hz, which exceeded that at high frequency, 100 kHz, by a factor of 5 or 6. This is an indication of interfacial polarization resulting from space charge development at the interfaces.[12] The conduction mechanism was Schottky emission. A typical dielectric constant calculated from the Schottky plot was approximately 3.5. This is within the optical constant of 2.5 and the static constant of 5 to 6 and is consistent with carrier transition over a Schottky barrier.[13] Figure 1 is an experimental Shottky plot of a 50 nm oxide film on aluminum made in an O_2 atmosphere and electrically tested under DC voltage step conditions.

Electrical characterization of oxide films on pyrolitic graphite were inconsistent from specimen to specimen. Figure 2, figure 3, and figure 4 are experimental I-V plots of two oxide films on HOPG. In general all that could be definitively said about the specimens is whether they exhibited a high resistance state, $> 10^9$ ohms, or a low resistance state, $< 10^2$ ohms.

Attempts to correlate failure stress with electrical characteristics were inconclusive. Table 1 lists the pertinent data. The load-displacement curves on all specimens were linear until failure which was catastophic(i.e load dropped to zero at failure). Delamination type failure was not exhibited as the load remained constant when displacement was stopped during the test.

It is interesting to note that the baseline value for the failure stress appears to be in the range of 250 kPa. The range can be as high as 600 kPa and as low as 190 kPa. A thin highly insulating oxide appears to favor larger failure stress while low resistance films favor lower failure stresses. Larger failure stresses also seem to be indicative of more extensive failure within the graphite. The evidence is by no means conclusive. However it is the only data of its kind presently available as any indication of the intrinsic strength of the aluminum oxide-graphite interface.

TABLE 1: Failure characteristics of aluminum oxide films on highly oriented pyrolitic graphite. Measured after two days minimum in chrom. Ar with the relative humidity < 5%.

Nominal oxide Thickness(nm)	Resistive State (ohms)	% Graphite Failure (+/- 5%)	Failure Stress (kPa)
0	$< 10^2$	15(sl)*	203
50	" "	50(sl)	192
50	" "	10(sl)	255
50	" "	30(sl)	302
25	$>10^9$	50(ml)	637
	Reference single crystal Ticonderoga graphite in air		75(avg.)

---

* sl: under optical examination only a single layer of graphite could be distinguished on the load pin side of the failure.

ml: under optical examination multiple layers of graphite could be distinguished on the load pin side of the failure.

Certain physical characteristics of the specimens should be noted. After failure the HOPG surface exhibited exfoliation areas which under optical examination showed interference patterns. The spacing of the patterns was indicative of the gradient of the degree of HOPG surface layer delamination. This may be indicative of the degree of adhesion. These patterns were not observed in areas of complete HOPG surface failure which corresponded to areas covered by graphite on the load pin side of the failure surface.

In addition, when the specimens were exposed to lab air(50% relative humidity), oxide buckling occured in areas not covered by the aluminum overlayer. Its appearance was that of a "mole tunnel". The tunneling did not progress after the specimens were stored in a vacuum dessicator. The tunneling was believed to be a consequence of the reported compressive stresses in thin film oxides[5] reacting to the loss of adhesion at the oxide-grahite interface. This loss of adhesion was attributed to water vapor infiltration. The large polarizability of water molecules would neutralize the electrostatic interfacial adhesion. "Tunneling" was not observed under the aluminum overlayer prior to testing. The aluminum overlayers intrinsic tensile stress[5] would tend to compensate for the relaxation of the oxide's compressive stress.

CONCLUSION

A study of the oxide-graphite interface and subsequent data interpretation faces certain interdependent aspects which are not easily discernable as independent observations. Each aspect may in itself not be an easily studied phenomena. Wetting characteristics of aluminum atoms on graphite basal planes in an oxidizing atmosphere is one such aspect. This forms the basis for the adhesive character of aluminum oxide on graphite in reaction evaporation. The effect of residual stress in the oxide film in combination with that of any overlayer films on the developing oxide-graphite interface is an example of the complications involved. These are just now being addressed in the scientific literature.[14] Experimental measurement of an overall phenomena, such as electrical-mechanical switching, within the concepts of theoretical consistency becomes a complex task when viewed in this sense.

The results of this study to date may be summarized as follows:

1) The first attempt at measuring the interfacial strength of the aluminum oxide-graphite system in tension has been made. The strength was found to be related to the oxide's dielectric character. For a highly conducting system, the interfacial strength is in the range of 250 kPa. With thin, non-conducting oxide films, the strength is in the range of 600 kPa. This is consistent with the electrostatic adhesion model. The higher strength can also be correlated with a greater degree of failure within the graphite.

2) Correlating the electrical character with the adhesive-cohesive character of the oxide-graphite

system will be difficult. This is predominantly due to difficulties in data acquisition and interpretation. It may be useful in monitoring reactions at the oxide-graphite interface, however, and in correlating these to the adhesive-cohesive behavior.

3) The stresses of the aluminum overlayer on the oxide mask the intrinsic interfacial character. From the many mechanics studies on laminates, it may be stated that, without extensive interfacial modification, the bulk aluminum will determine the overall mechanical response characterisitics of the aluminum-graphite composite. The oxide-graphite interface is still the weak link with little load or strain transfer capabilities. This study provides values by which the interface may be better accounted for in overall response considerations.

4) Interface modification might best be pursued by modifying the oxide morphology since aluminum oxide has an intrinsically layered nature with weak hydrogen bonding between layers.In the sense of reactive evaporation, this might be accomplished in a partially reducing atmosphere(i.e. reduced oxidation) so that a cermet morphology is formed. One must keep in mind, however, the enhancement of aluminum carbide formation in areas of the oxide film rich in aluminum as stated in other areas of this report.

5) Water vapor is detrimental to the adhesive character of the oxide-graphite interface.

The research required for the formulation of a plausible explanation to the electrical-mechanical switching phenomena has resulted in a more basic understanding of the complexities of the oxide-graphite interface. It is believed that the ideas expounded above may be realized in principal with an associated better understanding of the oxide-graphite interface. . Information of this type is a partial prerequisite for significant advancements in interface engineering in the aluminum-graphite metal matrix composites. These advancements are needed prerequisites for the competive use of MMCs in engineered structures.

REFERENCES

1) H. Birey, Appl. Phys. Lett., **23**(6), 1973, pp. 316-318.

2) H. Mendez, et.al., Scripta Met., **16**(1982), pp. 855-858.

3) S. Nakahara,et.al., Thin Solid Films, **102**(1983), pp. 345-360.

4) T.N. Kennedy, Elect. Packaging and Prod., 1974, pp. 136-141 and references therein.

5) K.L. Chopra, Thin Film Phenomena, McGraw-Hill, 1966.

6) L.D. Brown,et.al., Interfaces in Metal-Matrix Composites, Ed. A.K. Dhingra and S.G. Fishman, Metallurgical Society, 1986, pp. 205-210.

7) J.R. Huntsberger, Treatise on Adhesion and Adhesives, Vol. 1, Ed. R.L. Patrick, Marcel Dekker, 1966, pp. 137-143.

8) A.R. Ubbelohde, et.al, Graphite and Its Crystal Compounds, Clarendon Press, 1960.

9) K.E. Petersen, et.al., IEEE Tran. Elect. Dev., **ED-23**(4), 1976, pp. 471-477 and references therein.

10) T.C. Arnoldussen, et.al, Phys. Rev. B, **9**(8), 1974, pp 3377-3393.

11) K. Wefers, et.al., Tech. Paper No. 19, Alcoa Research Laboraties, 1972.

12) F. Argall, et.al., Thin Solid Films, **2**(1968), pp. 185-210.

13) S.M. Sze, Physics of Semiconductor Devices,2nd Ed., John Wiley & Sons, 1981, p. 251

14) R. Pandit, et.al., Phys. Rev. B, **26**(9), 1982, pp. 5

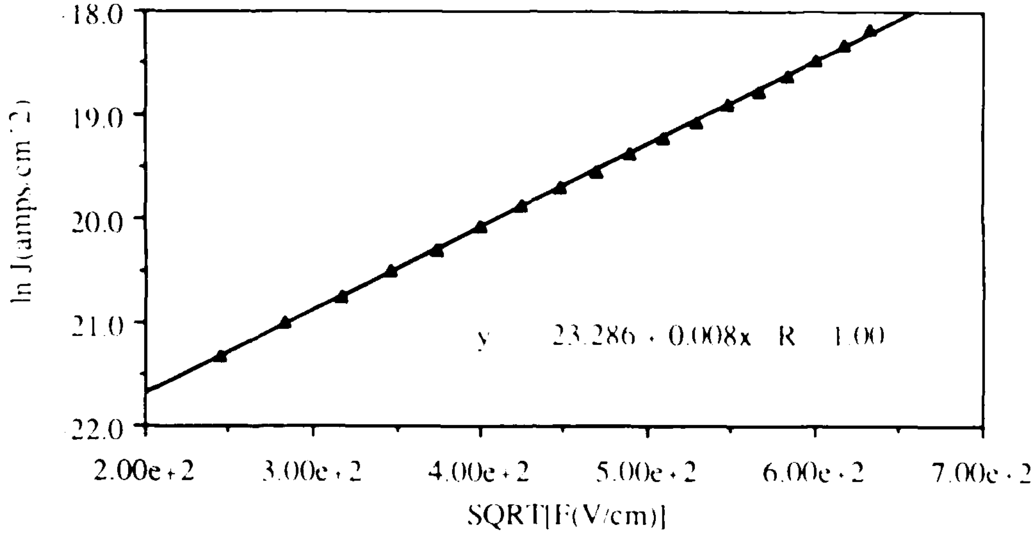

Figure 1: A Schottky emission plot of the I-V leakage response of a 50 nm oxide film on 100 nm of aluminum on alumina with a 100 nm aluminum overlayer. The oxide film was prepared by reactive evaporation in 10^{-4} torr of O_2.(High resistance state)

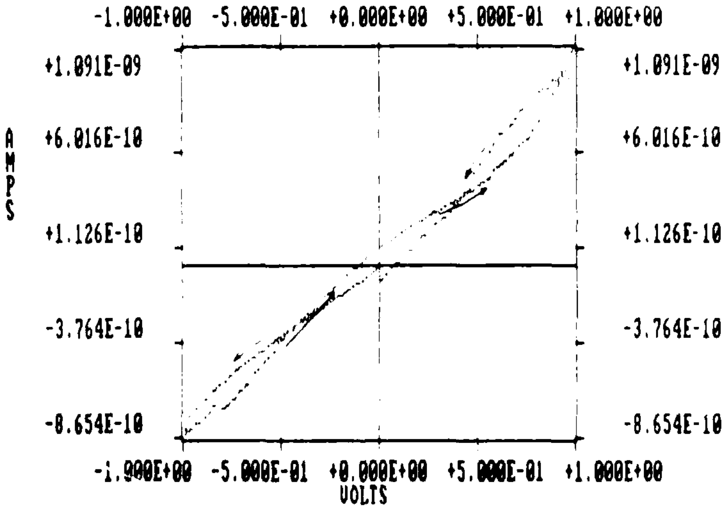

Figure 2: An I-V response of a 25 nm aluminum oxide film on HOPG with a 100 nm overlayer The oxide film was prepared by reactive evaporation in 10^{-4} torr of O_2.(High resistance state)

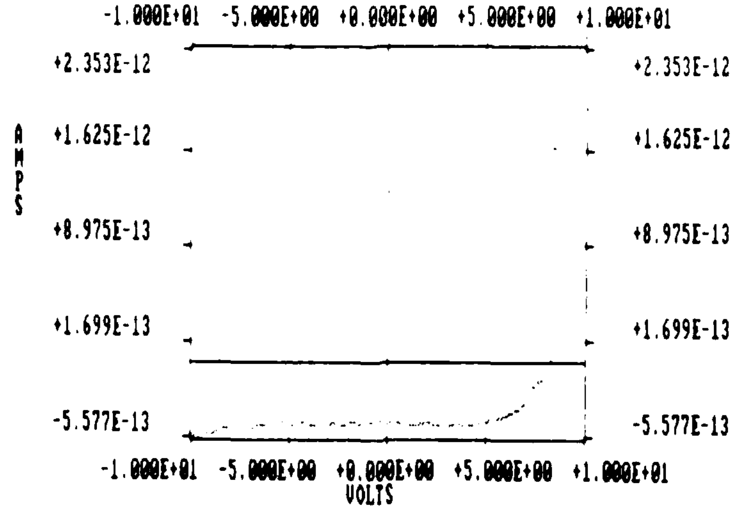

Figure 3 An I-V response of a 50 nm aluminum oxide film on HOPG with a 100 nm aluminum overlayer. The oxide film was prepared by reactive evaporation in 10^{-4} torr H_2O saturated Ar.(Like Fig. 2, this is considered a high resistance state)

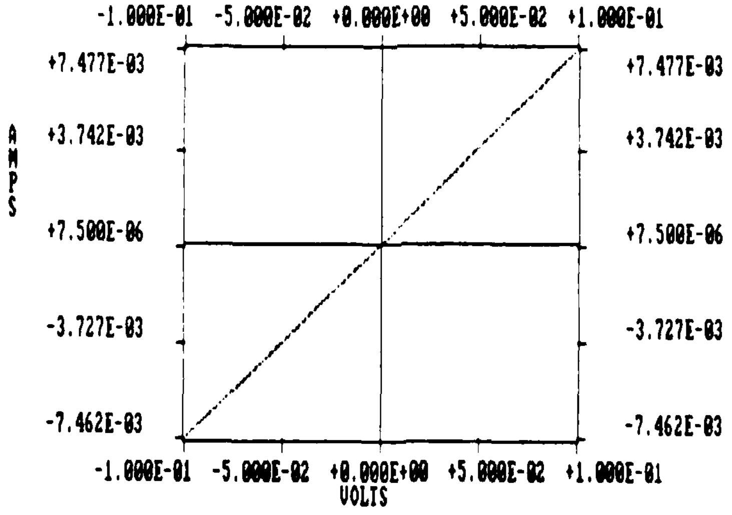

Figure 4: An I-V response on the system in Fig. 3 after switching to a low resistance state Resistance = 13.4 ohms

APPENDIX E

OXIDATION MODEL OF INTERFACE REACTIONS IN ALUMINUM/GRAPHITE COMPOSITES

Benji Maruyama and Llewellyn Rabenberg

Materials Science and Engineering
The University of Texas
Austin, Texas 78712

Abstract

The formation of Al_4C_3 at interfaces in Al/graphite fiber composites involves atomistic processes identical to those which occur during oxidation of graphite in air. In both cases, carbon-oxygen bonds are formed, carbon-carbon bonds are broken, and the products are transported away. Although many elements and compounds are known to catalyze the reaction of graphite with oxygen in air, only boron and phosphorus are known to poison *it. This suggests that Al_4C_3 formation may be hindered and interfacial* bonding may be improved by treatment of graphite fibers with boron and phosphorus compounds.

Introduction

The characteristics of the interfaces in aluminum/graphite fiber composites depend on: 1) the degree of wetting of the graphite by the aluminum, 2) the bonding between the Al and graphite, and 3) the presence or absence of any chemical reactions between Al and graphite which might occur during heat treatments. All three of these processes interact to determine the nature of the interfaces; they all play a role in the resulting mechanical properties of the composite.

Because of their importance to the final product, a large research and development effort has been aimed at improving interface properties. Since wetting of graphite by aluminum is difficult to obtain, chemical vapor deposition techniques are used to apply TiB_2 and other compounds to the fibers as wetting and bonding agents (1). Pressure infiltration with plasma deposited silicon and carbon before consolidation in Al is being attempted in order to improve bonding and to protect the fibers from chemical reaction during processing (2). To reduce the rates of interfacial reactions and aluminum carbide formation, refractory metals and carbides are being applied to the fibers before consolidating.

Of the several processes described above, this paper emphasizes the role of interfacial reactions and carbide formation in Al/graphite composites as a means of understanding interface properties. In the next section is a discussion of carbide formation in heat treated aluminum/graphite composites followed by a discussion of oxidation of graphite in air. Finally, implications of an oxidation model of aluminum carbide formation at Al/graphite interfaces including the possibility of reaction poisons will be presented.

Aluminum Carbide Formation

Aluminum carbide forms at Al/graphite interfaces of composites heated above 500°C for long periods of time [~4um in 100 hr at 530°C (3)]. The formation of aluminum carbide can be divided into three steps: the dissociation of carbon atoms from the graphite fiber, the diffusion of the carbon through the interfacial oxide layer into the matrix, and finally, the reaction of carbon and aluminum to form Al_4C_3. Although the second step has been shown to be the rate determining step for carbide thicknesses greater than 2-4 microns (3), it is the first step which allows insight into the nature of the interface properties.

The details of the aluminum carbide reaction have been investigated by many authors (1-8), and a partial summary is given here. Finello (4) found the anisotropy of graphite to reveal itself in reaction rate differences between basal plane faces (low reactivity) and basal plane edges and dislocation cores (high reactivity). This is logical, since in-plane chemical bonding is extremely strong in graphite (implying low reactivity), and any disruption of the bonding in the plane should expose highly reactive carbon atoms with uncompensated bonds.

A layer of oxide at the interface between the graphite fiber and the matrix is always present in industrial materials, and is likely to be present, albeit to a lesser extent, in deposited Al-Al/graphite interface models, and is important to all composite interfacial properties. The importance of the interfacial oxide in bonding have been underlined in works by Finello (4), Tsai (5), and Mendez (6) on fracture path correlation with electronic switching phenomena. During carbide formation, Finello (4) has shown that the carbide forms on the matrix side of the oxide.

This implies that during the interfacial reaction, the dissociation of carbon from the graphite must occur as a result of contact with the interfacial oxide, not with the matrix. Furthermore, it points to carbon, rather than aluminum, as the diffusing species. Work by Finello (4) and Motoki (8) indicate that the interfacial oxide slows the diffusion of carbon into the matrix, but Finello's work also indicates that the initial, interface-controlled reaction rate may be enhanced by the oxide layer.

Given the importance of the interfacial oxide, any theoretical model of the Al/graphite interface must incorporate its influence, and any physical model must include an interfacial oxide layer or account for its absence.

In summary, the reaction rates, or dissociation rates of graphite will depend on the orientation of the graphite and the number of exposed bonds. The interfacial oxide has been shown to be important in both interfacial bond strength and reaction kinetics. Here, an emphasis will be placed on the fact that the dissociation of carbon from the graphite fiber occurs as a result of direct contact with the interfacial oxide. Thus, a study of the interface controlled growth stage, where the dissociation of carbon from the fiber is the most important step, may shed new light on bonding at graphite/aluminum interfaces as well as interface reaction kinetics.

Oxidation of Graphite

As a model of the interface reaction, the oxidation of graphite in air was chosen because it can describe the removal of carbon atoms from the fibers and the inability to form a strong fiber-matrix bond. At first glance, a comparison of the two reactions reveals several similarities. The oxidation of graphite in air becomes significant at temperatures above 500°C, as with the formation of Al_4C_3 (3,4,7). Carbide formation rates (4) and oxidation rates (9) are site specific; basal plane faces are relatively unreactive whereas basal plane edges and dislocation cores are highly reactive. Also, oxygen is present at the interface, both in the form of passivating layer of Al_2O_3 and as adsorbed oxygen on the fiber surface. To develop the model, a description of graphite oxidation is given.

Following the discussion of Rakszawski and Parker (10), the process of graphite oxidation can be separated into several steps. First oxygen atoms are chemisorbed, C(0), onto active carbon sites, C_f, on the graphite surface (reaction 1). Next, chemisorbed carbon monoxide, (CO), is formed from the active carbon and the chemisorbed oxygen (reaction 2). And finally, the carbon monoxide is desorbed from the surface (reaction 3).

$$2C_f + O_2(g) \rightarrow 2C(O) \qquad (1)$$

$$C(O) \rightarrow (CO) \qquad (2)$$

$$(CO) \rightarrow CO(g) \qquad (3)$$

Reaction (2) can be considered as a rearrangement of pi bonds as shown in Figure 1, where C(0) is structure (a) and (CO) is structure (b).

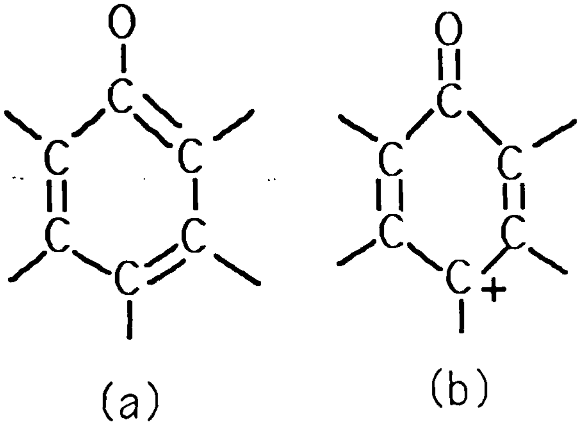

Figure 1 (from ref. 11)

As pointed out by Rakszawski and Parker, reaction (2) is catalyzed by the donation of an electron from the carbon matrix to a catalyst material which can be a suitable transition metal ion or other electrophyllic species. Reaction (2) results in the weakening of the carbon atom bond in (CO) to the matrix, as one π bond is lost. This is, in effect, the stabilization of structure (b) above. Relating this process to interface bonding, a material that stabilizes structure (b) relative to (a) should enhance carbon bond weakening and subsequent dissociation. Since Al_2O_3 is a Lewis acid or electron acceptor, it should stabilize structure (b), implying that Al_2O_3 should enhance dissociation of carbon. In a similar fashion, the action of TiB_2 as a wetting agent is believed to be the stabilization of π bond structure (a) as will be shown below.

It is well known that many substances enhance graphite oxidation, and included in these are aluminum and aluminum oxide. This is verified by oxidation rates taken from Rakszawski and Parker (10) where the relative catalytic effects are shown. The strengths of these effects are shown in table 1.

Table I. Oxidation Rates of Graphite in Air at 700°C (10)

Additive	*Rate* (hr^{-1})	*Rate Relative to* Pure Graphite
None	0.072	1.0
Al	0.118	1.64
Al_2O_3	0.181	2.52
B	0.032	0.44
B_2O_3	0.033	0.46
P	0.017	0.24
P_2O_5	0.016	0.23

0.1 mole per cent added to graphite powder.

Notice that aluminum oxide increased oxidation by 2.52, while boron and phosphorus compounds reduced the oxidation rate to as low as 0.23. In fact, boron and phosphorus compounds are the only compounds known to significantly decrease the oxidation rate (9,10,12). Two conclusions can immediately be drawn from these facts. First, the dissociation of carbon from graphite, and thus the formation of Al_4C_3 is catalyzed by the presence of Al_2O_3. Second, the wetting action of TiB_2 is attributable to better bonding characteristics of boron, and thus enhanced stability of the interface. Thus, it is possible that the same factors govern both interface bonding and interface reaction mechanics.

McKee et al. (9,12) have investigated bond order and oxidation inhibition of boron and phosphorus compounds using Fourier Transform IR spectroscopy (FTIR). Their studies reveal that organic phosphate and phosphite esters and organo-borates are strongly adsorbed onto active graphite sites, and that the unoccupied d-π orbital in phosphorus serves to mediate the otherwise overwhelmingly strong carbon-oxygen bond. Also, based on steric arguments, boron oxide should preferentially poison graphite $\{10\bar{1}0\}$ faces (figure 2).

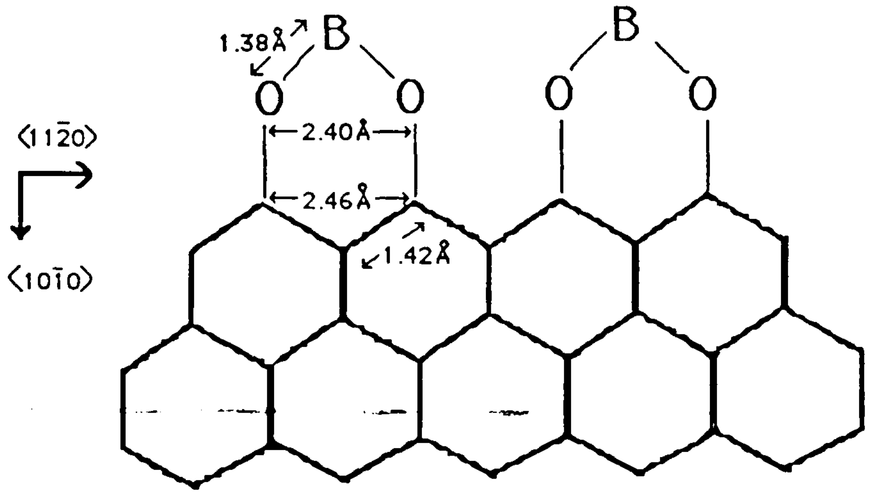

Figure 2 (from Ref. 12)

Thus, the reduction in oxidation rates caused by the addition of boron or phophorus compounds is probably due to a reduction in the number of available active sites. This is supported by a constancy of activation energy with the addition of such compounds (9).

Conclusion

From this model we propose that phosphorus and boron compounds (elemental, oxides and organic compounds) may be novel and effective reaction inhibitors for graphite fibers in an aluminum matrix. Furthermore, they may act to increase wettability through bond strengthening. Chemical deposition of boron or phosphorus on the graphite surface before consolidation may serve to delay the onset of carbide formation. Alloying the aluminum with borides (eg. AlB_2) or phosphides (eg. AlP) or intercalation of the graphite fibers with suitable boron/phosphorus compounds will provide a nearly infinite source of available boron or phosphorus to the interface, and may delay the formation of aluminum carbide indefinitely.

In summary, we propose the oxidation of graphite as a suitable model for the dissociation of carbon in Al/graphite composites. This model points to various substances (e.g. Al_2O_3, Al) present at the interface as catalysts of the dissociation of carbon (bond weakening) and others

(TiB_2, boron and phosphorus compounds) as inhibitors (bond strengthening). If effective, boron and phosphorus compounds have the potential to increase bond strength and wettability, and to inhibit the formation of Al_4C_3 in Al/graphite composites.

Acknowledgement: This research was supported by DARPA under contract ONR N00014-84-K-0687.

References

1. M. F. Amateau, "Progress in the Development of Graphite-Aluminum Composites Using Liquid Infiltration Technology," Journal of Composite Materials, 10 (1976).

2. L. Aggour, E. Fitzer, M. Heym, and E. Ignatowitz, "Thin Coatings on Carbon Fibers as Diffusion Barriers and Wetting Agents in Al Composites," Thin Solid Films, 40 (1977) 97-105.

3. I. H. Khan, "The Effect of Thermal Exposure on the Mechanical Properties of Aluminum-Graphite Composites," Met. Trans, 7A (1976) 1281.

4. D. Finello, "Interfacial Behavior of Graphite-Aluminum Composites" (Ph.D. thesis, The University of Texas at Austin, 1982).

5. S. D. Tsai, "The Characterization of the Interface in Graphite-Aluminum Composite Systems" (Ph.D. thesis, The University of Texas at Austin, 1980).

6. H. Mendez, D. Finello, R. M. Walser, and H. L. Marcus, "Correlation of Electronic State and Fracture Path of Aluminum-Graphite Interfaces," Scripta Met., 16 (1982) 855-858.

7. S. J. Baker and W. Bonfield, "Fracture of Aluminium-Coated Fibers," Journal of Materials Science, 13 (1978) 1329-1334.

8. K. Motoki and A. Okura, "Formation of Intermetallic Compound in Composite Materials," Progress in Science and Engineering of Composites, (T. Hayashi, ed.) 1281, North-Holland, 1982.

9. D. W. McKee, C. L. Spiro, and E. J. Lamby, "The Inhibition of Graphite Oxidation by Phosphorus Additives," Carbon, 22(3)1984) 285-290.

10. Rakszawski and Parker, "The Effect of Group IIIA-VIA Elements and Their Oxides on Graphite Oxidation," Carbon, 2 (1964) 53-63.

11. F. J. Long and K. W. Sykes, "The Effect of Specific Catalysts on the Reaction of the Steam-Carbon System," Proc. Roy. Soc. (Lond.) 215A (1952) 100.

12. D. W. McKee, C. L. Spiro, and E. J. Lamby, "The Effects of Boron Additives on the Oxidation Behavior of Carbons," Carbon, 22(6)(1984) 507-511.

APPENDIX F

Influence of aluminum oxide on the formation of aluminum carbide in the aluminum-carbon system.

Benji Maruyama, L. D. Brown, L. K. Rabenberg.

Abstract

Observations of reactions in thin film specimens show that the formation of aluminum carbide by solid state reaction at the interface between aluminum and carbon is catalyzed by the presence of a thin layer of aluminum oxide. Alternatively, the presence of a thicker oxide layer may serve as a diffusion barrier to impede carbide formation. These results support a model previously proposed .

Introduction

The formation of aluminum carbide in aluminum-graphite composites during primary and secondary forming operations is detrimental to the properties of the composite[1]. Investigators have shown that the lower limit for the temperature of formation of aluminum carbide is about 500°C[2]. Because aluminum carbide degrades the mechanical, as well as corrosion properties of the composite[1,3], it is therefore desirable to avoid or control carbide formation. Although the chemical and physical properties of the interface between aluminum and graphite in aluminum-graphite composites are crucial to its mechanical properties, the present understanding of the interface is poor. In particular, the influence on the interface of aluminum oxide, which is certainly present at the interface of commercial composites, is not well understood. A theoretical model has been developed that allows the characterization of bonding and chemical reactivity at the interface[4]. Specifically, the model allows the influence of various chemical species, especially oxygen and aluminum oxide, present at the interface to be evaluated. The results of experiments using a thin film physical model to test this theory are presented below.

Experimental:

A multi-layer thin film was chosen as an experimental model because it is easily analyzed in a transmission electron microscope. The films consisted of thermally deposited carbon, reactively deposited aluminum oxide and thermally deposited aluminum.

Graphite was avoided as a sample material because of its anisotropic reactivity, i.e. the basal plane edges are much more reactive than the basal plane faces. Instead, thermal carbon was chosen for a number of reasons: It is an isotropic material, it is easy to deposit in thin-film form. Thermal carbon is as reactive, if not more reactive than graphite basal plane edges[5], and its bonding is very similar to graphite[6].

Sample Preparation

The aluminum and carbon deposits were done in an Edwards 306A vacuum evaporator with a base pressure of at least 6×10^{-4} Pa. The carbon was from spectrographically pure carbon rods. The aluminum was from 99.995% pure aluminum foil.

The aluminum oxide film was made by thermally evaporating aluminum at 0.1nm/s in an oxygen atmosphere of 3×10^{-2} Pa. It was deposited onto the thermal carbon and was masked by a 400 mesh copper grid so as to form 6 micron square islands of aluminum oxide.

Film thicknesses were measured dynamically using a 5 Mhz crystal oscillator. All films were supported on pure aluminum grids, 200 mesh from Pelco Inc.

Various sample configurations were used. Initial samples were comprised of 25 nm of carbon under 50 nm of aluminum. Later, in order to reduce oxidation of the aluminum, the sample configuration was modified to include a 25 nm overlayer of carbon on the aluminum . Finally, in order to observe the effect of aluminum oxide on the system in a controlled manner, 50 nm of aluminum oxide was deposited on the carbon masked by a 400 mesh copper grid. This was followed by 50 nm of aluminum and 25 nm of carbon. This configuration allowed the observation of a triple-point interface, that is, the interface between the carbon, aluminum and aluminum oxide regions (see figure 1).

Heat treatments were performed in a quartz tube placed in a tube furnace at 600°C dynamically pumped to 3×10^{-5} Pa using an ion pump. Copper turnings were placed near the sample to act as an oxygen getter. Heat treatment times varied from 2 to 6 hours.

Analysis:

A JEOL 1200EX transmission electron microscope/ scanning transmission electron microscope (TEM/STEM) equipped with energy dispersive x-ray spectroscopy (EDS) and electron energy loss spectroscopy (EELS) capabilities was used to analyze the samples. EDS and EELS were used to check for impurities. Diffraction and microdiffraction were used to determine the presence or absence of aluminum carbide. The presence of aluminum carbide was indicated by the appearance of diffraction intensity at 0.166 nm $(11\underline{2}0)$, 0.28 nm $(10\underline{1}2)$, or the appearance of (0003) spots at 0.83 nm. Auger electron spectroscopy (AES) sputter profiling was done using a Physical Electronics 590 Scanning Auger Microscope.

Results:

Samples with the 25 nm carbon overlayer showed no detectable aluminum carbide formation when heat treated at 600°C for 2hrs (see figures 2). Samples given successive heat treatments of 2 and 4 hrs (total 6 hrs) showed a great deal of aluminum carbide formation (see figure 3). Masked aluminum oxide samples heat treated for 2 hrs at 600°C showed aluminum carbide formation. In some cases the formation was more prominent at the boundaries of the aluminum oxide island than at either the center of the island or away from the island. Figure 4 shows a view of an entire aluminum oxide square within the 200 mesh grid square of the sample. Figures 5 and 6: a, b, and c are selected area diffraction patterns of the area without aluminum oxide, the boundary area and the center of the aluminum oxide area, respectively. This suggests a catalytic effect at the boundaries where the oxide is thinner and a triple interface exists and a diffusion barrier effect at the center, where the thickness is greater. In other cases the island showed enhanced aluminum carbide formation throughout . The former result was seen to be the more common of the two.

Earlier samples were heat treated without a carbon overlayer in an atmosphere of greater oxygen content. These samples showed aluminum oxide formation on the exposed surface of the sample (as determined by Auger electron spectroscopy (AES) sputter profiling). Occasionally, the aluminum oxide would form as a dense patch where the aluminum was present in reduced amounts. In these areas there would invariably be enhanced carbide formation. It seems that the aluminum had receded from underneath the surface oxide. Such an occurrence would produce a configuration as is represented in figure 7. Notice that there is a triple interface between the aluminum, the carbon and the aluminum oxide. The enhanced carbide formation along with this hypothesis of its cause led us to the subsequent configuration of introducing the aluminum oxide in a controlled manner.

Discussion:

The results presented above partially confirm predictions of the oxidation model of aluminum carbide formation[4]. Briefly described, the oxidation model of aluminum carbide formation at aluminum-graphite interfaces makes an analogy between the oxidation of graphite in air and the formation of aluminum carbide at the aluminum-graphite interface. The steps in the formation of aluminum carbide are as follows. First, carbon atoms must be dissociated from the surface of the graphite fiber. Second, the dissociated carbon must diffuse through the surface oxide and already-formed carbide to the aluminum. Third, the carbon diffusing into the aluminum must form aluminum carbide. The relevant step pertaining to the chemical bonding of the interface is the first step. One theory on the oxidation of graphite in air occurs as follows[7]. First, oxygen is adsorbed onto the surface of the graphite. Second, an electron is transferred from the graphite to the carbon-oxygen pair forming a double bond between the carbon and the oxygen atoms and weakening the bond between the surface carbon atom and the graphite fiber. Third, the carbon oxygen pair dissociates, diffusing into the atmosphere. These three steps in the oxidation of graphite in air are believed to be applicable to the dissociation of carbon from graphite in the formation of aluminum carbide.

Thus oxygen present at the graphite surface can form an extremely strong bond between the oxygen and surface carbon at the expense of the bond between the surface carbon atom and the graphite fiber. Therefore, oxygen present at the surface of graphite can weaken the integrity of the surface and can be considered a catalyst for the dissociation of carbon from the surface of the graphite fiber.

As is well known, many substances enhance the oxidation of graphite in air[8]. Indeed, very few substances are known to inhibit the oxidation of graphite[9]. The catalytic action of these substances is believed to be due to the catalyst's ability to stabilize the state in which the bond between the surface carbon atom and the graphite is weakened. By our analogy then, the dissociation of carbon during the formation of aluminum carbide is believed to be catalyzed by the presence of the same substances which catalyze the oxidation of graphite in air, as well as by the presence of oxygen itself.

The results of previous samples showed us that the more success we had in eliminating oxygen and aluminum oxide from the system under the same conditions, the more resistant the sample was to aluminum carbide formation. Our best sample was the carbon/aluminum/carbon multi-layer which formed no detectable aluminum carbide when heat treated for 2 hours at 600°C. In previous samples of ours, for which there was no carbon overlayer and a poorer vacuum, carbide was formed. Kahn[1], using a carbon/aluminum film similar to ours with the same heat treatment also formed aluminum carbide.

As a result, we introduced aluminum oxide into our system in a controlled manner where the reaction of the triple interface (carbon, aluminum and aluminum oxide) could be observed. This system was considered to be a valid test model because aluminum oxide is certainly present at the interface of commercial composites and is likely to be present in many experimental models of the aluminum graphite system, and also because aluminum oxide is known to be a catalyst of graphite oxidation.

A comparison of the carbon/aluminum/carbon sample and the carbon/ aluminum oxide/ aluminum/carbon sample shows that, even though the samples had the same heat treatment, the oxide sample formed carbide whereas the sample without oxide did not.

These results bear numerous ramifications. The results suggest that, because aluminum oxide is present at the interface in commercial composites, the aluminum carbide reaction for a commercial composite is a catalyzed reaction (*i.e.*, the reaction would not occur as fast without any oxygen).

The results presented here also shed some light on previous investigations. The ability of aluminum oxide to catatalyze the dissociation of carbon from the fiber surface and,conversely the barrier to the diffusion of carbon which the aluminum oxide can pose if it forms a continuous layer are conflicting actions. For example, Finello et al. [10]have indicated that carbide formation rates increase with increasing pressure up to a point where oxidation of the aluminum is so great as to become a barrier to carbide formation. The results also suggests catalysis as the reason for previous investigators observation of aluminum carbide formation at low temperatures, down to 475°C[11].

Aluminum oxide catalysis of aluminum carbide formation must be recognized as a factor in experimental studies of such interface reactions. That is, the diffusion of oxygen through imperfection in aluminum coatings, through fiber ends and the supply of absorbed oxygen from the fiber itself will all affect the rate of carbide formation. A proper investigation of aluminum carbide formation should include a characterization of the oxide present at the interface and the affect the environment may have on the state of the interface.

But while aluminum oxide is certainly present at the interface of aluminum-graphite composites, it is a relatively mild catalyst to the oxidation of graphite in air. On the other hand, transition metals (as well as heterogeneous transition metal-alumina supported catalysts) are known to be strong catalysts of oxidation[7]. Of the transition metals, Fe, Cu are present in the largest amounts in alloys used for commercial aluminum-graphite composites and are therefore highly suspect as a cause of enhanced carbide formation. The presence of these elements may be a reason for the observation of carbide formation at temperatures lower that we have observed. At any rate, the influence of such elements, as with the influence of aluminum oxide must be evaluated and integrated into our understanding of the interface.

Conclusion

The aluminum carbide reaction at aluminum-carbon interfaces has been shown to be catalyzed by the presence of aluminum oxide. This catalytic action is naturally extended to aluminum graphite composites and also points to certain alloying elements or impurities present in commercial alloys as stronger catalysts. The results suggest that the chemical nature of the interface must be re-evaluated to include an understanding of how the bonding and chemical reactivity are affected by various substances present at the interface.

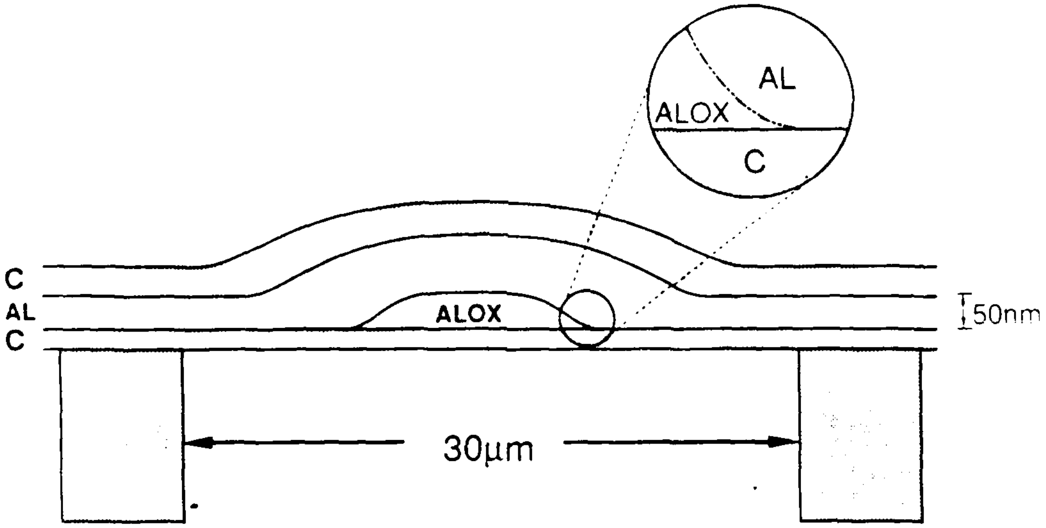
AL
ALOX
C
C
AL
ALOX
C
50nm
30µm

Figure1: Schematic of Carbon/Aluminum Oxide/Aluminum/Carbon Thin-Film Model.

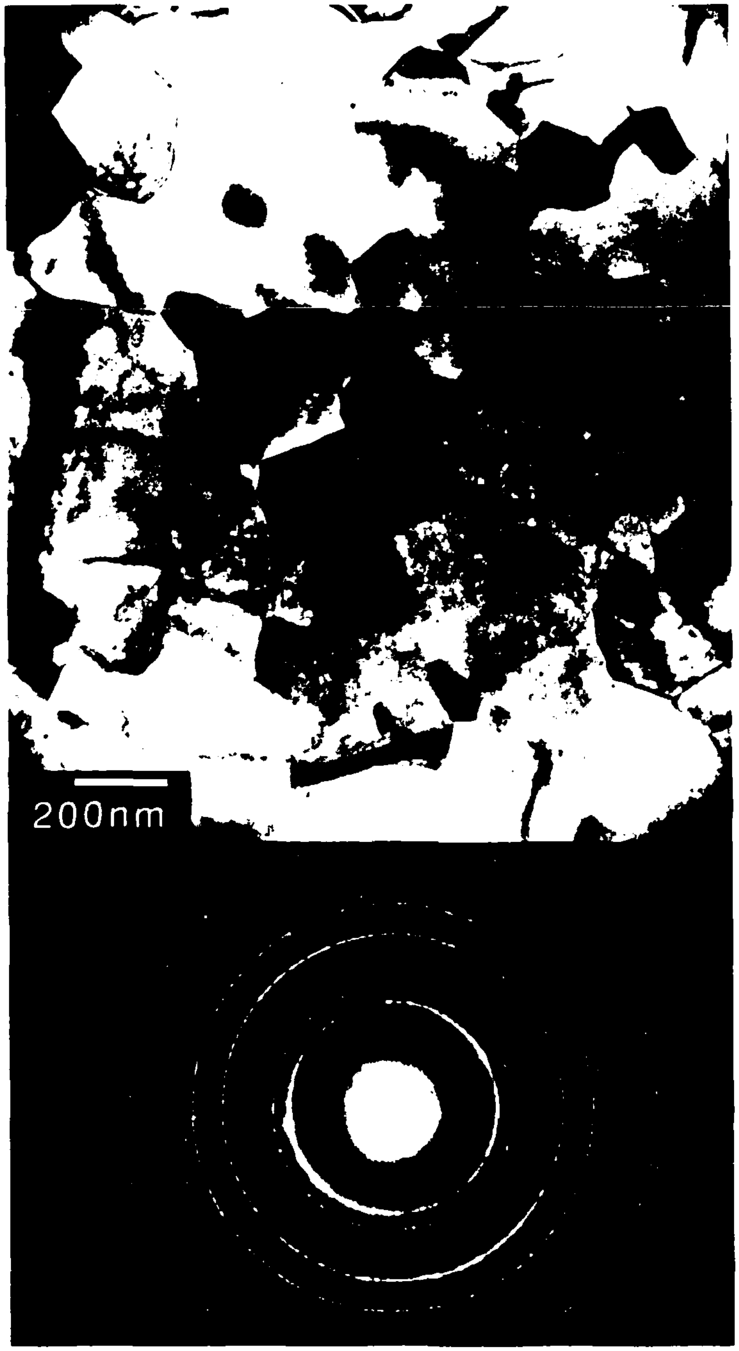

Figure 2: Carbon/Aluminum/Carbon Thin-Film Model heat treated for 2hrs, 600°C, no carbide formation.

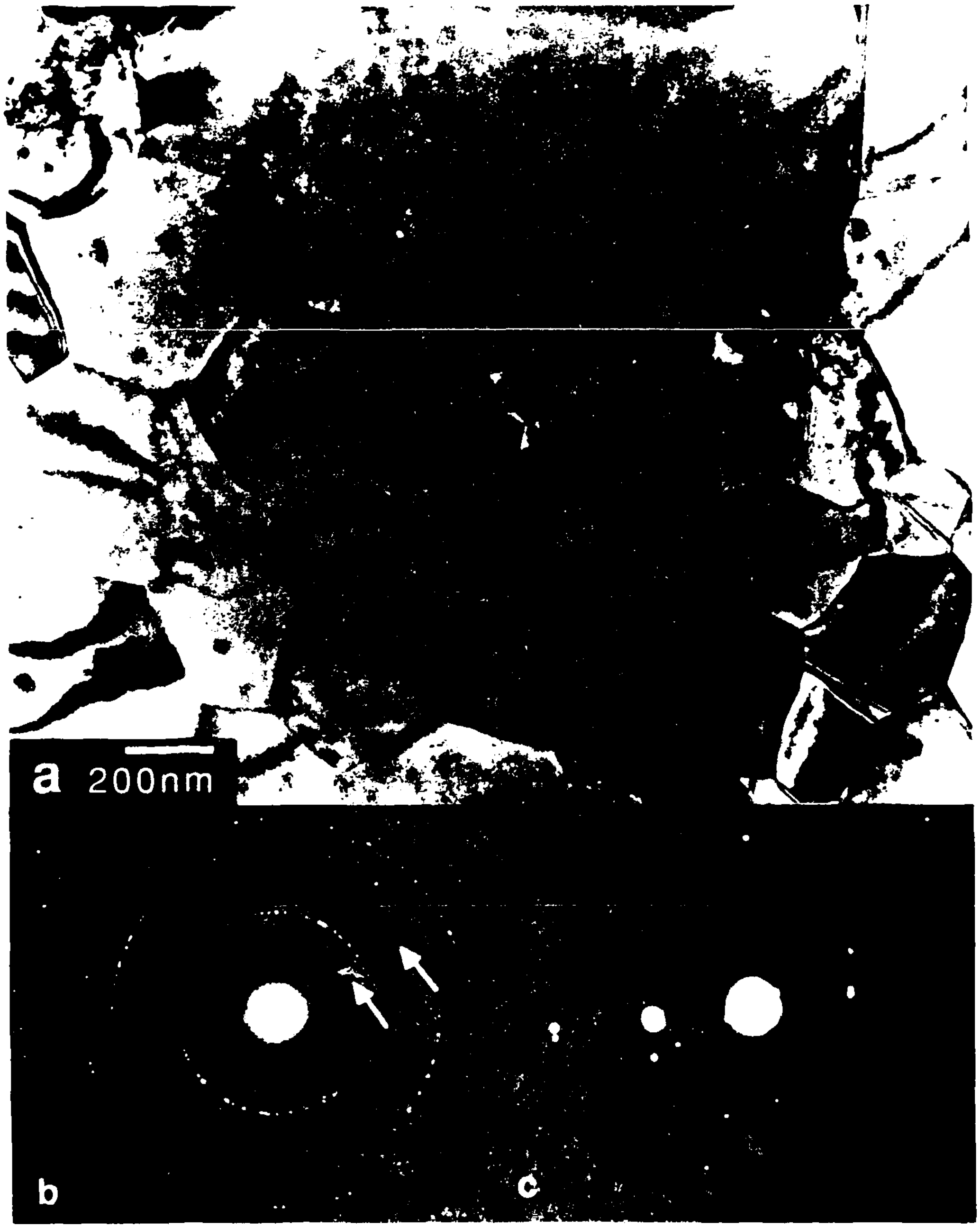

Figure 3. C[illegible] [illegible] treated for 2hrs and [illegible]

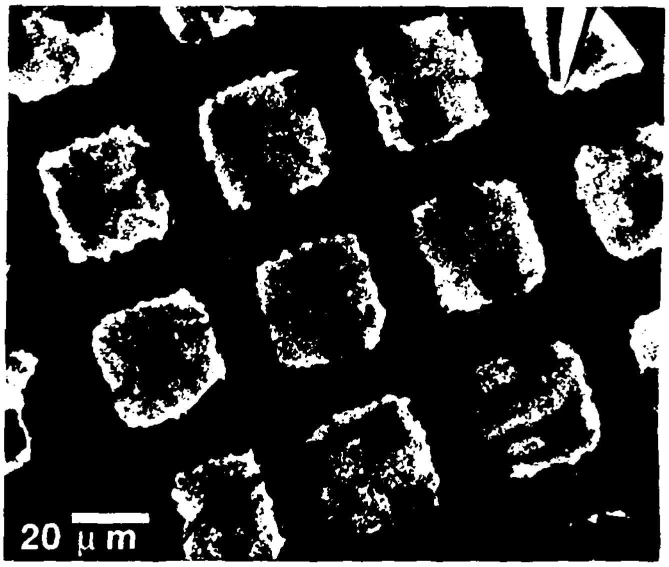

Figure 4: Carbon/Aluminum Oxide/Aluminum/Carbon Thin-Film Model: Dark islands within 200 mesh grid are aluminum oxide.

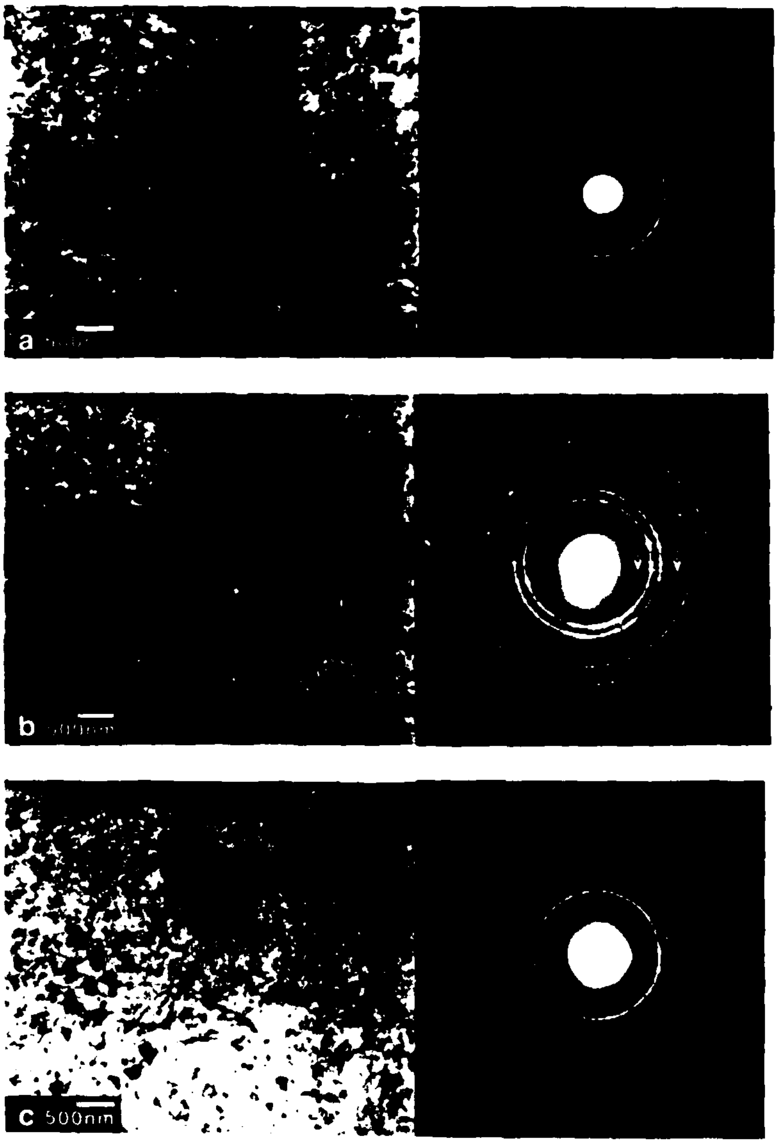

Figure 5: Carbon/Aluminum Oxide/Aluminum/Carbon Thin-Film Model. heat treated 2hrs., 600°C, a is the aluminum area, b is the border of the aluminum oxide island, and c is the center of the aluminum oxide island.

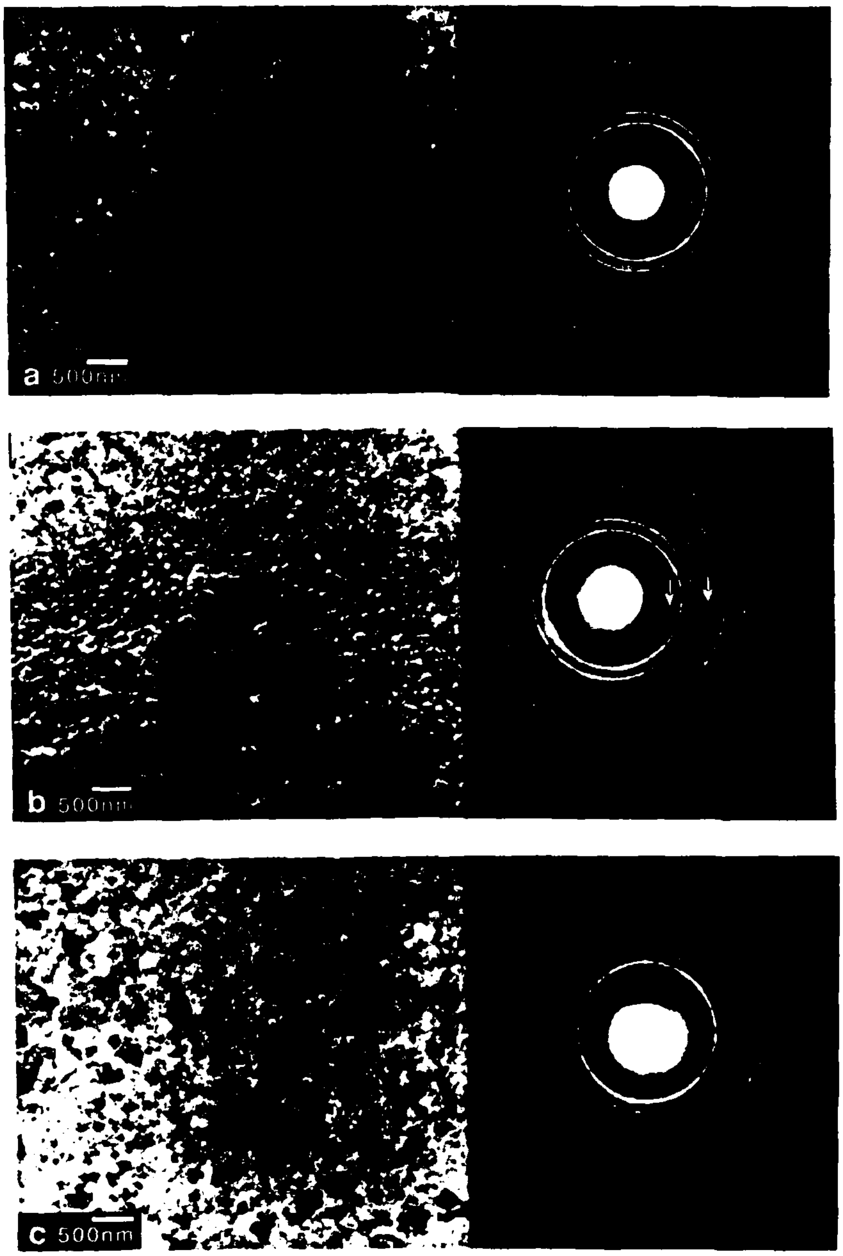

Figure 6: Carbon/Aluminum Oxide/Aluminum/Carbon Thin Film Model. Heat treated 2hrs., 600°C, a is the aluminum area, b is the border of the aluminum oxide island, and c is the center of the aluminum oxide island

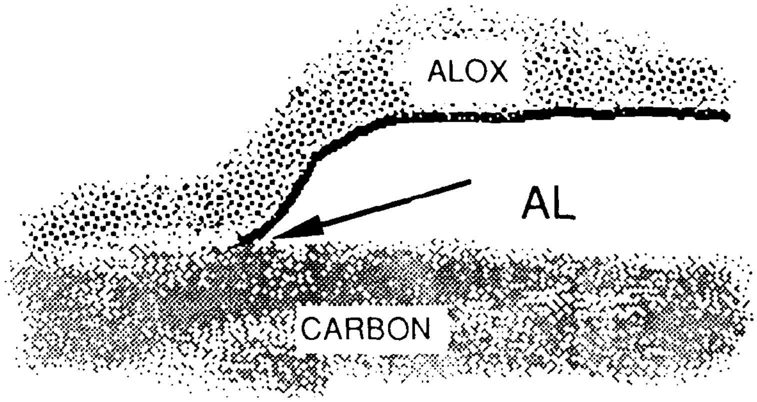

Figure 7: Surface Aluminum Oxide/Aluminum/Carbon Thin-Film schematic. Aluminum receding from under a surface oxide produces such a configuration. Arrow points to triple point between aluminum, aluminum oxide and carbon.

References

1 I. H. Khan. "The Effect of Thermal Exposure on the Mechanical Properties of Aluminum-Graphite Composites." Met. Trans. 7A (1976) p. 1281.

2 A. A. Baker. "Carbon Fiber Reinforced Materials-- A Review of Current Technology." Mat. Sci. and Eng. Vol. 17 (1975) pp.177-208.

3 D. M. Aylor, P. J. Moran. "Effect of Reinforcement on the Pitting Behavior of Aluminum-Base Metal Matrix Composites." J. Electrochem. Soc.: Electrochemical Sci. and Tech. Vol. 132, No. 6 (1985) pp. 1278-1281.

4 Benji Maruyama, L. K. Rabenberg. "Oxidation Model of Interface reactions in Aluminum/Graphite Composites." in Interfaces in Metal Matrix Composites, A. K. Dhingra and S. G. Fishman, eds., (AIME, Warrendale, PA 1986), p. 233.

5 S. R. Kelemen, H. Freund. "A Comparison of O_2 and CO_2 Oxidation of Glassy Carbon Surfaces." Carbon, **23** 6 (1985) pp. 723-729.

6 R. F. Egerton, M. J. Whelan. "Electron Energy Loss Spectra of Diamond, Graphite and Amorphous Carbon." J. Electron Spectroscopy and Related Phenomena, 3 (1974) pp. 232-236.

7 F. J. Long, K. W. Sykes. "The Catalysis of the Oxidation of Carbon." Proc. Roy. Soc. (Lond.) 215A (1952) 361.

8 J. F. Rakszawski, W. E. Parker. "The Effect of Group IIIA-VIA Elements and Their Oxides on Graphite Oxidation." Carbon 2, (1964) p.53-63.

9 D. W. McKee, C. L. Spiro, E. J. Lamby. The Inhibition of Graphite Oxidation by Phosphorus Additives." Carbon, **22** 3 (1984) pp. 285-290.

10 D. Finello. Doctoral Dissertation, The University of Texas at Austin, 1982.

11 M. Shorshorov, T. Chernyshova, L. Koveleva. "Interface Interaction in Aluminum-Carbon System." Progress in Science and Engineering of Composites, T. Hayashi, ed. p. 1273, North-Holland, 1982.

APPENDIX C

Residual Stresses in Composite Materials

Yong-Moo Cheong* and H. L. Marcus**
Center for Materials Science
and Engineering
The University of Texas
Austin, TX 78712

ABSTRACT

Residual stress is a significant property of composite materials from the point of view of both practical applications and mechanical response. The paper presents a short review of the various residual stress measurement techniques that have potential use in filamentary and planar composites. The origin of the residual stresses at the interface between matrix and fiber are discussed. They involve differences in coefficient of expansion between the components as well as differences in mechanical response. The potential measurement techniques include x-ray, neutron, optical, ultrasonic and magnetic probes. Some of the advantages and limitations for each method in measuring residual stresses in composites are discussed.

---

*Graduate Student

**Harry L. Kent Jr. Professor of Mechanical Engineering

NOMENCLATURE

γ_0 :	Gruneisen parameter
d	Fiber diameter
$d_{\phi,\psi}$	Interplanar spacing along the direction tilted the angle ϕ and ψ from the surface normal
d_0	Interplanar spacing between (hkl) planes
ε'_3, ε'_{33}	Strain normal to the surface
ε	Strain calculated from the difference of thermal expansion coefficents
E	Young's modulus
exp	Exponential base of natural logarithm
I	X-ray intensity
l	Distance between the fibers
l	Path length
ln	Natural logarithm
μ	X-ray linear absorption coefficient
ν	Poisson's ratio
σ_i, σ_1, σ_2, σ_3	Principal stress
σ_{ij}	Stress tensor component
σ_ϕ	Stress along the direction tilted at the angle ϕ from the surface normal
σ_y	Yield stress
S'_{ij}, $S_{i[hkl]}$	Compliance tensor corrected by rotation matrix transformation from [hkl] to [001]
τ	Penetration depth
V	Volume
ω_0	Incident photon frequency
z	depth

INTRODUCTION

Residual stress in composite materials is one of the important properties to characterize the material performance. However, it is not easy to measure the residual stress field accurately, since the composite materials are inherently *heterogeneous material systems.* *The intrinsic nature of the residual* stress that is associated with no external forces is that every residual stress system has zero resultant force for the body to be in equilibrium. This stress state is very difficult to determine in the heterogeneous composite systems.

Residual stresses are introduced into materials by *any process - mechanical,* thermal, or chemical - that results in a permanent, nonuniform change in shape or volume(1-3). From the theoretical viewpoint, thermal stresses, which are introduced upon cooling from the manufacturing temperature, if the matrix and fiber have different coefficients of thermal expansion, are expected to be the *most significant sources of residual stresses* in composite materials. For exemple, in the unidirectional aluminum matrix-graphite fiber composites, there is a mismatch of approximately $23 \times 10^{-6} \, ^{\circ}C^{-1}$ in the thermal expansion coefficients in the longitudinal direction. The composites are cooled by almost 600°C after solidification, giving rise to significant amounts of residual stresses(4,5). Thus internal stresses are developed at the interface due to thermal strain incompatibilities between the elastic fiber and the elastic-plastic matrix. Plastic flow in the matrix is expected to occur if the state of stress at the interface is above the appropriate flow stress criterion of the matrix.

Unfortunately, in many of the experimental approaches that are in use to obtain residual stresses, the detailed understanding of the relationships between the measurable parameters and the residual stress state are not sufficiently developed uniquely to distinguish the details of the stress states. Actually no experimental technique measures stress directly. X-ray diffraction, the most advanced approach to obtaining residual stress information, measures lattice strains relative to a standard at the same temperature while the other techniques measure the physical or mechanical properties which are modified by residual stresses

As the composite materials are becoming more broadly used, the need to quantify the role of residual stresses and to determine their magnitude have led to attempt improving the measurement techniques. This paper discusses some of the new improvements and methods to quantitatively determine the residual stresses.

ORIGIN OF RESIDUAL STRESSES AT THE INTERFACES

When a fiber or film and its tightly bonded matrix have different thermal expansion coefficients, changing the temperature of the combination will introduce strain into the matrix. Murbach and Wilman(6) measured stress in deposits of various metals and concluded the amount of stress developed depend on the difference between the final deposit temperature and recrystallization temperature or the highest temperature reached if this is less than the recrystallization temperature. When the crystals are growing at the deposit surface by addition of arriving atoms they are thermally expanded. As this layers become covered by further growth of deposit, their temperature must decrease progressively in accordance with the temperature gradient in the deposit, and the crystals must contract. Appreciable atomic migration persists and causes readjustments at and near the grain boundaries, i.e. recrystallization, until the temperature falls below the recrystallization temperature, and thereafter the further cooling must cause a tensile stress to be developed throughout the deposit(6).

Composites are generally classified as unidirectional fiber, random fiber and laminate as shown schematically in Fig 1. Longitudinal residual stress is much greater than transverse stresses in the unidirectional fiber composites. Laminate composite can be regarded as having an isotropic stress system in the plane of laminate and no stress normal to the plane of laminate exists in the ideal condition. It is a good assumption that a net isotropic residual stress exists in the random fiber composites, but the interface between the matrix and disperoid will define the residual stress state. This will be strongly dependent on the l/d ratio, l the length

of the random fiber and d the diameter Vook and Witt (7-9) calculated the strain in metal film based on the following assumptions, (1) The film is firmly attached to the substrate (2) The thermal expansion of film and substrate are isotropic in the plane of the substrate (3) The stress on the film in a direction normal to the plane of the film is zero (4) The shear strain in the plane of the film is zero (5) The metal film is single crystal
The results are expressed by (7)

$$\frac{\varepsilon_3'}{\varepsilon} = \frac{S_{31}'(S_{12}' - S_{22}') + S_{32}'(S_{12}' - S_{11}')}{(S_{12}')^2 - S_{11}' S_{22}'} \qquad (1)$$

,where ε_3' is the strain along the axis normal to the surface corrected by rotation matrix transformation from [hkl] vector to [001], is the strain calculated from the thermal expansion coefficients, and the S_{ij}''s are the compliance tensor components corrected by rotation matrix transformation from [hkl] vector to [001] To check these basic calculations, x-ray diffraction measurements of the lattice parameters were made The as-deposited and annealed films show large variations in measured lattice parameters, probably due to lack of experimental precision and presence of varying tensile and compressive thermal strains in the different grains resulting from variation in the adhesion of the film to the substrate (9) The experiments were inconclusive in evaluating the model

X-RAY and NEUTRON DIFFRACTION

The principles of determining the residual stress with x-ray diffraction have been described in several sources (3,10,11) For the particular application to the composite materials, $\sin^2\psi$ method (12,13) is generally used. Assuming only biaxial stresses are present ($\sigma_3=0$), a good assumption for thin laminate, the following was developed (11) The strain along the direction tilted the angle ϕ and ψ from the surface normal is given by

$$\varepsilon_{\phi,\psi} = \frac{d_{\phi\psi} - d_0}{d_0} = \left(\frac{1+\nu}{E}\right)\sigma_\phi \sin^2\psi - \frac{\nu}{E}(\sigma_1 + \sigma_2) \qquad (2)$$

In this expression, the quantity σ_1 and σ_2 are the principal stresses within the plane, σ_ϕ is the stress in the plane of surface of the sample in the direction defined by the angle, ϕ, as shown in Fig 2, and ν and E are poisson's ratio and the elastic modulus of the material The surface stress at angle ϕ is given by

$$\sigma_\phi = \sigma_1 \cos^2\phi + \sigma_2 \sin^2\phi \qquad (3)$$

$$\frac{d_{\phi,\psi=0} - d_0}{d_0} = \frac{-\nu(\sigma_1 + \sigma_2)}{E} \qquad (4)$$

Substitute these equations into eq(2), we have

$$\frac{1+\nu}{E}\sigma_\phi \sin^2\psi = \frac{d_{\phi\psi} - d_{\phi,\psi=0}}{d_0} \cong \frac{d_{\phi\psi} - d_{\phi,\psi=0}}{d_{\phi,\psi=0}} \qquad (5)$$

From the slope of $d_{\phi\psi}$ vs $\sin^2\psi$ plot, σ_ϕ can be determined

Let m* be the slope of $d_{\phi\psi}$ vs $\sin^2\psi$ plot

$$m^* = \frac{\partial d_{\phi\psi}}{\partial \sin^2\psi} \qquad (6)$$

Then

$$\sigma_\phi = \frac{m^*}{d_{\phi,\psi=0}\left(\frac{1+\nu}{E}\right)} \qquad (7)$$

This method of measurement is relatively simple and easy to get the quantitative residual stress data in the laboratory or in the field In reality, however, nonlinear d vs. $\sin^2\psi$ distributions have been observed in the residual stress measurement, which can be explained by the multiaxial stress state, stress gradients, and/or elastic anisotropy (14-17) In polycrystalline materials, only those grains properly oriented to diffract at each tilt contribute to the diffraction profile. This selectivity implies that the elastic constants connecting the measured strains will vary with particular set of planes (hkl) chosen for measurement

The classical principles briefly described above assumed only two principal stresses on the surface and other stress terms are zero Stress tensor components are expressed by

$$\begin{pmatrix} \sigma_1 & 0 & 0 \\ 0 & \sigma_2 & 0 \\ 0 & 0 & 0 \end{pmatrix} \qquad (8)$$

In addition to the above tensor component expression, the possible residual stress states of materials are

$$\begin{pmatrix} \sigma_{11} & \sigma_{12} & 0 \\ \sigma_{12} & \sigma_{22} & 0 \\ 0 & 0 & 0 \end{pmatrix} \qquad \begin{pmatrix} \sigma_1 & 0 & 0 \\ 0 & \sigma_2 & 0 \\ 0 & 0 & \sigma_3 \end{pmatrix} \qquad \begin{pmatrix} \sigma_{11} & \sigma_{12} & \sigma_{13} \\ \sigma_{21} & \sigma_{22} & \sigma_{23} \\ \sigma_{31} & \sigma_{32} & \sigma_{33} \end{pmatrix}$$

(9) (10) (11)

While the tensor expressions (8,9) represent (residual or applied) stresses in free surfaces, the tensor expressions (10,11) may represent residual stress state in the interior of a material or stress states caused by multiaxial loading. The general expression considering all nine stress tensor components are given by (14)

$$\frac{d_{\phi\psi} - d_0}{d_0} = \varepsilon'_{33} = \frac{1}{2} S_2(hkl) \left[\sigma_{11} \cos^2\phi + \sigma_{12} \sin 2\phi + \sigma_{22} \sin^2\phi \right] \sin^2\psi$$
$$+ \frac{1}{2} S_2(hkl) \sigma_{33} \cos^2\psi + S_1(hkl) \left[\sigma_{11} + \sigma_{22} + \sigma_{33} \right] \qquad (12)$$
$$+ \frac{1}{2} S_2(hkl) \left[\sigma_{13} \cos\phi + \sigma_{23} \sin\phi \right] \sin 2\psi$$

For the tensor expressions (8), (9) and (10), d vs $\sin^2\psi$ is linear, even though the tensor expression (9) and (10) have additional terms. However, the tensor expression which represents the most general stress state, (11) is no longer linear d vs $\sin^2\psi$ and the terms σ_{13} and σ_{23} in the tensor expression (11) have a sin 2ψ dependence. This effect has been termed 'ψ splitting' (14)

The influence of stress gradients also results in the nonlinearity of d vs $\sin^2\psi$. X-ray penetration depth is one of the important factors considering the effect of stress gradients. Assume the stress component, σ_{ij} depend only on the depth, z and local strain, $\varepsilon_{33}(\phi,\psi,z)$, are caused by local stress, $\sigma_{ij}(z)$. The intensity dI reflected by unit volume, dV at the depth, z can be written by

$$dI \simeq \exp(-\mu l)\, dV \qquad (13)$$

where l is the path length of the x-ray beam within the sample and μ is the linear absorption coefficient. The path length l depend on ψ and Bragg angle θ

$$l = \frac{2Z \sin\theta \cos\psi}{\sin^2\theta - \sin^2\psi} \qquad \text{(for } \Omega\text{-goniometer)} \qquad (14)$$

$$l = \frac{2Z}{\sin\theta \cos\psi} \qquad \text{(for } \psi\text{-goniometer)} \qquad (15)$$

Thus the penetration depth, τ, which corresponds to $e^{-\mu l} = e^{-1}$, becomes

$$\tau = \frac{\sin^2\theta - \sin^2\psi}{2\mu \sin\theta \cos\psi} \qquad \text{(for } \Omega\text{-goniometer)} \qquad (16)$$

$$\tau = \frac{\sin\theta \cos\psi}{2\mu} \qquad \text{(for } \psi\text{-goniometer)} \qquad (17)$$

When measuring the residual stresses of metal matrix composites by using x-ray diffraction, x-ray penetration depth gives rise a fundamental problem. A schematic of stress distribution in metal matrix composites in longitudinal direction is expected as shown Fig 3. The dotted line can represent the fixed strain condition, as may be expected from a continuum viewpoint, and the solid line is one of possibilities of the non-homogeneous residual strain. In the aluminum-graphite composites, x-ray penetration depth using typical laboratory x-ray sources, satisfies both of those conditions since the fiber is about 10μm and for reasonable volume fractions the distance between fibers is about the same. Thus the stress values measured by x-ray diffraction are merely the volume average stresses.

In composites such as continuous SiC fiber in Ti matrix where the fiber diameter is about 150μm, the x-ray penetration depth is less than one fiber depth. This makes x-ray residual stress measurements extremely difficult to make and interpret. One way to avoid this dilemma would be to use neutron diffraction with its much greater penetration depth([illegible]). The principle of neutron diffraction techniques is based essentially on that same Bragg relation as x-ray diffraction This would be plausible in the laboratories with the wide angle neutron diffraction capability, available only from research nuclear reactor, but it would not be generally available

In the fracture mechanics of composites, the most significant factor is the stresses at the interface between fiber and matrix, a value expected to be different from the volume average stress, since the thermal expansion strain mismatch would be maximum at the interface The stress at the interface between the graphite fiber and aluminum matrix is expected to be well above the yield strength of aluminum matrix when the composite has been cooled from the liquidus region to room temperature This results in plastic flow in the vicinity of the interface

Although it is almost impossible to get a sharp x-ray diffraction peaks in the polymeric materials, residual stress in graphite/epoxy composites can be measured by x-ray diffraction peak from the filler particles (20-23) In principle, if small amounts of crystalline filler particles are dispersed at the interfaces in the polymeric composites, the particles are responsive to both applied and residual stress Filler particles, Ag, Nb, and CdO, sized 1-30 μm, dispersed in small amounts between the plies in unidirectional graphite/epoxy laminate, are found to be satisfactory with Cu Kα radiation (22) Stresses at a surface can be measured when the crystalline particles are dispersed in a thin layer of resin coated on the surface, and stresses at interior positions can be measured with particles dispersed more deeply throughout the interior The use of two different disperoids, one at each location allows both measurements to be made simultaneously

OPTICAL METHOD (RAMAN SPECTROSCOPY)

When a crystal is exposed to a monochromatic optical wave (laser), photons are inelastically scattered by the phonons (lattice vibrations) If photons are interacted with optical phonons, the photon frequency shifts, so called Raman shift, are observed (24) The change in photon frequency of light during the scattering events involves the creation or annihilation of phonons (25,26)

When a uniaxial stress is applied, Raman peaks exhibit splitting and shifts which are linear in the applied stresses (27). The proportionality constants of Raman peak shifts to hydrostatic stress components, are defined by,

$$\gamma_0 = -\frac{\partial \ln \omega_0}{\partial \ln V} \qquad (19)$$

where γ_0 is the Gruneisen parameter, ω_0 is incident photon frequency, and V is volume interacted with photons.

By using group theoretical manipulations (28,29), Raman tensors (polarizability tensors) can be determined for a given crystal structure or crystal symmetry group. Once the Raman tensors are known, it can be determined whether a given geometry of experimental system shows a Raman active or inactive mode. The deformation potential theory based on the phenomenological Hamiltonian which assumed the Hamiltonian is linear function of strain, results in deformation potential constants for a given Raman mode of the materials. The relation between the stress and Raman peak shift can be determined from the information on the deformation potential calculated from the Raman peak shift measurements under a given uniaxial stress. Strain induced Raman splitting and shifts in the diamond structure are well developed (30). A great deal of literatures on the deformation potentials and stress induced Raman peak shifts are available for the single crystal, silicon (27,31,32), germanium (31,33,34), diamond (30), α-quartz (35-37), and sapphire (38). The fundamantal questions that are introduced as to the feasibility of the Raman method is in terms of how easily the peaks can be detected and how sensitive to the stress the Raman line is. It is difficult to apply this method to metals because the intensities of observed Raman lines in metals are quite small, in some cases no Raman active mode exists because of no optical phonon branch or due to symmetry considerations. Scattering takes place only within the skin depth, while at the same time the large impedance mismatch between the metal and vacuum results in a low efficiency for transmission of energy into or out of the medium (39). However, the materials which have diamond structure (O_h symmetry group), or uniaxial structure (D_3 or D_{3d} symmetry group) show

Raman active peaks

The stress level of 100 MPa (= 10^9 dyne/cm^2) generally correspond to the Raman shift of one wavenumber or less. Therefore very accurate measurements are needed for detecting the stress on the materials. Raman scattering spectra is one of the excellent tools to characterize the stress state during the production and annealing process for the semiconductor laminate composites. It is known that a built-in stress of the order $10^8 - 10^9$ dyne/cm^2 exists in the silicon epitaxial film grown on the sapphire wafer (000), which can be calculated from the thermal expansion coefficients of silicon and sapphire (40). The thermal expansion coefficients of sapphire is roughly twice that of silicon (41), causing a room temperature lateral strain of -3×10^{-3} upon cooling down from the growth temperature of around 1000°C in the chemical vapor deposition (CVD) method (42). The existing strain in silicon films on sapphire was found to be 7 kbar (=700 MPa) at room temperature with an accuracy of about ± 0.3 kbar (40). The amounts of stress relieved by laser annealing of silicon on sapphire (SOS) were also determined by Raman spectroscopy (41-44).

Raman spectroscopy is a very selective method. The materials should belong to the symmetry group which shows the Raman active mode and the intensity of Raman peaks should be large and detectable. Generally metals are excluded from these categories. If residual stress in opaque composites are to be measured the back-reflection geometry is required. The optical penetration depth of materials must be considered for the composite and optical wavelength used. For the 488 nm line of an argon laser, the penetration depth is 1000 nm for single crystal silicon and about 100 nm for the amorphous silicon (45).

The shift and broadening of the Raman frequencies are observed in the polycrystalline silicon (46). The shift toward low frequencies is attributed to the macroscopic strain induced during the laser annealing and the Raman linewidth in annealed polycrystalline silicon layers is mainly governed by the phonon damping caused by the lattice damage and grain boundaries (46). Raman shifts under tensile loading of aluminum on α-quartz has also been reported (47).

ULTRASONIC METHODS

The basic idea for ultrasonic stress measurements is that so called acousto-elastic effect on the stressed materials. The stress applied to solids results a change in interatomic distances which cause a change in the acoustic wave velocity (48,49). The acoustic wave velocity can be expressed in terms of second- or third order elastic constants from the equation of motion, which is derived from nonlinear stress-strain relation for a given crystal symmetry by substituting plane-wave solutions (48). The third order elastic constants play a major role in the anharmonic behavior of crystal lattice and relate stress to strain in nonlinear finite elastic theory (50). The third order elastic constants can be determined from the measurement of wave velocity variation on small amplitude acoustic wave under conditions of hydrostatic pressure or uniaxial stress. Longitudinal, transverse (shear), or surface (Rayleigh) waves can be used for stress measurements. The acousto-elastic effect have been observed in anisotropic, stress-free materials and is attributed to the birefringent nature of materials to the ultrasonic radiation, i.e., the difference in the velocity of propagation of the two polarized wave components. Elastic stiffnesses of glass/epoxy composites are measured by ultrasonic velocity method (51). It is shown that the Young's modulus, calculated from the elastic stiffness, are greatly depend on the fiber orientations. The difference in the time of flight of shear waves is proportional to the applied stresses introduced by the three-point bending (52).

Generally the ultrasonic method measures the bulk average values of residual stresses, because the wavelength of ultrasonic waves is much greater than the fiber diameter or the distance between the fibers in most composite materials. In many cases, the integral of the residual stress components through the thickness of the sample must be zero for the internal forces in the materials to be balanced in the absence of externally applied forces. There are two major problems hindering the effective use of the acoustic birefringe technique (53). First because the stress induced velocity changes between the two components of acoustic waves are relatively small (in the order of 0.5

percent or less), sensitivity is limited. Second, since factors other than stress, such as preferred orientation (texture), can cause an acoustical birefringence correlation. Measurements are needed to relate the observed velocity changes to known stress distributions or degrees of preferred orientation.

SAW (Surface Acoustic Wave, or Rayleigh wave) can measure the surface properties of materials, however, only average values from the surface to at least one wavelength depth can be measured. For example, at a few MHz, the penetration depth of Rayleigh waves is of the order of a millimeter. It can be possible to probe a planar interface by sequentially changing the penetration depth by changing the frequency. The velocity of Rayleigh waves is sensitive not only to stress but also to microstructural variations from point to point on the materials, such as preferred orientation, dislocation density, temperature, etc., and because the Rayleigh wave velocity at zero stress is unknown, only relative measurements of stress can be performed (54). Thus, in practical applications, one must carefully calibrate the measurement system relative to the particular composite materials being investigated, and even if this is done the results have large experimental scatter. A great deal of additional research effort will be required before ultrasonic methods could be considered a promising method to measure the residual stress in composites.

MAGNETIC METHODS

Many stress-sensitive magnetic properties, such as magnetostriction, magnetic anisotropy, Barkhausen noise, hysteretic effect, etc., can be used for residual stress measurement. At the present stage of development, however, the detailed theory relating these properties to residual stress is not available because of complications introduced by the irreversible nature of ferromagnetic phenomena and resulting hysteresis effect, and their microstructural dependences(55). In the following, the principles of both Barkhausen noise and the magnetostriction (magneto-elastic effect) are briefly described.

As the applied magnetic field is increased continuously, the magnetization of ferromagnetic materials does not increase in a strictly continuous way, but rather by small, abrupt discontinuous increments, called Barkhausen jumps or Barkhausen noise. Such jumps are caused, principally, by the discontinuous movements of mobile magnetic boundaries (Bloch walls) between adjacent magnetic domains and occasionally by the initiation of new magnetic domain walls. Furthermore, the direction and magnitude of mechanical stress existing in macroscopic ferromagnetic specimen strongly influences the detailed dynamics of the domain wall motion and correspondingly influences the Barkhausen noise (56). When an annealed metal is subjected to cyclic stressing with a constant stress amplitude, the dislocation arrangements affect the motion of the domain walls which cause increased small scale jerkiness in this motion (57). When the materials and its processing are known and combined with suitable calibration data are available, it is possible to achieve some degree of quantitative residual stress measurements on the ferromagnetic materials.

When a magnetic field is applied to the ferromagnetic materials, materials also respond by expanding or contracting. This phenomenon is called magnetostriction or magnetoelastic effect. Magnetostriction is a reversible phenomenon between the strain and magnetization. The physical origin of the magnetostriction is an interactions of the magnetic spins which are at the lowest free energy state due to an interaction between the spin rotation and crystalline anisotropy. This results in induced mechanical strain from the distorted electron clouds in the nuclear structure (58). Applied force can cause the change of strain induced by the magnetization or the change of magnetization itself. Thus the measurement of the change of magnetization or strain by applied forces can be converted to stress based on the calibration data. For the appropriate composite system containing magnetic components, magnetic approaches described do offer limited hope to determine the residual stresses.

SUMMARY

It has been attempted to present a picture of the present status of the measurement of the residual stresses in the composite materials by describing the methods used to determine them. The differences in coefficient of thermal expansion between matrix and fiber is expected to play a major role in generating the residual stresses in composite materials. At present time, x-ray diffraction is the most effective and reliable technique for the measurement of residual stresses in composites and may serves as a calibration tool for all other techniques. The other techniques for residual stress measurement for composites suffer from many inherent unknowns and limitations. Neutron diffraction could be a promising technique for a appropriate composite system since it has an advantage with its much greater penetration depth compared to x-ray diffraction. Raman scattering is one of the powerful optical methods for semiconductor laminate composites, especially Si and SiO_2 but this method generally won't be suitable for metal composites.

All residual stress measurement methods described in this paper are non-destructive methods. Any advancement of the method described or new fundamental approaches to measure residual stress will greatly aid in the complex problems of determining the residual stresses in composites.

ACKNOWLEDGEMENT

This work was supported by the DARPA under the ONR contract No. N 00014 - 84 - K - 0687 at the University of Texas

REFERENCES

1 Noyan I. C and Cohen J.B. (1982) The Nature of Residual Stress and Its Measurement, Residual Stress and Stress Relaxation, Eric Kula and Volker Weiss eds., Plenum Press., pp 1-17

2 Leonard Mordfin (1981) Measurement of Residual Stress: Problems and Opportunities, in Residual Stress for Designers and Metallurgists, Proceedings of a Conference held 9-10 April 1980, Chicago, Il., Larry J Vande Walle eds., American Society for Metals, pp 189-210

3 Hilley M. E., Larson J. A., Jatczak C.F., and Ricklefs R.E. eds (1971) Residual Stress Measurements by X-Ray Diffraction, SAE Information Report J784a

4 Swe-Den Tsai, Deepak Mahulikar, and Marcus H.L., Ismail C Noyan and Cohen J B (1981) Residual Stress Measurements on Al-Graphite Composites Using X-Ray Diffraction, Materials Sci. & Eng., 47, pp 145-149

5. Swe-Den Tsai (1980) PhD Dissertation, The Univ. of Texas at Austin

6. Murbach H.P and Wilman H. (1953) The Origin of Stress in Metal Layers Condensed from the Vapor in High Vacuum, Proc. Roy. Soc. (London) Ser B, 66, pp 905-910

7. Vook R.W. and Witt F. (1965) Thermally Induced Strains in Evaporated Films, J. A [illegible] 's., 36, (7), pp 2169-2171

8 W[illegible] r. and Vook R.W (1968) Thermally Induced Strain Cubic Metal Films, J Appl. Phys., 39 (6), pp 2773-2776

9 Vook R.W. and Witt F. (1965) Structure and Annealing Behavior of Metal Films Deposited on Substrates Near 80°K I Copper Films on Glass, J Vac Sci Tech., 2, pp49-57

10 Barrett C.S. and Massalski T.B. (1966) Structure of Metals, 3rd ed. Mcgraw-Hill Inc.

11 Cullity B.D (1977) Elements of X-Ray Diffraction, 2nd ed. Addison - Wesley Publishing Company, Inc

12 James M.R and Cohen J.B (1977) Study of the Precision of X-Ray Stress Analysis, Adv X-ray Anal., 20, pp 291-307

13 Hauk V.M and Macherauch (1984) A Useful Guide for X-ray Stress Evaluation (XSE), Adv X-ray Anal., 27, pp 81-99

14 Dolle H (1979) The Influence of Multiaxial Stress States, Stress Gradients and Elastic Anisotropy on the Evaluation of (Residual) Stresses by X-rays, J Appl

Cryst., 12, pp 489-501

15 Noyan I.C and Cohen J.B. (1984) Determining Stresses in the Presence of Nonlinearities in Interplanar Spacing vs sin^2 , Adv X-ray Anal., 27, pp 129-148

16 Sprauel J.M., Barral M. and Torbaty S (1982) Measurement of Stress Gradients by X-ray Diffraction, Adv X-ray Anal., 26, pp 217-224

17 Toshihiko Sasaki, Makoto Kuramoto and Yusuo Yoshioka (1984) X-ray Multiaxial Stress Analysis Taking Account of Stress Gradients, Adv X-ray Anal. 27, pp 121 -128

18 Krawitz A. D., Brune J. E. and Schmank M. J. (1982) Measurement of Stress in the Interior of Solids with Neutrons, Ref 1, pp 139 - 155

19 Pintschovius L., Jung V., Macherauch E., Schafer and Vohringer O (1982) Determination of Residual Stress Distributions in the Interior of Technical Parts by Means of Neutron Diffraction, Ref 1, pp 467 - 482

20 Barrett C S and Predecki P (1976) Stress Measurement in Polymeric Materials by X-ray Diffraction, Polymer Eng & Sci., 16, pp 602 - 608

21 Barrett C S. and Predecki P. K. (1978) Measuring Triaxial Stresses in Embedded Particles by Diffraction, Adv. X-ray Anal 21, pp 305 - 307

22. Predecki P. and Barrett C. S. (1979) Stress Measurement in Graphite/Epoxy Composites by X-ray Diffraction from Fillers, J. Composite Materials, 13, pp 61 - 71

23 Predecki P and Barrett C. S. (1980) X-ray Stress Measurement in Graphite/Epoxy Composites, Proc. of the DARPA/AFML, Review of Progress in Quantitative NDE, Rockwell International Science Center, AFWAL-TR-80-4078, pp 225 - 227

24 Kittle C. (1971) Introduction to Solid State Physics, 4th ed., John Wiley & Sons, Inc. pp 163

25 Long D A (1977) Raman Spectroscopy, McGraw-Hill

26 Loudon R (1964) The Raman Effect in Crystals, Adv Phys., 13(52), pp 423

27 Anastassakis E., Pinczuk A., Burstein E., Pollak F H and Cardona M (1970) Effect of Static Uniaxial Stress on the Raman Spectrum of Silicon, Solid State Comm., 8, pp 133-138

28 Wigner E P (1959) Group Theory and its Application to the Quantum Mechanics of Atomic Spectra, Academic Press

29 Max Born and Kun Huang (1954) Dynamical Theory of Crystal Lattices, Oxford Press

30. Ganesan S., Maradudin A. A. and Oitmaa J. (1970) A Lattice Theory of Morphic Effects in Crystals of Diamond Structure, Anals. of Phys., pp 556-594

31. Evangelos Anastassakis (1981) Inelastic Light Scattering in the Presence of Uniaxial Stresses, J. Raman Spectroscopy, 10, pp 64-76

32. Weinstein B.A. and Piemarini G.J. (1975) Raman Scattering and Phonon Dispersion in Si and GaP at Very High Pressure, Phy. Rev. B 12(4), pp 1172-1186

33. Cerdeira, F., Buchenauer C. J., Pollak F. H. and Cardona M. (1972) Stress-induced Shifts of First-Order Raman Frequencies of Diamond and Zinc-Blend Type Semiconductors, Phy. Rev. B 5(2), pp 580-593

34. Sergio Rodriguez, Fisher P. and Fernando Barra (1972) Spectroscopic Study of the Symmetries and Deformation Potential Constants of Singly Ionized Zinc in Germanium, Theory, Phy. Rev. B 5(6), pp 2219-2233

35. Harker Y. D., She C.Y. and Edwards D. F. (1969) Stress-Dependent Raman Frequency and Linewidth in α-Quartz, Appl. Phys. Lett. 15(8), pp 272-275

36. Harker Y.D., She C.Y and David F. Edwards (1970) Raman Spectra of α-Quartz Under Uniaxial Stress J. Appl. Phys., 41 (13) pp 5274-5278

37. Tekippe V. J., Ramadas A.K. and Sergio Rodriguez (1973) Piezospectroscopic Study of the Raman Spectrum of α-Quartz, Phy. Rev. B 8(2), pp 706-717

38. Soo H. Shin, Fred H. Pollak and Paul M. Raccah (1975) Effects of Uniaxial Stress on the Raman Frequencies of Ti_2O_3 and Al_2O_3, Light Scattering in Solid, 3rd Conf., Campinas, Brazil, Balkanski M. ed., pp 401-405

39. Mills D.L. and Maradudin A.A. (1970) Theory of the Raman Effect in Metals, Anals. of Phys., 56, pp 504-555

40. Englert Th., Abstreiter G. and Pontcharra J. (1980) Determination of Existing Stress in Silicon Films on Sapphire Substrate Using Raman Spectroscopy, Solid State Electronics, 23, pp 31-33

41. Sai-Halasz G. A., Fang F. F., Sedgwick T. O. and Armin Segmuller (1980) Stress-Relieved Regrowth of Silicon on Sapphire by Laser Annealing, Appl. Phys. Lett., 36 (6) pp 419-422

42. Masayoshi Yamada, Ken-Ichi Yamazaki, Hisakazu Kotani, Kenichi Yamamoto and Kenji Abe (1981) Thermally-Assisted Pulsed-Laser Annealing of SOS, Laser and Electron-Beam Solid Interaction and Material Processing, Gibbons, Hess and Sigmon eds., Elsevier North Holland Inc., pp 503-510

43 Omura Y., Inoue T. and Yoshii T. (1981) Raman Spectra of Si-implanted Silicon on Sapphire, Solid State Comm., 37, pp 583-585

44 Kobayashi Y., Nakamura M. and Suzuki T. (1982) Effect of Heat Treatment on Residual Stress and Electron Hall Mobility of Laser Annealed Silicon-on-Sapphire, Appl. Phys. Lett., 40 (12), pp 1040 - 1042

45 Morhange J. F., Kanellis G. and Balkanski M. (1979) Raman Study of Laser Annealed Silicon, Solid State Comm., 31, pp 805 - 808

46 Nakashima S., Oima S., Mitsuishi A., Nishimura T., Fukumoto T. and Akasaka Y. (1981) Raman Scattering Study of Ion Implanted and C.W. - Laser Annealed Polycrystalline Silicon, Solid State Comm., 40, pp 765 - 768

47 Anna K. Zurek, Private Communication

48 Thurston R. N. and Brugger K. (1964) Third-Order Elastic Constants and the Velocity of Small Amplitude Elastic Waves in Homogeneously Stressed Media, Phy. Rev. 133(6A), pp A1604 - A1610

49 Brugger K. (1964) Thermodynamic Definition of Higher Order Elastic Coefficients, Phy. Rev., 133(6A), pp A1611 - A1612

50 Green R. E. Jr. (1973) Ultrasonic Investigation of Mechanical Properties, Herman H. ed. Treatise on Materials Science and Technology, Vol 3, pp 126 - 144

51 Zimmer J.E. and Cost J.R. (1970) Determination of the Elastic Constants of a Unidirectional Fiber Composite Using Ultrasonic Velocity Measurements, J. Acoust. Soc. Am. 47(3), Pt 2, pp 795 - 803

52 Noronha P.J. and Wert J.J. (1975) An Ultrasonic Technuque for the Measurement of Residual Stress, J. Testing & Evaluation, 3 (2), pp 147 - 152

53 Hsu N.N. (1974) Acoustic Birefringence and the Use of Ultrasonic Waves for Experimental Stress Analysis, Experimental Mechanics, pp 169 - 176

54 Husson D., Bennett S.D. and Kino G.S. (1985) Measurement of Stress with Surface Waves, Material Evaluation, 43, pp 92 - 100

55 James M.R. and Buck O., (1980) Quantitative Nondestructive Measurements of Residual Stresses, CRC Critical Reviews in Solid State Sciences, Rockwell Science Center

56 Barton J.R. and Kusenberger F.N. (1974) Residual Stresses in Gas Turbine Engine Components from Barkhausen Noise Analysis, Trans. ASME, J. Engineering for Power, pp 349 - 357

56 Ruuskanen R. and Kettunen P. (1980) Two Ferromagnetic Methods for the Evaluation of Fatigue Limit in Polycrystalline Iron, NDT International, pp105- 106

57 Cullity B.D (1972) Introduction to the Magnetic Materials, Addison- Wesley Pub. Co., pp 264- 266

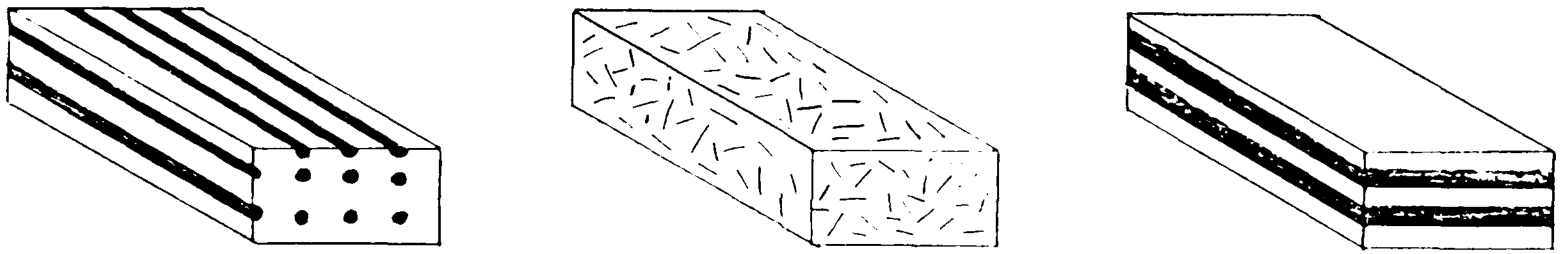

(a)

(b)

(c)

Fig. 1 Schematic illustration of various composite structure
(a) unidirectional fiber (b) random fiber
(c) laminate

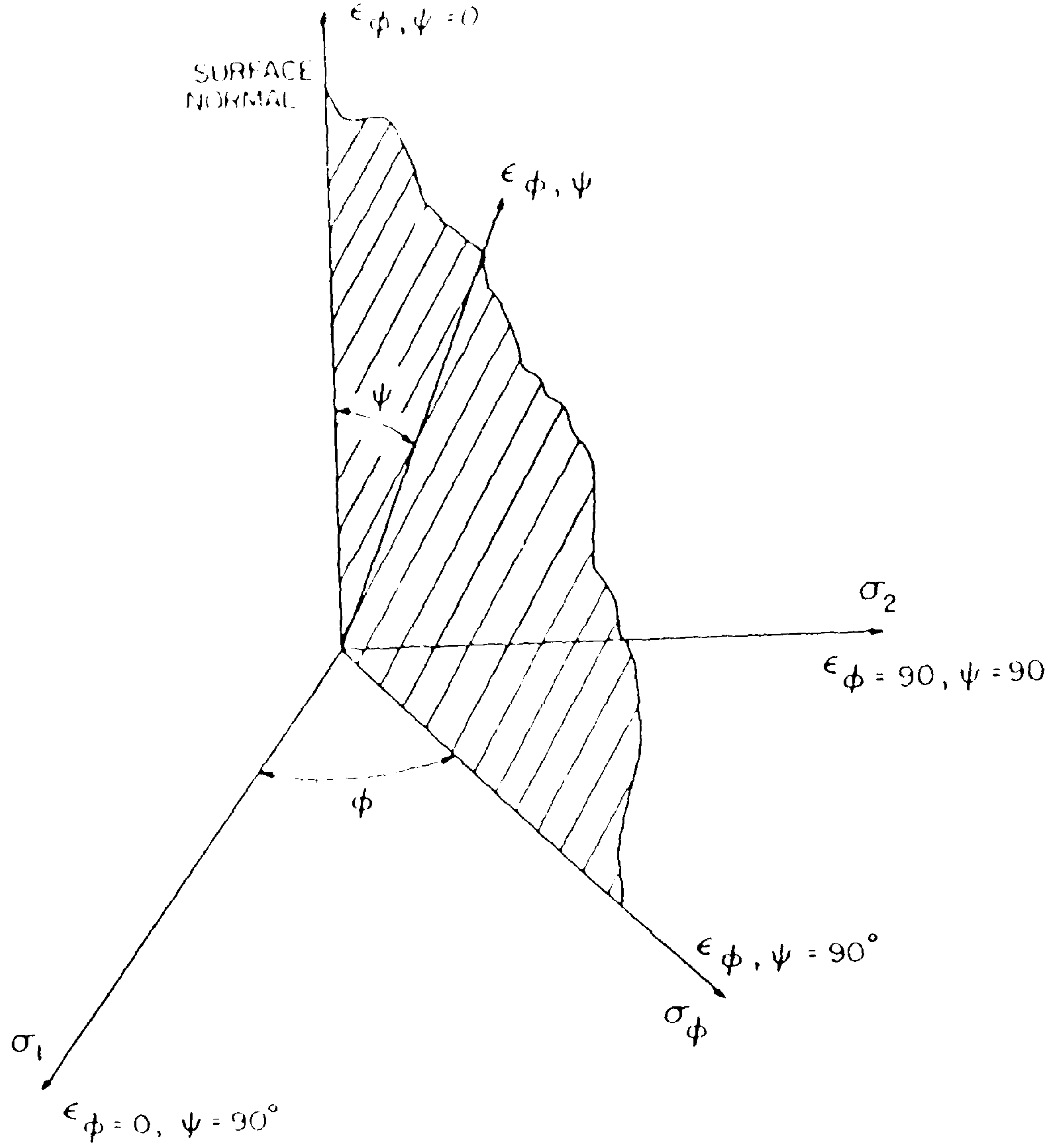
$\epsilon_{\phi}, \psi = 0$
SURFACE NORMAL
ϵ_{ϕ}, ψ
ψ
σ_2
$\epsilon_{\phi} = 90, \psi = 90$
ϕ
$\epsilon_{\phi}, \psi = 90°$
σ_{ϕ}
σ_1
$\epsilon_{\phi} = 0, \psi = 90°$

Fig. 2 Definition of ψ and ϕ and orientation of the stresses (or strains)

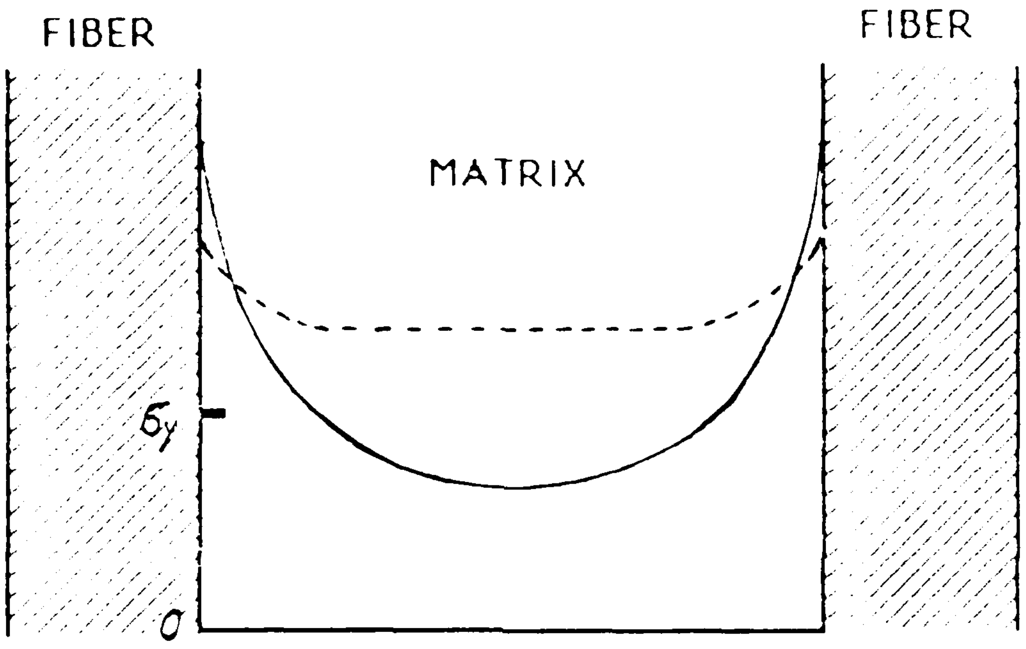
FIBER
FIBER
MATRIX
σ_y
0

Fig. 3 A simple model to show the residual stress distribution. The term σ_y is the yield strength of the matrix.

APPENDIX H

RAMAN MICROPROBE MEASUREMENTS OF RESIDUAL STRAINS AT THE INTERFACES

Y. M. Cheong and H. L. Marcus
Center for the Materials Science and Engineering
The University of Texas at Austin
Austin, Tx, 78712

F. Adar
Instrument S. A. Metuchen, NJ, 08840

ABSTRACT

Raman spectroscopy offers a method of determining residual stresses in Raman active materials. This is reviewed in this paper. In addition it can serve as a method to monitor residual stresses in thin film-substrate composites. Measurements of such stresses by the Raman microprobe have been performed on a Si film on quartz and Al film on quartz. For the quartz, peak shift of one of the Raman active vibration due to applied stress was calibrated using strain gauges and four-point bending method The [illegible]

AD-A186 441 INTERFACE CHARACTERISTICS AND THE MECHANICAL PROPERTIES 2/2
OF METAL MATRIX C..(U) TEXAS UNIV AT AUSTIN CENTER FOR
MATERIALS SCIENCE AND ENGINEE.. H L MARCUS ET AL.
UNCLASSIFIED 28 SEP 87 UTCMSE-87-3 N00014-84-K-0687 F/G 11/4 NL

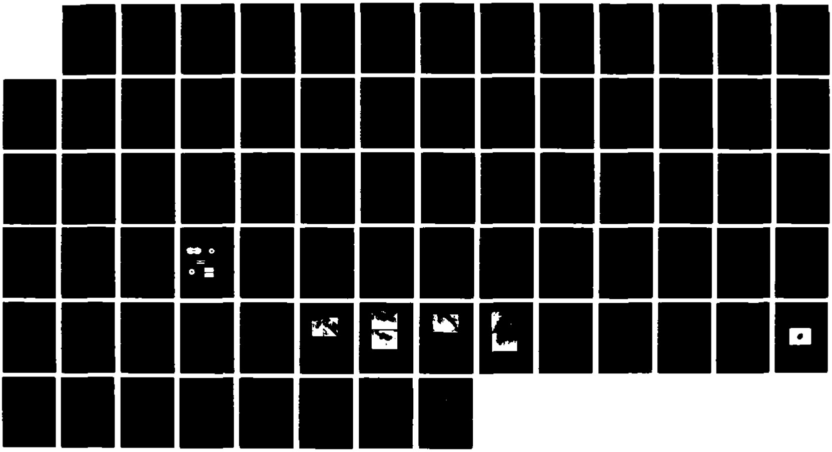

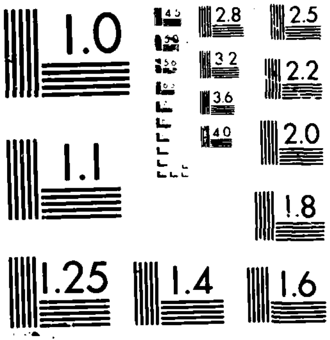
1.0
2.8
2.5
3.2
2.2
3.6
2.0
4.0
1.1
1.8
1.25
1.4
1.6

residual strains at the Si/quartz interfaces using the Raman microprobe were compared to expected residual strains by a model, involving exponential gradient in the substrate and no gradient in the film. The model shows that a small volume of substrate near the interface about 2 times the film thickness was affected by the thermal mismatch of the two regions.

1. INTRODUCTION

When a film is deposited to a substrate residual stresses are developed at the interfaces by various reasons [1]. They are due to 1) the difference of the coefficient of thermal expansion (CTE) of a film and a substrate, 2) lattice mismatch, 3) variation of the interatomic spacing with the crystal size, 4) recrystalization and grain growth, 5) microscopic voids and special arrangement of dislocations, and 6) phase transformations [2]. The fundamental origin of all the stresses are the changes of volume or atomic rearrangement in the film during the process [3].

Even though some of the origins can be understood at least qualitatively the understanding of the origin of stress during deposition and annealing is still unsatisfactory. In many of the experimental approaches that are in use to obtain residual stresses, the detailed understanding of the relationships between the measurable parameters and the stress state are not sufficiently developed to distinguish the details of the stress states. Actually no experimental technique measures stresses directly. Any physical or mechanical properties which are modified by residual stresses can be used for this purposes [4].

For several decades the most common methods for measuring the stresses in a thin film are basically measuring the degree of physical bent of substrates. However, using this technique it is very difficult to compare other results of different authors since the large number of variables are influenced to the process.

X-ray diffraction(XRD), the most advanced approach to obtain residual stress, measures lattice strains relative to a standard.

From the slope of d vs. $\sin^2\psi$ where d is a measured lattice parameter and ψ is a tilting angle, the residual stress can be calculated [5]. Since conventional x-rays can penetrate up to 10 - 50 µm measured residual stresses are merely volume average values. Neutron diffraction with the same principle as the XRD can be used for certain materials with a much deeper penetration depth[6,7].

Raman spectroscopy using monochromatic radiation (laser) can be useful for the measurement of residual stress for the materials having Raman active modes. In the theoretical viewpoint, Raman frequency shifts are linear to the stresses for a certain range of stress[8]. The relation between the stress and Raman band shift can be determined from the information of the deformation potential calculated from the Raman band shift measurements under a given uniaxial stress or a hydrostatic stress. A great deal of literatures on the deformation potentials and stress induced Raman band shifts are available for the single crystal, Si[8-10], Ge[8,11,12], diamond[8], quartz[13-15], and sapphire[16]. Because a laser can be focused at a small region of 1 µm Raman technique can be used effectively for the measurement of residual stresses of a small region near the interfaces of the Raman active materials. The penetration depths of a band of argon ion laser (488 nm) to Si are about 100 nm - 1 µm depending on the crystallinity of Si [17]. Since a quartz is transparent to the light laser can be focused at a small region of Si/quartz interface by illuminating from the quartz subsrate side. Residual stress state of both film and substrate at the interface as well as top surface of Si film can be measured by Raman microprobe technique. The measured residual strains were compared to expected residual strains by a model, involving exponential gradient in the substrate and no gradient in the film (Fig. 1) [18].

2. Approaches to Measure the Residual Stresses at Interfaces

a) Experimental method

Z-cut quartz plates (0.5" long (X-axis) x 0.5" wide (Y-axis) x

0.035" thick (Z-axis), optically polished on both sides) were used for the substrate. Since Z - cut quartz plates were used as substrate, $Z(XX)\bar{Z}$ and $Z(XY)\bar{Z}$ geometry can be used for the measurement of Raman peak shifts in the substrate. The stress-dependent shift in quartz was calibrated by using a four-point bending method by attaching a set of strain gauges on the surface for monitoring the strain (Fig. 2)[19].

Si films of 150 nm thick were produced on the quartz plate by electron beam deposition. The laser beam was polarized parallel to the X - axis of quartz plates. Because the quartz substrate is single crystal and optically transparent, the laser beam can be focused at the interface through the substrate. The Raman peak shift for the measured quartz band at 128 cm^{-1} and that of the Si band at 520 cm^{-1} were measured in the vicinity of the interface. The Raman peak shift from the Si film surface and the quartz substrate surface were also measured for comparison to the measurements at the interface.

An Ar ion laser beam (wavelength = 514.532 nm) was polarized parallel to the X - axis of the quartz plate. Axial spatial resolution (depth of field) of the microprobe can be controlled by an aperture placed at an intermediate image plane between the Raman microprobe and the monochromator entrance slit [20,21]. Under such optical conditions, scattered Raman intensity outside the laser focal volume can be limited by the intermediate aperture. Using Dhamelincount's calculation [20] axial spatial resolution around the interface was expected to be approximately 5 - 10 μm. By monitoring the laser image on the ground glass screen the laser beam can be focused down to 1 μm in diameter.

In addition, residual interfacial stresses were measured in Al film on quartz. Al overlayers of 200 - 1500 nm thick were deposited using the thermal evaporation technique. Since Al has no Raman active mode, Raman spectra from the quartz-side interfaces(128 cm^{-1}) were acquired through the quartz substrates(Fig.3) [19].

b). Results and Discussion

The phonon frequencies decrease linearly as applied tensile stress increase. For the measurement of the residual strain in quartz, a 1 cm^{-1} shift of the 128 cm^{-1} phonon to lower frequency was taken to be equivalent to a strain of 0.4 % or stress of 347 MPa [19]. Because the thickness of the quartz substrate is sufficiently great compared to the Si film, the effect of the thermal mismatch at the interface would be negligible beyond some depth (i.e. extinction thickness). The outer surface of quartz also would not experience the thermal mismatch of the Si film. The measured phonon frequency at the quartz surface used as a standard.

The Raman frequency shift of stressed Si can be estimated by solving the dynamical equations of the cubic lattice perturbed by strains [22-26]. According to Englert's annalysis [24] which assumes only isotropic planar stress ($\sigma_{xx}=\sigma_{yy}=\sigma$, $\sigma_{xy}=\sigma_{yz}=\sigma_{zx}=\sigma_{zz}=0$), the strain ε is related to the frequency shift of the optical phonon modes by the following equation.

$$\varepsilon_{1,2} = -1.38 \times 10^{-3} \, \Delta w_{1,2} \ \mathrm{cm}^{-1}$$

$$\varepsilon_3 = -1.92 \times 10^{-3} \ \Delta w_3 \quad cm^{-1}$$

Here Δw_i is the difference between the measured Raman peak shift of stressed and unstressed Si. The average value was used to calculate the residual stress levels from the measured Raman orientation is expected by XRD results.

Both the microcrystallinity and the stress could produce shifts to lower frequency of Si phonon. In amorphous Si the Raman band is broad and centered at approximately 480 cm^{-1} whereas the band in stress free single crystal appeares at 520.6 cm^{-1}[27,28]. Raman band of Si of crystalline size greater than 150 Å appears around 520.6 cm^{-1} which is about the same as that from the stress free single crystal [28,29]. Crystalline size of approximately 250 Å for the specimen annealed at 900°C, 150 Å for the specimen annealed at 800°C, and 120 Å for the specimen annealed at 700°C were calculated without considering instrumental line broadening by the Sherrer fomula [30]. The effect of the crystallite size on the Raman band position will be negligible. Under these conditions, the shift of the Raman frequency can be used to calculate the residual strains in these specimens. Residual strains were calculated based on $\Delta w = w - w_0$ by setting $w_0 = 520.6\ \text{cm}^{-1}$ Residual strains in the as-deposited specimen and the specimen annealed at 600 °C could not be calculated due to fine size of microcrystallite as indicated by the each of any XRD Si peak. The 500 cm^{-1} implies a crystallite size of less than 30 Å [28].

Relatively high compressive residual strains in the Si film and corresponding tensile residual strains in the quartz substrate at the interface were measured from the specimen annealed at 700 °C and 800 °C (Table 1) compared to the model calculation (Table 2) [18]. These facts may be explained by other sources of residual strain generated at the interface during the crystallization processes in addition to the thermal residual strain term. The difference of lattice spacing of a quartz substrate and Si film during epitaxial growth could result in compressive residual strain in Si film, which is common in the case of Si on sapphire [31]. If we assume that other terms contributing to residual strains may be present,(for example residual strain due to recrystallization and grain growth, residual strain due to lattice mismatch during epitaxial growth), the measured results would be different from the model calculation where only a thermal term is assumed. Since any source of residual strain would contribute to the model to both sides of interface in the model [18], the ratio of measured residual strains in the Si film to those in the quartz substrate would be the same whatever the origins of residual strains that are considered at the interface. By considering the ratio of residual strains in the Si film to the quartz substrate, the ratio of the measured residual strains (Table 1) are relatively well matched to the ratio from the model calculation with the characteristic thickness in the substrate of 1 -2 times the film thickness when the probe thickness (x) in the model was assumed 10 µm , which is a reasonable value from the references 20 (Table 2). In other words, it can be shown that most of the residual strains in the substrate generated by the incompatibility at the interfaces are concentrated in the region of 1 - 2 times the magnitude of the film thickness.

Lower phonon frequencies of the quartz with the Al overlayer to the standard was observed. This means a tensile residual stress is present at the quartz-side of the interface and correspondingly a compressive stress must be present at the aluminum/aluminum oxide side of the interfaces. Annealing of the specimen at 300°C for 30 min. increase the tensile stress in the quartz-side interface.

SUMMARY

The residual stresses at the interfaces of Si on quartz and Al on quartz were measured by Raman microprobe technique. Compressive residual stresses at the Si-side interfaces and tensile residual stresses at the quartz-side interfaces were observed after annealing the specimen. The measurements are compared to the model of a laminate composite with an exponential stress gradient in the substrate and no gradient in the film. A small volume of substrate near the interface about 2 times the film thickness was affected by the thermal mismatch of the two regions. Tensile residual stresses at the quartz-side of the interfaces from Al overlayer on quartz specimens were observed.

Acknowledgement

This work was supported by Texas Advanced Technology Research Programs and DARPA/ONR Contract No. N00014-84-K-0687 at the University of Texas. We would like to thank B. Perrulli (Instrument S. A.) for the arranging of the experimental assistence in making the Raman measurements.

References

1. C. F. Powell, et. al., "VApor Deposition", Chap. 7, John-Wiley, (1966).
2. W. Buckel, J. Vac. Sci. & Tech. 6, (4), pp 606, (1969)
3. R. W. Hoffman, Thin Solid Films, 89, pp 155, (1982).
4. Y. M. Cheong and H. L. Marcus, "Advances in Surface treatments Vol. IV - Residual Stresses", A. Niku-Lari ed., pp 115, Pergamon Press, (1986).
5. M. E. Hilley, et. al. eds., "Residual Stress Measurements by X-ray Diffraction", SAE Information Report, J784(a), (1971).
6. A. D. Krawitz, et. al., "Residual Stress and Stress Relaxation", E. Kula and V. Weiss eds. pp 139, Plenum Press, (1982)
7. L. Pintschovius, et. al., Ref. 6, pp 467.
8. E. Anastassakis, J. Raman Spectroscopy, 10, pp 64, (1981)
9. E. Anastassakis, et. al., Solid State Comm., 8, pp 133, (1970).

10. B. A. Weinstein and G. J. Piemarini, Phy. Rev. B 12, (4), pp 1172, (1975).

11. F. Cedeira, et. al., Phys. Rev. B 5, (2), pp 580, (1972).

12. S. Rodriguez, et. al., Phy. Rev. B 5, (6), pp 2219, (1972).

13. Y. D. Harker, et. al., Appl. Phys. Lett., 15, (8), pp 272, (1969).

14. Y. D. Harker, et. al., J. Appl. Phys., 41, (13), pp 5274, (1970).

15. V. J. Tekippe, et. al., Phys. Rev., B 8, (2), pp 706, (1973)

16. S. H. Shin, et. al., "Light Scattering in Solid", 3rd Int. Conf., Campinas, Brazil, M. Balkanski, Ed., pp 401, (1975).

17. J. F. Morhange, et. al., Solid State Comm., 31, pp 805 (1979).

18. Y. M. Cheong, et. al., J. Materials Research (1987), to be published.

19. Y. M. Cheong, et. al., "interface in Metal Matrix Composites", A. K. Dhingra and S. G. Fishman eds., (Proc. AIME-TMS Conf., New Orleans, The Metallurgical Soc.) pp 147, (1986).

20. P. Dhamelincount, Ph.D Thesis, Univ. of Lillie, (1979).

21. F. Adar and D. R. Clarke, Microbeam Anals., San Fransisco Press Inc., pp.307, (1982).

22. S. Ganasan, et. al., Anals. Phys. (56), pp 556, (1971).

23. V. Lemos et.al., Phys. Rev. B. (16) 12, pp. 5560, (1977).

24. Th. Englert and G. Abstreiter, Solid State Elect., 23, pp. 31, (1981).

25. S. Venugopalan and A. K. Ramdas, Phys. Rev. B (8) 2, pp. 717, (1973).

26. E. Anastassakis et.al., Solid State Comm., 8, pp.133, (1970).

27. F. Adar, et. al.,Appl. Phys. Lett., 47, pp 479, (1985)

28. Z. Iqbal and S. Veprek, J. Phys. C, 15, pp. 377, (1982).

29. Z. Iqbal et. al., Solid State Comm., 37, pp. 993, (1981).

30. H. P. Klug and L. E. Alexander, "X-ray Diffraction Procedures", Chapter 9, John-Wiley, (1954).

31. There are many literatures on the stress in Si on sapphire. For example, ref. 24, Y. Ohmura et.al., Solid State Comm., 37, pp.583 (1981), M.S. Abrahams et.al., Appl. Phys. Lett., 28 (5), pp.275 (1976), G. A. Sai-Halasz et.al., Appl. Phys. Lettt., 36 (6), pp.419 (1980), Y. Kobayashi et. al., Japan J. Appl. Phys., 20 (4), pp.L249 (1981), S. R. J. Brueck et.al., Appl. Phys. Lett., 40 (10), pp.895 (1982).

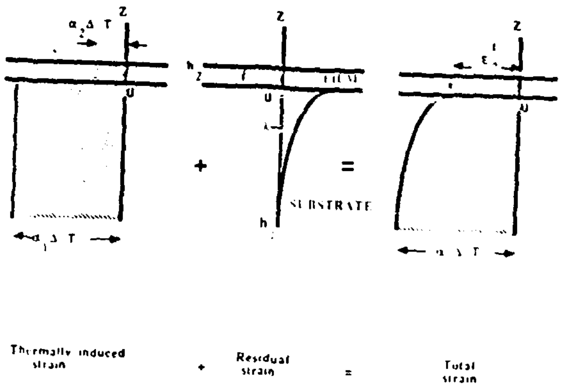
$\alpha_2 \Delta T$
Z
U
$\alpha_1 \Delta T$
+
h
Z
Z
FILM
U
λ
SUBSTRATE
h
=
Z
ε_x^t
U
$\alpha \Delta T$
Thermally induced strain
+
Residual strain
=
Total strain

Fig 1 Schematic drawing shows how the differences of the thermal contractions result in the residual strain distributions in the film and substrate.

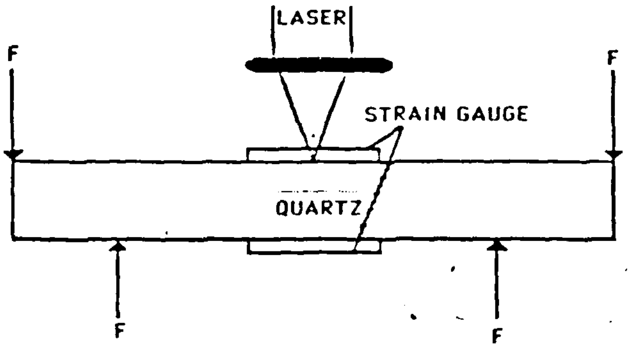
LASER
F
F
STRAIN GAUGE
QUARTZ
F
F

Figure 2 - Schematic drawing shows the four-point bending method and attached strain gauges (half bridge formation).

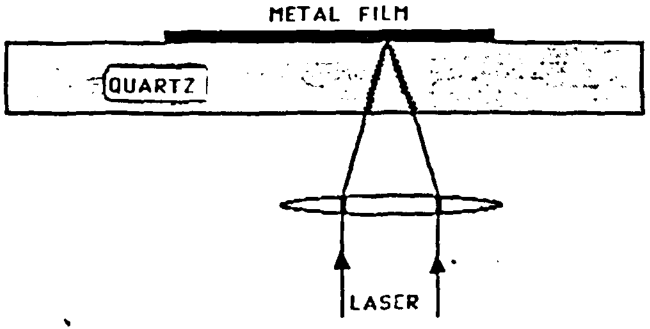
METAL FILM
QUARTZ
LASER

Figure 3 - Experimental geometry for the Raman line shift for the measurement of residual stress on and near the interface between the quartz and metal film.

Table 1 Measured residual strains at the top surfaces of Si film and Si/quartz interfaces by Raman microprobe

Annealing Temp.		$\Delta\omega$ (cm^{-1})	ε (%)	Ratio of $\varepsilon_{Si} : \varepsilon_q$
	S_{Si}	3.7	-0.61	
700°C	I_{Si}	7.8	-1.29	-0.91 : 0.09
	I_q	0.31	0.12	
	S_{Si}	3.6	-0.59	
800°C	I_{Si}	7.6	-1.25	-0.93 : 0.07
	I_q	0.22	0.09	
	S_{Si}	0.2	-0.03	
900°C	I_{Si}	2.9	-0.48	-0.87 : 0.13
	I_q	0.18	0.07	

$\Delta\omega = \omega - \omega_0$ and $\omega_0 = 520.5\ cm^{-1}$

ε_{Si} : Residual strain at the Si-side interfaces

ε_q : Residual strain at the quartz-side interfaces

S_{Si} : Measured at the Si surface for Si

I_{Si} : Measured at the Si/quartz interface for Si

I_q : Measured at the Si/quartz interface for quartz and difference of phonon frequencies between outer surface and interface of quartz.

Table 7. Theoretically predicted residual strains at the Si-side and quartz-side of the interface.

		700° C		800°C		900°C		ratio of
x	λ/h_2	ε_{Si}	ε_q	ε_{Si}	ε_q	ε_{Si}	ε_q	$\varepsilon_{Si} : \varepsilon_q$
	1	-0.43	0.07	-0.40	0.06	-0.38	0.05	-0.87:0.13
10	2	-0.62	0.05	-0.59	0.02	-0.56	0.04	-0.93:0.07
	5	-0.83	0.02	-078	0.02	-0.74	0.02	-0.97:0.03

ε_{Si} : residual strain at the Si-side interface.
ε_q : residual strain at the quartz-side interface.
x : probe thickness (=10 μm).
λ : characteristic thickness(μm).
h_2 : film thickness (= 0.15 μm)
The unit of strains ε_{Si}, and ε_q is %.

APPENDIX I

A THEORETICAL INVESTIGATION OF ACCELERATED AGING IN METAL-MATRIX COMPOSITES

I. Dutta and D.L. Bourell
Center for Materials Science & Engineering
The University of Texas at Austin
Austin, Texas 78712

D. Latimer
Mechanical Repair and Engineering
Laporte, Texas 77571

Abstract

Accelerated aging of precipitation hardening alloys reinforced with particulates or fibers has often been attributed to an increase in dislocation density in the immediate vicinity of the reinforcement. The plastic zone is generated during cooling from the solutionizing temperature due to a mismatch in thermal expansion coefficients of the matrix and the reinforcement. In this work, continuum mechanics and finite element approaches were used to develop models to calculate the plastic strain and the expended plastic work in the matrix in terms of the solutionizing temperature, matrix yield strength and elastic constants, and the reinforcement volume fraction. The information obtained was then used to relate the degree of accelerated aging with the state of plastic strain of the matrix. It was assumed that the plastic zones from adjacent reinforcements are non-interacting and that the reinforcement is incompressible. Aging curves were generated for a monolithic 6061 Al alloy and fiber composites with 10v/o and 30v/o SiC. It was found that composites with a higher volume fraction of SiC age faster. Aging data generated for the monolithic alloy strained plastically after quenching were compared to those for the composites to determine the reliability of the model in determining the degree of accelerated aging, based on materials parameters and reinforcement morphology.

I. INTRODUCTION

One feature common to many precipitation hardening metal-matrix composites (MMC) is an accelerated aging after solutionizing and quenching, relative to composite-free material. This is shown in Figure 1 for 6061P/M aluminum containing 23 volume percent of B_4C [average particle size, 5µm, ref. 1]. The presence of dispersoids decreases the time to peak hardness by approximately one order of magnitude. This behavior has been attributed to strain-enhanced aging. This mechanism of accelerated aging is common in aluminum alloys evidenced by the aging characteristics of metals given the -T3 or -T8 temper (cold work after solution heat treatment). In MMC, the strain is proposed to arise from a difference in thermal expansion coefficients of the matrix and reinforcement. On quenching from the solutionizing temperature, the matrix metal is plastically deformed as it shrinks around the reinforcement [1-7]. This plastic deformation increases the driving force of discontinuous precipitation, thereby accelerating the precipitation rate by dislocation-enhanced diffusion of the second phase [8-11]. Second phase nucleation is facilitated by dislocation - particle interaction, which reduces the overall strain energy of the system [12]. Dislocations can also act as "collector lines" for solutes, such that excess solute first flows radially from the matrix to the dislocation, followed by rapid diffusion along the defect to the second phase particle, thereby aiding the growth process [13,14]. Weak beam transmission electron microscopy reveals that dislocations can serve as potent catalysts for the precipitation process in the solid state [15]. High voltage electron microscopy of Al-SiC interfaces reveals a high density of dislocations, which are frequently decorated with fine precipitates [4].

In this investigation, the effective plastic strain and the plastic work done by the reinforcing phase due to thermal expansion coefficient mismatch during cooling from the solutionizing temperature have been calculated in terms of the cooling range, matrix yield strength / elastic constants and the reinforcement volume fraction. These values have been calculated based on noncontacting plastic zones from adjacent reinforcements for spherical dispersoids, continuous filaments in plane strain, continuous fibers in non-plane strain and chopped fibers. The information obtained has been used to relate the degree of accelerated aging with the properties of the matrix/reinforcement and the reinforcement morphology. It has been assumed that the reinforcement is incompressible and the matrix is elastic-ideally plastic.

The correlation of the dislocation density with the plastic work done on the matrix due to deformation is shown in the Appendix.

II. THERMAL EXPANSION INDUCED STRAIN

Plastic strain imposed on a matrix by a spherical dispersoid or cylindrical fiber during cooling from elevated temperature requires change in reinforcement radius relative to the matrix. The thermal history is shown schematically in Figure 2, which includes the nomenclature used for dispersoid or fiber radius. A conceptual thermal history is postulated which makes use of the fact that at elevated temperature T_s, restoration processes eliminate dislocations formed during heating by thermal expansion difference between matrix and reinforcement. Suppose that a spherical dispersoid or cylindrical fiber of room temperature radius a_D is heated to a temperature T_s. Its radius changes to a_T due to thermal expansion. The reinforcement is then placed in a cavity of radius a_T in a matrix material, thereby producing no plastic strain. This requires the room temperature matrix cavity radius to be a_M, less than a_T. Upon cooling to room temperature, the matrix tries to contract more than the reinforcement because of its higher thermal expansion coefficient. This induces strain in the matrix and if the difference in the thermal expansion coefficients is large enough, the matrix becomes plastically deformed with a plastic zone radius c. The reinforcement reaches a radius, a, which may range between a_M (incompressible matrix) and a_D (incompressible reinforcement). For common MMC, the final radius is very nearly equal to a_D. It is henceforth assumed that the reinforcement is incompressible.

The matrix accommodates a change in radius from a_M to a. The relative expansion of the matrix cavity a/a_M may be written in terms of the linear coefficient of thermal expansion of the matrix α_M and the dispersoid or fiber α_D appropriate for the range of temperature $\Delta T = T_s - T_{RT}$:

$$a_T = (1 + \alpha_D \Delta T)a_D = (1 + \alpha_M \Delta T)a_M$$

Solving for a/a_M,

$$a/a_M \cong a_D/a_M = (1 + \alpha_M \Delta T)/(1 + \alpha_D \Delta T) \cong 1 + (\alpha_M - \alpha_D)\Delta T \qquad (1)$$

The effects of this displacement on the matrix will be considered for the case of spherical dispersoids as well as continuous and discontinuous cylindrical fibers in the following sections.

In all cases, cooling from T_s to room temperature is assumed to be sufficiently rapid that the extent of matrix restoration is negligibly small. The extent of relative expansion a/a_M is seen to increase with increasing temperature difference and decreasing reinforcement expansion coefficient. While a/a_M ranges between zero and about 1.015, a reasonable range covering most alloy systems and heat treatments is 1.005 to 1.010. For SiC reinforced 6061 Al matrix composite, a/a_m is 1.010.

III. REINFORCEMENT MORPHOLOGY & SOLUTION APPROACH

Four different models were studied. The geometry and method of solution vary for each. They are:

1. Spherical dispersoids embedded in the matrix
2. Infinitely long cylindrical fibers with the matrix in plane strain
3. Infinitely long cylindrical fibers with the matrix in non-plane strain (Continuous Fibers)
4. Finite cylindrical fibers embedded in the matrix (Discontinuous Fibers).

In each case, a semi-infinite matrix was assumed and a cavity having the shape of the dispersoid particle or the fiber was assumed to expand under internal pressure generated due to differential thermal contraction of the matrix and the reinforcing phase. In late stages of each analysis, reinforcement volume fraction is incorporated by introducing a periodic array of isolated reinforcement particles. After each model is introduced, the results will be presented.

1. Spherical Dispersoids :

The plastic zone around an expanding spherical cavity in an infinite medium is well documented. According to the analysis by Hill [16], a plastic zone of radius c forms in a matrix as a cavity expands from a_M to a. The relationship between these parameters is given by

$$(a/a_M)^3 = 1 + \{3(1-v)\sigma_{ys}(c/a_M) - 2(1-2v)\sigma_{ys}[3\ln(c/a_M)+1]\}/E \qquad (2)$$

where the elastic modulus E, Poisson's ratio v and yield stress σ_{ys} are matrix values. The effective plastic strain ε^P_e in a plastic zone of radius c around the dispersoid is a function of radial distance r only :

$$\varepsilon^P_e = 2\sigma_{ys}(1-v)[(c/r)^3-1]/E \qquad (3)$$

Assuming a periodic cubic array of dispersoids of spacing S in the matrix, giving rise to a reinforcement volume fraction V_c, the plastic work expended per unit composite mass is given by:

$$E_w{}^m = E_w/\rho S^3 = 6\sigma_{ys}(1-\nu)\{(c/a)^3[\ln(c/a)-1/3]V_c/\rho E \qquad (4)$$

where ρ is the density of the matrix and E_w is the plastic work expended by a single spherical particle ($E_w = \iiint \sigma_{ys}\varepsilon_e{}^p \, dV$).

The above analysis requires that plastic zones between two adjacent composite particles be noncontacting. For a cubic array of spherical particles of diameter 2a, spaced a distance S apart, it has been shown [17] that the maximum volume fraction of composite V_{cmax} for which plastic zones are noncontacting is estimated to be

$$V_{cmax} = \{4\pi a^3/3\}/S^3 = (\pi/6)\,(a/c)^3$$

for the noncontacting constraint $S \geq 2c$.

When the volume fraction of composite exceeds this value, plastic zones interact. Assuming that the plasticity analysis is not severely altered by this plastic zone interaction, the deformation volume takes the shape of a sphere truncated by six, orthogonal one-base segments. This condition is valid so long as the undeformed matrix between plastic zones is continuous ($S \geq c\sqrt{2}$) and the composite particles themselves do not contact each other ($S \geq 2\sqrt{a}$). The mean strain term $\bar{\varepsilon}_e{}^p$ ($\bar{\varepsilon}_e{}^p = \iiint \varepsilon_e{}^p \, dV$) is not considered to change significantly as plastic zones from adjacent dispersoids interact, although the expended plastic work per unit composite mass $E_w{}^m$ is greater.

2. Cylindrical Fibers with Matrix in Plane Strain

The plastic zone around an expanding cylindrical cavity in an infinite matrix medium is somewhat complicated by the fact that the third principal stress (σ_z) is not related to the other two by symmetry considerations, as is true for the spherical case (i.e., $\sigma_\theta=\sigma_\phi$). The cylindrical solution is therefore sought using the numerical approach outlined by Hill [16], with the additional simplifying assumption of plane strain ($d\varepsilon_z=0$). The result of this analysis is a one-to-one relationship between a and c (or a/a_m and c/a), similar to equation 2 for the case of spherical particles. Also, the plastic strain field may be calculated by the appropriate numerical integration along the particle path line [16]. The total effective strain may be obtained by summing the incremental value over the expansion of the cavity from the onset of yielding to the final value and subsequently subtracting away the elastic component :

$$\varepsilon_e{}^P = \varepsilon_e{}^T - \varepsilon_e{}^E = (2/\sqrt{3})\,\Sigma|\partial\varepsilon_r{}^T| - (2/\sqrt{3})|\,\sigma_r/E - \nu/E(\sigma_\theta + \sigma_z)| \qquad (5)$$

Finally, the mean effective plastic strain $\overline{\varepsilon}{}^P{}_e$ at any extension of the plastic zone is calculated by a cylindrical averaging of strain over the plastically deformed volume.

The work associated with plastic deformation E_w is obtained in a manner similar to the method followed for the spherical dispersoid :

$$E_w = \iiint \sigma_{ys}\ \varepsilon_e{}^P dV = \sigma_{ys}\ \overline{\varepsilon}_e{}^P \pi[(c/a)^2-1]za^2$$

where z is an arbitrary length dimension parallel to the axis of the fiber. This plastic work term can be written in terms of the volume fraction of the reinforcement V_c if it is assumed that the fibers are parallel and spaced on a square array separated by a distance S :

$$E_w{}^m = E_w/S^2z = \sigma_{ys}\ \overline{\varepsilon}_e{}^P V_c[(c/a)^2-1]/\rho \qquad (6)$$

These equations are valid so long as plastic zones do not interact. As for the spherical case, this corresponds to $2c \leq S$,

$$V_{cmax} = \pi(a/S)^2 = \pi(a/2c)^2 = \pi(a/c)^2/4 \qquad \text{(noninteracting plastic zones)} \qquad (7)$$

Beyond this volume fraction, the plastic zone can be treated the same way as the spherical plastic zone. The interacting plastic zones from the four nearest fibers act to truncate the circular plastic zone.

3. Infinitely long Cylindrical Fibers with Matrix in Non-Plane Strain

Most continuum mechanics approaches available in the literature either assume plane strain conditions [18-20] or assume that the axial strain does not vary in the radial direction [16,21]. While the second assumption is fairly accurate when the fibers are infinite, it is not valid when the fibers have a finite length. However, finite element analysis allows modelling of the composite system without any such assumption. Hence, a finite element approach was sought for both fiber morphologies (infinite and finite) when the matrix is in non-plane strain.

A finite element method (FEM) was used to analyze the stress-strain conditions in a two phase material system of hard particles embedded in a soft matrix [22-24]. In the following analysis, the NASA TRANSPORT CODE (NASTRAN) [25] was used.

The expansion of a thick walled, infinitely long cylinder was modelled as follows. First, it was assumed that since the cylindrical fiber is infinite in length, the stress and strain distributions do not vary along the cylinder axis if analyzed sufficiently far from the ends. Hence, only a thin layer of the matrix around the fiber was analyzed. Furthermore, since there is cylindrical symmetry around the fiber, it is sufficient to analyze a wedge shaped element to characterize the entire matrix. This wedge shaped element, shown in Figure 3, was then divided into smaller volume elements (the finite elements). The model requires that adjacent fibers be sufficiently spaced so that the strain field of one is not altered by that of another. It was also assumed that the matrix is elastic-ideally plastic and isotropic.

In the finite element mesh in Figure 3, the points B and B', being at the middle of the fiber (or cavity in the matrix) can move only in the radial direction, while the rest of the nodes can move both in the radial and the axial directions. A forced displacement, equal to the expansion of the cavity due to thermal expansion coefficient mismatch between the matrix and the fiber, is applied to B and B' in the radial direction, and to A and A' in both the radial and the axial directions. The displacement of A and A' in the axial direction is taken to be proportional to the fractional thickness of the matrix layer being analyzed with respect to the fiber (or cavity) radius. This is based on the assumption that the matrix has identical coefficients of expansion in the axial and the radial directions. The rest of the nodes are free to move in the r and z directions independently, although to maintain the cylindrical symmetry, they are constrained not to move in the θ direction. With these constraints, and the assumption of semi-infinite length, the model represents the matrix around one-half of the fiber.

On application of pre-determined incremental displacements at the nodes A, A', B and B', NASTRAN calculated the stress, plastic strain and displacement of each node point, and hence the size of the plastically deformed zone in the matrix. The mean effective plastic strain can once again be determined using the same procedure as before, while the plastic work per unit composite volume fraction is obtained from equation 6.

4. Finite Cylindrical Fibers with the Matrix in Non-plane Strain

The finite element (NASTRAN) approach was once again used to obtain a solution. Two fiber geometries were chosen with aspect ratios of 1 and 3. As before, cylindrical symmetry prompted selection of a slice of the matrix with a wedge shaped cross section . However, the modeled part of the matrix extended from the middle of the fiber to considerably beyond the end, as shown in Figure 4.

As for the infinite non-plane strain solution, predetermined incremental displacements were applied to the node points at the matrix-fiber interface (A to E). The points on the plane AA'ZZ' were constrained by symmetry to move only in the r direction, while points E through M for the same reason moved only in the z direction. All other points moved in r and z directions independently. Movement in the θ direction was forbidden to maintain cylindrical symmetry around the fiber.

The stresses, effective plastic strains and displacements of all the node points were calculated. The total plastic work due to differential contraction around one fiber is therefore approximated as

$$E_w = \sigma_{ys} \Sigma \varepsilon_e{}^p r\Delta\theta\Delta r\Delta z \tag{8}$$

where $r\Delta\theta\Delta r\Delta z$ represents a differential volume of sides $r\Delta\theta$, Δr and Δz, r being the radial distance from the z axis to the centroid of the finite element after yielding. The summation is carried out over all the finite elements around the fiber (or the cavity) which have yielded. If a square array of discontinuous but unidirectional cylindrical fibers in the matrix is assumed, and on average the fibers below start at the same level where the fibers above end (Figure 5), then the composite volume fraction is still given by $V_c = \pi(a/S)^2$. The plastic work per unit mass of the composite is given by

$$E_w{}^m = E_w/(\text{mass of composite}) = E_w/(S^2z)\rho \tag{9}$$

where ρ is the density of the matrix and z is the average length of the fiber. The plastic work per unit composite mass per unit fiber volume fraction may be written as :

$$E_w{}^m/V_c = E_w{}^m/(S^2z)\rho = E_w/(\rho\pi a^2 z) \tag{10}$$

IV. RESULTS AND DISCUSSION OF THE THEORETICAL INVESTIGATION

Figures 6 through 9 show the results of the theoretical analysis. A non-strain-hardening aluminum matrix with an elastic modulus of 68,950 MPa was assumed. The composite with spherical reinforcements was analyzed for two matrix yield strengths, viz., 100 and 200 MPa.

Figure 6 is a plot of the elastic-plastic interface relative radius c/a at some point in the expansion versus the relative matrix expansion a/a_M. The plastic zone size is found to increase with increasing relative matrix expansion. Since a/a_M is proportional to the solutionizing temperature and the thermal expansion coefficient mismatch (equation 1), an increase in these factors increases the plastic zone size. Although the plastic zone size for plane strain cylinders is greater than that for spheres, for infinitely long cylinders in non-plane strain (continuous fibers) the plastic zone is smaller. Hence, even if the fibers are very long, the assumption of plane strain does not closely approximate reality. Figure 6 also shows that for discontinuous fibers, the plastic zone size at the ends of the fibers is greater than that at the middle. This end-effect is generated principally because the matrix is constrained more at the end of the fiber than at the middle since the aspect ratio is more than 1. This makes the plastically deformed zone extend considerably beyond the fiber end. Also, the sharp corners in the fiber profile act as stress raisers, leading to more matrix deformation (corner effect). Together, the end and corner effects give rise to a "peanut-shell" shaped plastic zone. For very short fibers (aspect ratio ≤ 1), the end effect is absent, although the corner effect still plays a role in determining the plastic zone shape. This makes the plastic zone sizes at the fiber end and middle almost equal, although the matrix is still plastically deformed beyond the fiber-end. For spherical reinforcements, it is seen that the plastic zone size decreases with increasing matrix yield strength. Also, the matrix material deforms elastically during the early stages of the expansion, the amount of this elastic expansion being indicated by the value of a/a_M at which c/a becomes unity. As expected, the elastic displacement prior to yielding is greater for matrix metals of increasing yield strength.

Figure 7 summarizes the approximate relative plastic zone geometries and sizes for reinforcements of different morphology.

Figure 8 shows the effective plastic strain (ε_e^P) plotted against the radial distance from the center of the reinforcement expressed as a fraction of the plastic zone size (r/c). The effective plastic strain is found to decrease with increasing r/c, and finally vanish at the plastic-elastic zone boundary (r=c). The intensity of plastic deformation at a particular r/c increases with increasing aspect ratio (sphere through infinitely long cylinder). Also, the effective plastic strain at a particular value of r/c is greater along the center plane of the fibers of aspect ratio 3 than at the ends, giving the misleading impression that deformation is more intense at the center of the fiber. In actuality, at any radial distance away from the fiber, the effective plastic strain is greater at the ends than at the middle. The apparent anomaly is due to the fact that in Figure 8, the radial distance r has been normalized against c, which is larger at the fiber end. Whereas increasing matrix yield strength decreases the size of the plastic zone around a spherical dispersoid, it increases the plastic strain throughout. Once again, the plane strain cylindrical fibers do not follow the trend and reflect strain values considerably lower than that expected due to infinitely long cylinders.

Figure 9 is a plot of the ratio E_w^m/V_c as a function of matrix cavity expansion a/a_m. The plastic work increases with increasing relative matrix expansion. It is found that with increasing cylinder aspect ratio, the plastic work decreases for the same relative matrix expansion. This is because the plastic work term is a function of both the strain in the plastic zone and the size of the zone. Although the effective plastic strain for an infinitely long cylinder is greater than for a sphere, the plastic zone size is smaller, resulting in a smaller net plastic work. However, when the aspect ratio of the cylinder is decreased to a finite value at constant a/a_M, E_w^m/V_c is found to increase. This is principally due to large end effects resulting from the greater fiber expansion axially than radially. The corner effect, resulting from greater stress concentration at fiber corners also contributes to a greater E_w^m/V_c. For a constant fiber volume fraction, the longer the fiber, the more plastically deformed are zones at the fiber ends, and hence the greater is E_w^m. Decreasing the aspect ratio will decrease the size of the plastically deformed zone at the fiber-end, thereby resulting in a decrease in E_w^m. This is evident from Figure 9, where decreasing the aspect ratio from 3 to 1 makes E_w^m/V_c taper off slightly. The balance between a bigger plastic zone size and a smaller plastic strain fortuitously makes the plastic work for the plane strain cylinder almost coincident with that for the non-plane strain infinite cylinder, although neither the strains nor the plastic zone sizes are the same in the two cases. Spherical reinforcements yield an E_w^m/V_c value that is intermediate between finite and infinite fibers. For spherical reinforcements, it is seen that the extent of plastic work is greater for stronger matrix metals above a relative matrix expansion (a/a_M) of about 1.005. Below that value, the 100 MPa matrix yields a greater E_w^m/V_c. This is because a weaker matrix yields earlier, but less plastic work is done on it, resulting in lower E_w^m/V_c values at a greater a/a_M.

The preceding discussion elucidates several important points. First, the plastically deformed zone in the matrix for spherical dispersoids is larger than that for continuous fibers. For discontinuous fibers, the size of the plastic zone is bigger at the ends, but smaller at the middle of the fibers. Second, the intensity of deformation in the plastic zone, reflected by the effective plastic strain, increases with increasing aspect ratios. Third, the plastic work is greatly dependent on the end effect, and hence is very sensitive to the aspect ratio. Fourth, the yield strength of the matrix affects the plastic work term and hence accelerated aging, although the dependence changes with the solutionizing temperature and the thermal expansion coefficient mismatch between the matrix and the dispersoid. And finally, based on the information obtained from Figures 6 and 8, it is seen that the assumption of plane strain is not valid, even in a continuous fiber reinforced MMC.

Size Effect of Particulates or Fibers :

One feature of the models used in this study is that the absolute size of the reinforcements does not affect the plastic work term so long as their shape and volume fraction are constant. In other words, two composites, one with smaller reinforcements and the other with larger reinforcements, will be equally effective in producing plastic deformation so long as the aspect ratios and the volume fractions are the same. While a larger diameter leads to a larger plastic zone, the relative plastic zone size (c/a) and the plastic zone geometry remain the same since no assumption of fiber size has been incorporated in any of the models. And since the effective plastic strain ε_e^p is a function of only the relative radial distance (r/a) besides material properties and the cooling range (ΔT), the contribution of ε_e^p to the plastic work (equation 8) will be the same for composites of different sized reinforcements.

For the case of a coarser fiber, the plastic zone size will be proportionately bigger, thereby generating a greater total plastic work. But if the fiber volume fractions (V_c), given by

$V_c = \pi a^2 z/(S^2 z) = v_f/(S^2 z)$ (v_f = volume of a fiber)

are the same in both composites, an increase in v_f will lead to a proportionate increase in the fiber spacing term S^2z. Hence, the plastic work per unit mass of the composite E_w^m (equation 9) will be the same in both composites. The same is true for spherical dispersoids. This is clear from equation 4, which shows that the plastic work per unit composite mass depends only on material properties, the ratio c/a and the dispersoid volume fraction V_c.

One implication of this observation is that when comparing the relative effectiveness of, for instance, spherical dispersoids and fibers of a certain aspect ratio in producing matrix deformation, it does not matter whether the spheres and the fibers have the same individual size, so long as the two composites have the same volume fraction of the reinforcing phase.

V. EXPERIMENTAL SUPPORT OF THE RESULTS

Aging curves were generated for monolithic 6061 aluminum and composites with 10 and 30 volume percent of randomly oriented discontinuous SiC fibers of aspect ratios ranging from 1 to 20 (Figure 10). Increasing the volume fraction of SiC decreases the time to peak hardness. This is reasonable as a higher volume fraction yields a greater plastic work, thereby leading to more accelerated aging.

To demonstrate the applicability of the foregoing models, two conceptual MMCs consisting of 6061 aluminum containing 10 and 30 volume percent of SiC fibers of aspect ratio 3 were analyzed. The plastic work terms, calculated assuming a solutionizing temperature of 530°C, were converted into an equivalent plastic tensile strain ε^p for a matrix density of 2.7 Mg/m^3 and a yield strength of 200 MPa as follows :

$$E_w^m = \sigma_{ys}\,\varepsilon^p/\rho = 74000\,\varepsilon^p \text{ mJ/gm}$$

The Table lists the results of these calculations, together with the input data . It is seen that the equivalent effective plastic strain for the composite with 10 v/o SiC is 0.36%, while for that with 30 v/o SiC is at least 1.07%. These figures were calculated on the basis of our model with non-interacting plastic zones. However, for the 30 v/o SiC composite, in which the plastic zones do interact, the outer peripheries of the plastic zones with lower effective strain overlap with adjacent zones. This raises the plastic work per unit composite volume fraction, and hence the equivalent tensile strain to a value greater than that calculated for non-interacting zones, viz., 1.07%. These equivalent tensile strain values obtained above compare favorably with the order of strains known to accelerate aging in aluminum alloys. Specifically, uniform elongations of one to two percent have been shown to affect the aging characteristics of nondispersoid bearing aluminum [26].

In order to verify the effect of plastic deformation on the rate of aging, three monolithic 6061 aluminum samples (σ_{ys} = 150 MPa, ρ = 2.7Mg/m^3) were solutionized at 530°C, quenched, and subjected to tensile strains of 0.25%, 1.2% and 2% respectively. The samples were then aged at 205°C. As expected, the time to peak hardness decreased with increasing plastic work. This is illustrated by Figure 11 (solid line). Also indicated are data for the two composites, showing the time to peak hardness as a function of the calculated specific plastic work. Based on these results, the models for accelerated aging tend to underestimate the expended plastic work. One cause is that the model assumes parallel, evenly spaced fibers of aspect ratio 3 with non-interacting plastic zones, although in the actual samples these conditions were not satisfied. The increasing anomaly at higher fiber volume fraction is expected since the plastic zones start interacting, leading to a greater degree of plastic work than predicted.

VI. CONCLUSIONS

A method has been presented for modeling deformation zone formation arising from differential thermal contraction in a metal-matrix composite. The problem was considered for a periodic array of spherical or cylindrical reinforcements. In the case of cylindrical fibers, different aspect ratios were treated, and both plane and non-plane strain conditions were analyzed.

In the analysis of the matrix plastic zone around a fiber, the usual simplifying assumptions of plane strain and/or infinitely long fiber do not correctly represent the deformation of the matrix around a finite fiber. When the fiber has a finite aspect ratio, the ends of the fiber have the effect of increasing the plastic deformation of the matrix, thereby leading to a peanut-shell shaped plastic zone. The effective plastic strain was found to increase with increasing particulate aspect ratio, the spheres generating the lowest plastic strains and the infinitely long cylinders generating the highest. However, the plastic work done on the matrix, which is a function of both the plastic strain and the zone size, was found to be the greatest for fibers of long but finite aspect ratio, since the net plastic zone size per unit reinforcement volume fraction is the largest in this case and the strain level is also high (second only to the infinitely long fibers in non-plane strain, which give a very small plastic zone). The large plastic zone arises due to end and corner effects resulting from the corners in the fiber profile and the high matrix constraint at the end of the fiber, respectively, which in turn result in a larger and more intense plastic zone. It was also found that for all composite morphologies, the plastic work expended by the matrix increases with increasing solutionizing temperature and increasing thermal expansion coefficient mismatch.

Hence, it is concluded that the factors that exacerbate accelerated aging are (1) large cooling range, (2) large thermal expansion coefficient mismatch, (3) large reinforcement volume fraction and (4) large but finite aspect ratio fibers. Decreasing the fiber aspect ratio to unity or less reduces the matrix constraint at the fiber-end although the corner effect is still present, thereby decreasing the expended plastic work, and hence accelerated aging.

It is also concluded that the particle or fiber size should not affect the aging rate so long as there is a constant volume fraction of the second phase in the matrix. Hence, while comparing the relative effectiveness of differently shaped particulates in producing matrix deformation, the volumes of the particulates need not be identical.

The role of matrix yield strength is somewhat complicated by elastic effects. Weak matrices yield quickly but accumulate strain at a slower rate than stronger matrices. Therefore, it is not possible to predict a priori whether a change in matrix yield strength will enhance or inhibit accelerated aging. For the aluminum matrix system described here, accelerated aging is enhanced by making the matrix stronger.

ACKNOWLEDGEMENT

The majority of this work was sponsored by DARPA/ONR under contract # N00014-84-K-0687. The authors would like to thank Dr. A.E. Traver, Assistant Professor of Mechanical Engineering at the University of Texas at Austin for his help with the finite element analysis.

REFERENCES

1. T.G. Nieh and R.F. Karlak, Scr. Metall. 18 (1984) 25-28
2. "Progess in Science and Engineering of Composites", Proc. 4th Int. Conf. on Composite Materials, Tokyo, 1982, T. Hayashi, et al., eds., Japan Society for Composite Materials, Tokyo, 1982.
3. J.E. Hack and M.F. Amateau, eds., Mechanical Behavior of Metal-Matrix Composites, TMS-AIME, Warrendale, PA, 1983.
4. M. Vogelsang, R.J. Arsenault and R.M. Fisher, Met. Trans. A, 17A (1986) 379-389
5. L.J. Broutman and R.H. Krock, eds., Composite Materials, Vol. 1 to 4, Academic Press, New York, 1974.
6. C.A Hoffman, J. Engr. Mat'l. Technol. 95 (1973) 55-62.
7. G.J. Dvorak, M.S.M. Rao and J.Q. Tarn, J. Comp. Mat'l. 7 (1973) 194-216
8. A. Pawloski, Scr. Metall. 13 (1979) 791-794
9. A. Pawloski, Scr. Metall. 13 (1979) 785-790
10. J.C. Fisher and J.H. Holloman, Acta Met. 3 (1955) p.608
11. D. Turnbull, "Diffusion Short Circuits and their role in Precipitation", Defects in Crystalline Solids, The Physical Society, London, 1955.
12. J.W. Cahn, Acta Met. 5 (1957) p.169.
13. A.H. Cotterell and B.A. Bilby, Proc. Phys. Soc. (London) Section A62 (1949) 49
14. F.S. Ham, J. Appl.Phys. 30 (1959) 915.
15. R.M. Allen and J.B. Vandersande, Proceedings of and International Conference on Solid-Solid Phase Transformation, eds. H.I. Aaronson et al., TMS-AIME (1981) 655
16. R. Hill, The Mathematical Theory of Plasticity, Oxford, 1950, p.97-114.
17. D.L. Bourell and A.S. Rizk, Acta Met. 31 (1983) 609-617.
18. L.M. Kachanov, Foundations of the Theory of Plasticity, North Holland Publishing Company, 1971, p.118
19. O. Hoffman and G. Sachs, Introduction to the Theory of Plasticity for Engineers, Mcgraw Hill, 1953, p.80
20. W. Johnson and P.B. Mellor, Engineering Plasticity, Ellis Horwood Limited, Chichester, 1983, p.219
21. M.H. Rice and G.A. Gurtman, Residual Stresses in Fiber Reinforced Metal Matrix Composites, S-CUBED Report SSS-R-82-5447, March 1982 (Submitted to DARPA)

Composites, S-CUBED Report SSS-R-82-5447, March 1982 (Submitted to DARPA)

22. B. Karlsson and B.O. Sundstrom, Mater. Sci. Eng. 16 (1974) p.161.
23. B.O. Jaensson and B.O. Sundstrom, Mater. Sci. Eng. 9 (1972) p.217.
24. B.O. Sundstrom, Mater. Sci. Eng. 12 (1973) p.265.
25. MSC NASTRAN User's Manual, The MacNeal Schwendler Corp., Los Angeles, California
26. Metals Handbook, Vol. 2, 9th ed., ASM, Metals Park, OH.
27. L.M. Clarebrough, M.E. Hargreaves and M.H. Loretto, Recovery and Recrystallization of Metals, L. Himmel, ed., Interscience, 1963, p.63
28. Y. Nakada, Phil. Mag. 11 (1965) 251.
29. A. Wolfenden and A.S. Appleton, Acta Met 16 (1968) 915.
30. A. Wolfenden, Acta Met. 16 (1968) 975.
31. M.B. Bever, D.L. Holt and A.L. Titchener, Prog. in Mat'l. Sci. 17, Pergamon Press, 1973, p.23-51.

APPENDIX

When a body is deformed, most of the plastic work done, E_w, is dissipated, while the rest is stored as residual strain energy E_s. E_s may be written as a fraction of E_w as

$E_s = f E_w$,

where f is of the order of 0.1 [27-31]. Neglecting the effect of increased point defects, the residual stored energy may be equated to the increase in dislocation energy (ΔU_{disl}) which can be expressed as

$$\Delta U_{disl} = \alpha \Delta l\, G\, b^2$$

where Δl = increase in total dislocation length
G = shear modulus of the material
b = Burgers vector
and α = a constant.

But $\Delta l = V \Delta\rho$

where $\Delta\rho$ = increase in dislocation density due to plastic deformation
and V = volume of the body.

Hence $E_s = \Delta U_{disl} = \Delta\rho\, V\, G\, b^2$

and since $E_w = E_s/f = V\, G\, b^2\, \Delta\rho / f$.

Thus, the plastic work done is proportional to the increase in dislocation density due to plastic deformation. In the context of this work, E_w is the plastic work done on the matrix due to differential thermal contraction from the solutionizing temperature.

Table : Expended Plastic Work and Equivalent Plastic Strain for an Aluminum Matrix reinforced with 10 and 30 volume percent Silicon Carbide fibers having an aspect ratio of 3.

V_c (vol. %)	a/a_M	c_{max}/a	**Nature of Plastic Zones**	$E_w{}^m$ **(mJ/gm)**	**Equivalent Tensile Strain,%***
10	1.010	1.9	Non-interacting	26.451	0.36
30	1.010	1.9	Interacting	79.353	1.07 minimum

Data for Aluminum matrix : σ_{ys} = 200 MPa, E = 68950 MPa, ν = 0.33, ρ = 2.7 Mg/m^3,
$\alpha_M = 24 \times 10^{-6}\ {}^{o}C^{-1}$, ΔT = 505 ^{o}C.

Data for SiC fibers : $\alpha_D = 3.8 \times 10^{-6}\ {}^{o}C^{-1}$, A_r (aspect ratio) = 3,
V_{cmax} (Non-interacting plastic zones) = $\pi(a/c_{max})^2/4$ = 21.7 %
(Equation 7)

* The uniaxial plastic strain necessary to impart the plastic work equivalent to $E_w{}^m$ to a monolithic matrix. For the above data, ε^p (equivalent) = $E_w{}^m$ / (74,000 mJ/gm).

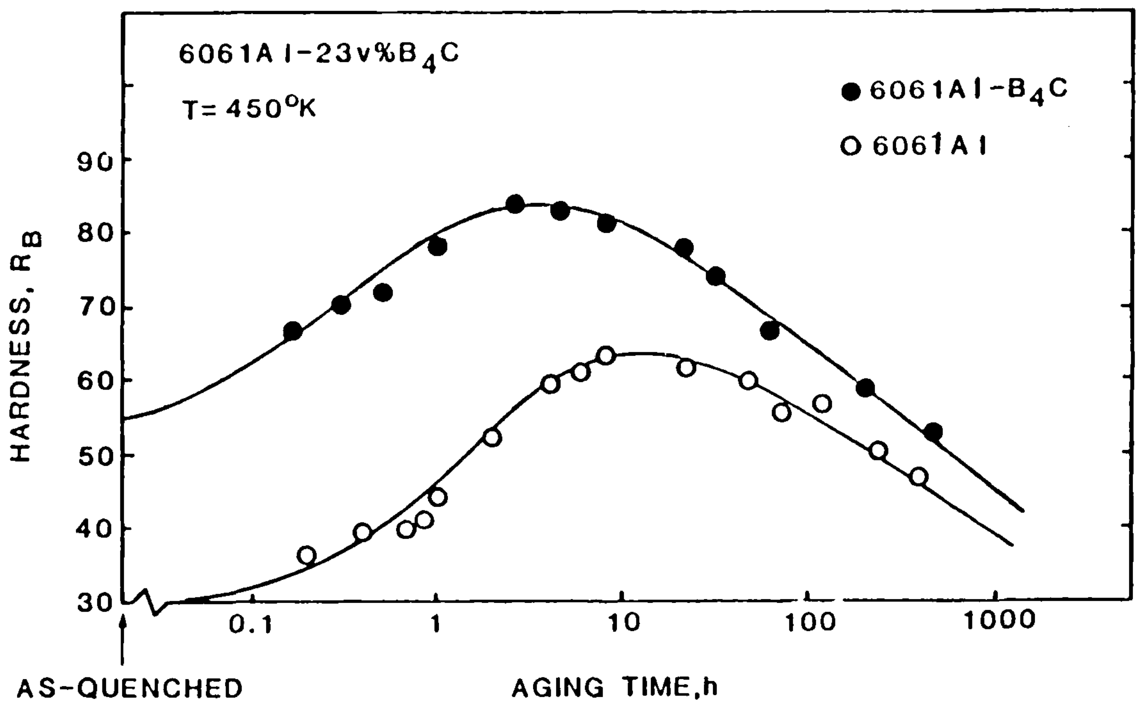

Figure 1 : Direct comparison of the aging characteristics of 6061 aluminum with and without B_4C reinforcement. The aging responses are similar except that the reinforced material ages faster (ref. 1).

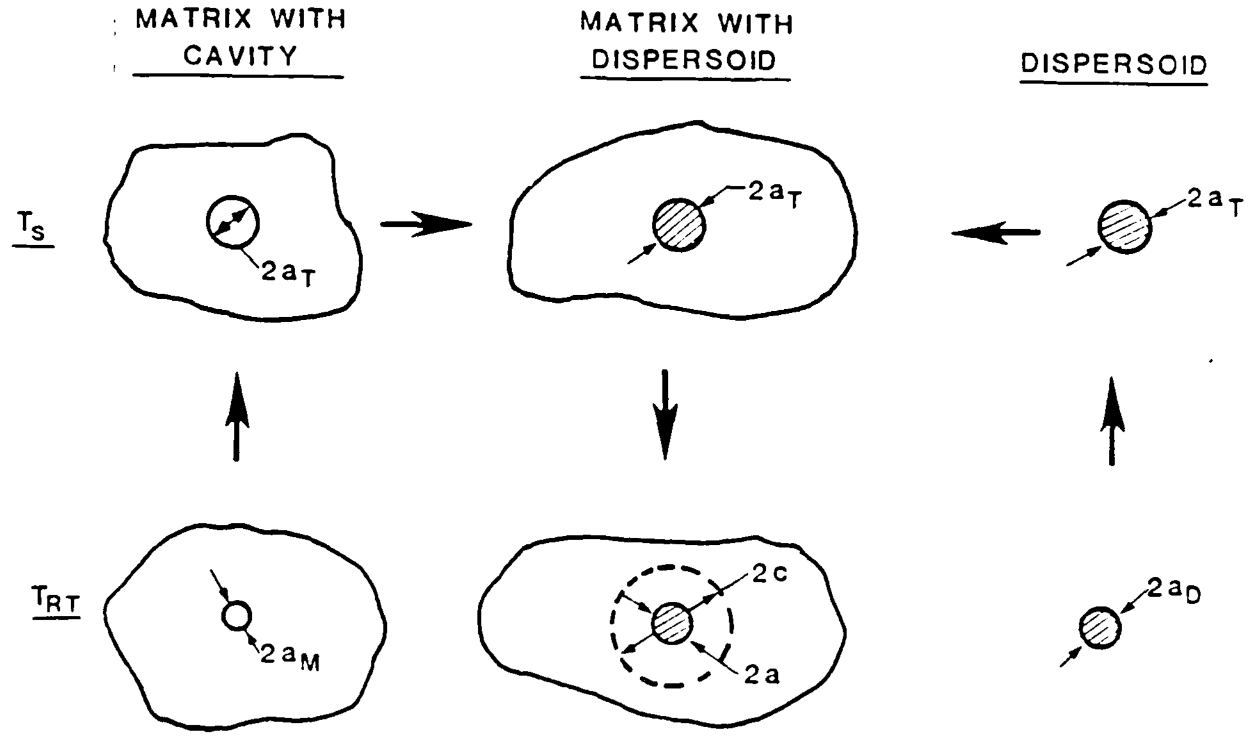
MATRIX WITH CAVITY
MATRIX WITH DISPERSOID
DISPERSOID
T_S
T_{RT}
$2a_T$
$2a_T$
$2a_T$
$2a_M$
$2c$
$2a$
$2a_D$

Figure 2 : A schematic of the composite solutionizing cycle, showing matrix, composite and reinforcement radii at room temperature T_{RT} and at the solutionizing temperature T_S.

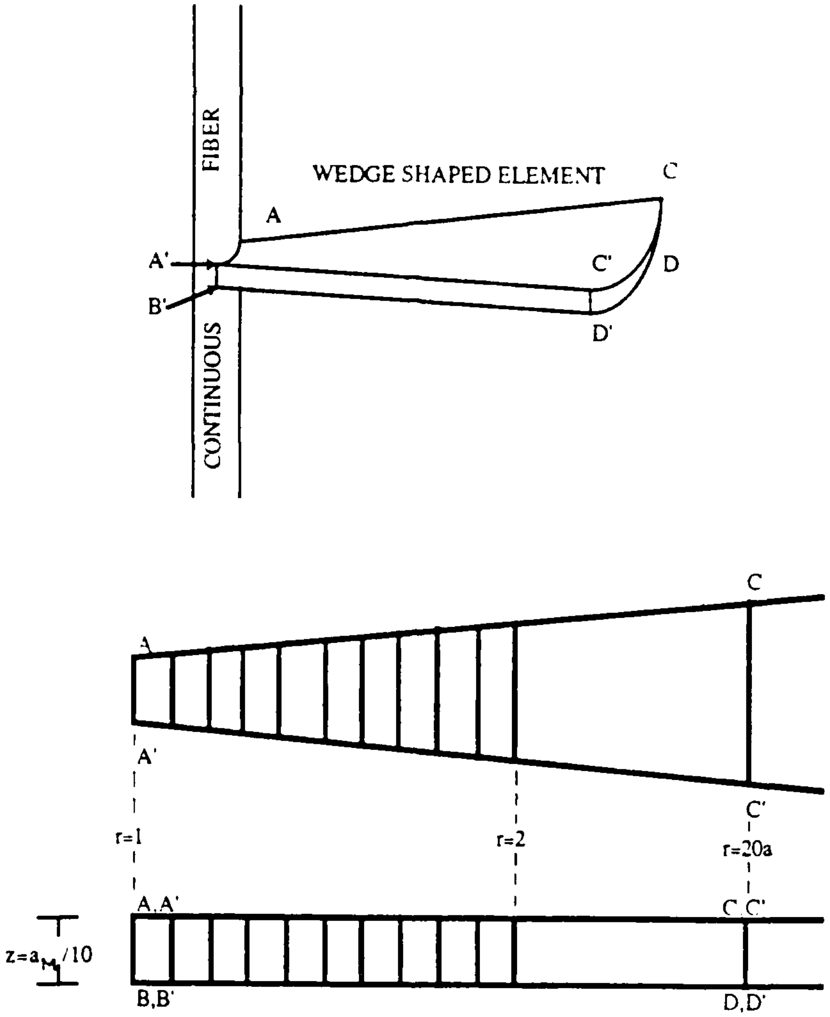
FIBER
CONTINUOUS
WEDGE SHAPED ELEMENT
A
C
A'
C'
D
B'
D'
A
C
A'
C'
r=1
r=2
r=20a
A,A'
C,C'
z=a_M/10
B,B'
D,D'

Figure 3 : The finite element gridwork used to model non-plane strain infinite length cylindrical fibers, showing a perspective view as well as the plan and elevation views of the wedge shaped matrix element.

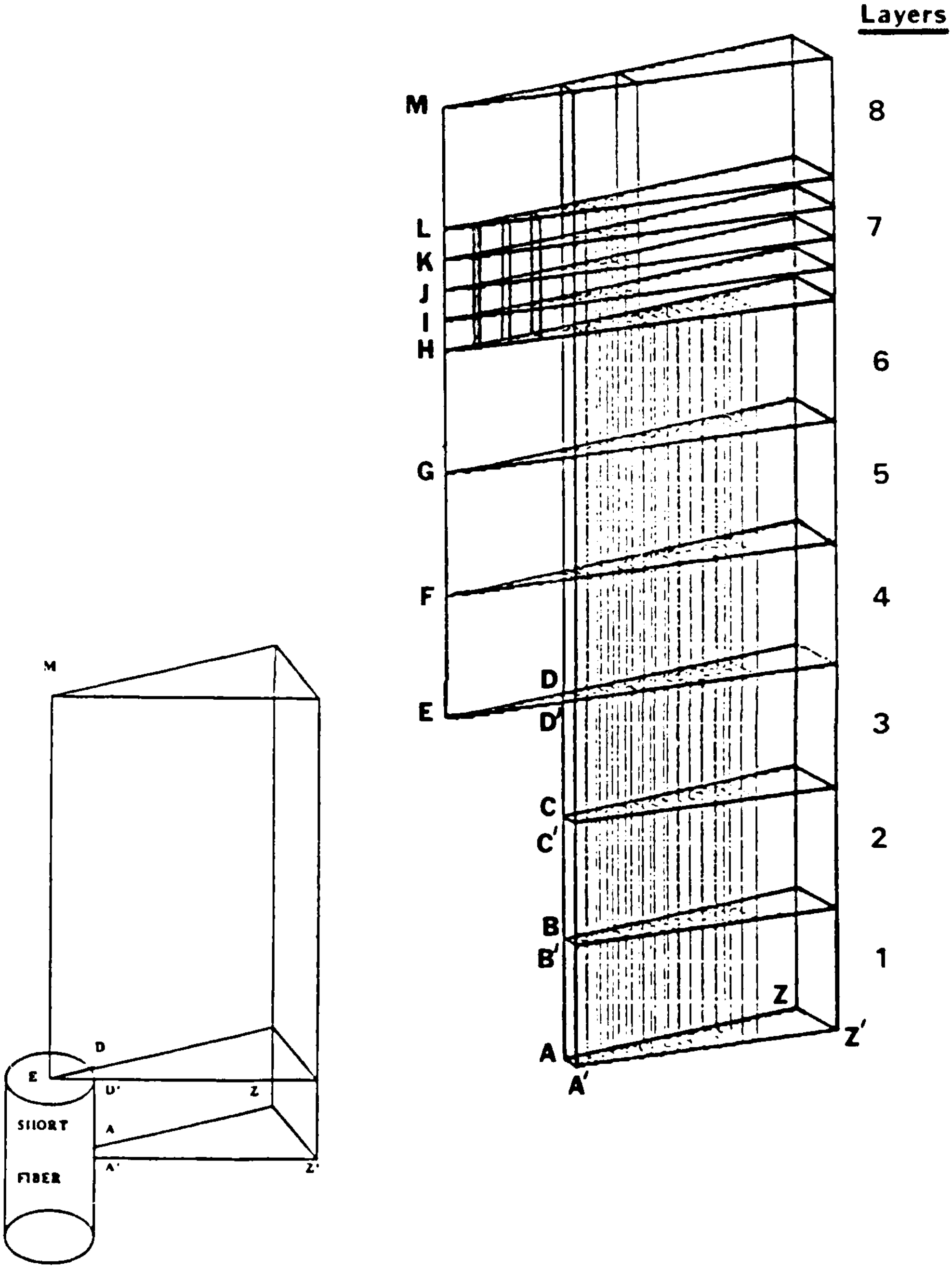
Layers
M
8
L
7
K
J
I
H
6
G
5
F
4
D
E
D′
3
C
C′
2
B
B′
1
Z
Z′
A
A′
M
D
E
D'
Z
SHORT
A
FIBER
A'
Z'

Figure 4 : The finite element gridwork used to model finite length cylindrical fibers. The gridwork was developed as part of the NASTRAN analysis. The gridwork shown was used to model a fiber of aspect ratio (length:diameter) three. The aspect ratio one reinforcement was modeled by eliminating layers 1,2,4 and 5.

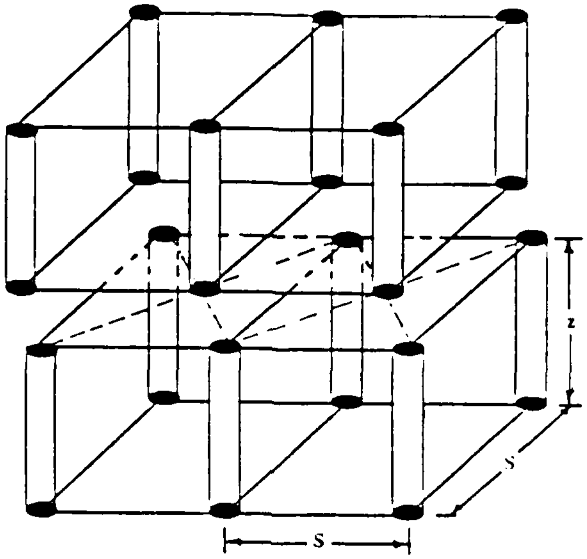

Figure 5 : Composite with discontinuous unidirectional fibers arranged in a square array such that the ends of fibers in the lower array lie on the same plane as fiber ends on the upper array.

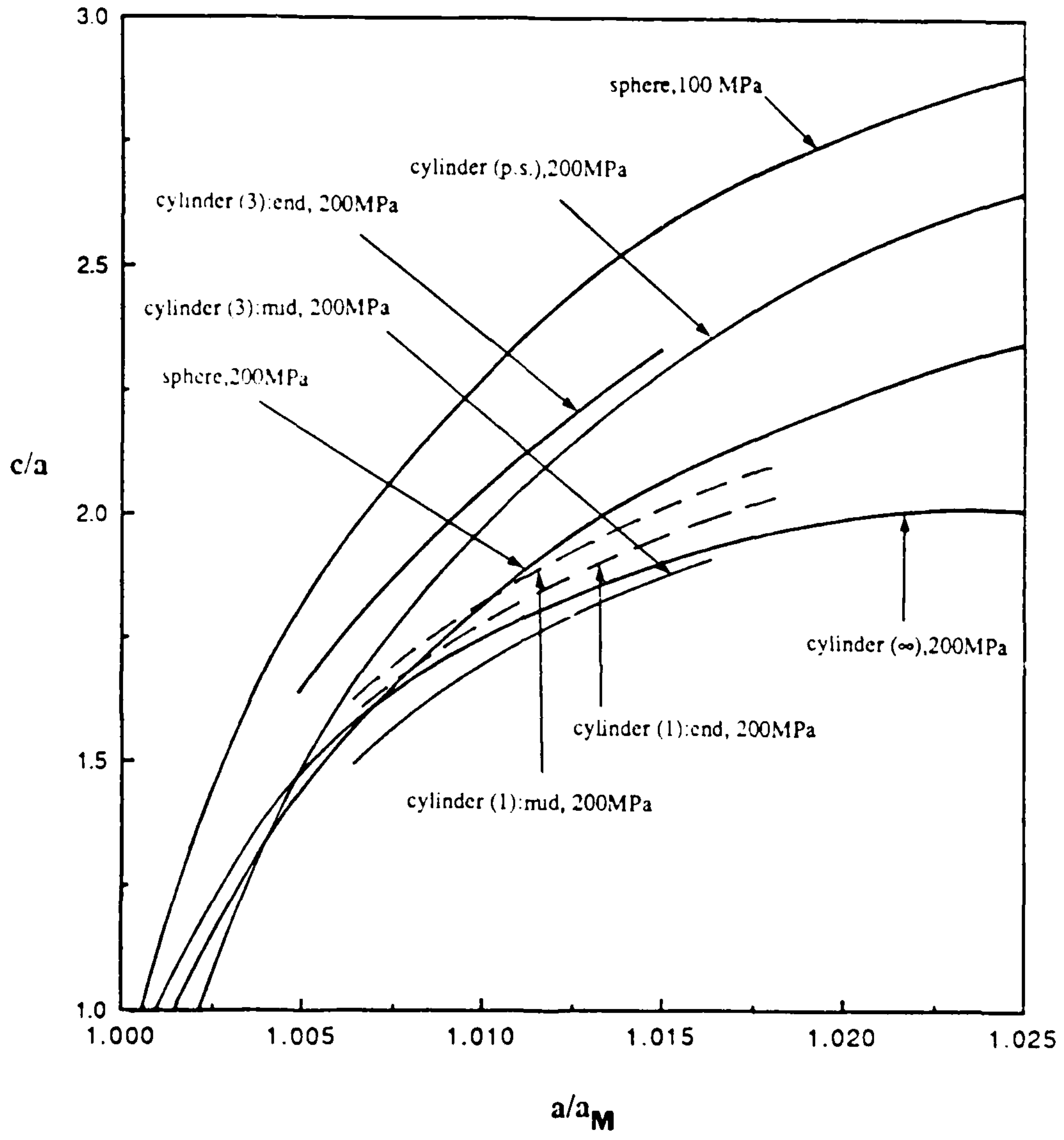

Figure 6 : Ratio of plastic zone radius to reinforcement radius (c/a) versus the relative matrix expansion (a/a_M) for SiC reinforced aluminum (see Table for material parameters) with the reinforcement aspect ratios indicated in parentheses. An increase in a/a_M produced by an increase in $(\alpha_M-\alpha_D)\Delta T$ (see equation 1) increases the plastic zone size for all reinforcement geometries. Decreasing matrix yield strength results in an increased plastic zone size as indicated by the curves for spherical reinforcements in matrices of yield strengths of 100 and 200 MPa.

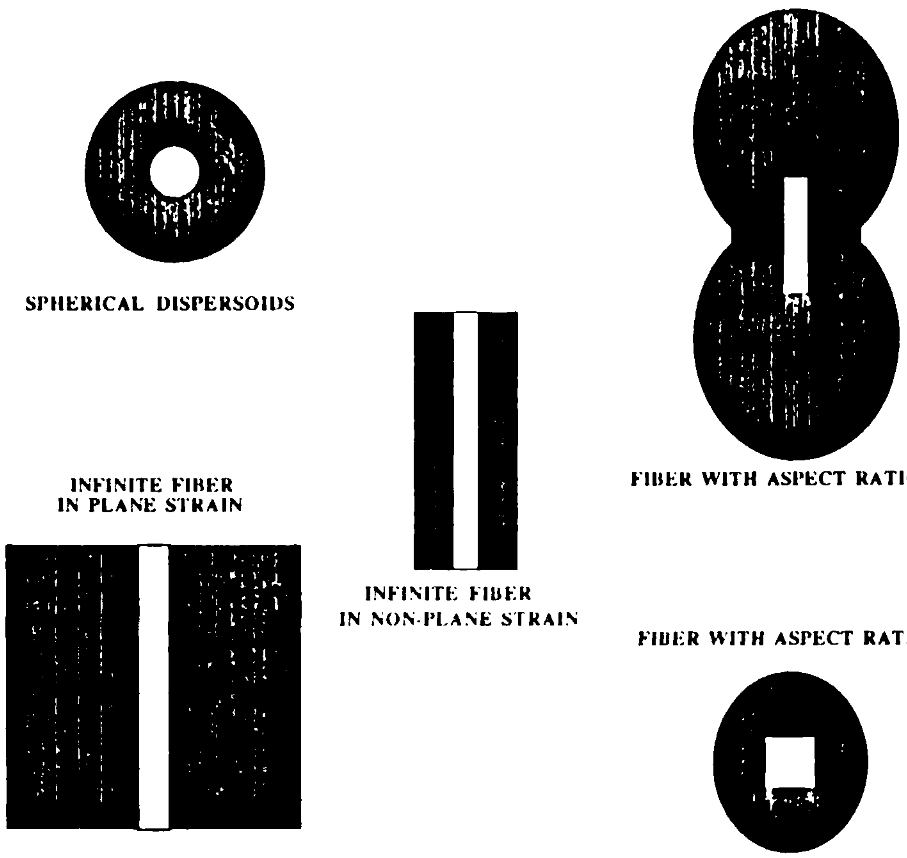
SPHERICAL DISPERSOIDS
FIBER WITH ASPECT RATIO = 3
INFINITE FIBER
IN PLANE STRAIN
INFINITE FIBER
IN NON-PLANE STRAIN
FIBER WITH ASPECT RATIO = 1

Figure 7 : Relative plastic zone size and shape (dark area) as a function of reinforcement particle shape (light area) for the geometries studied.

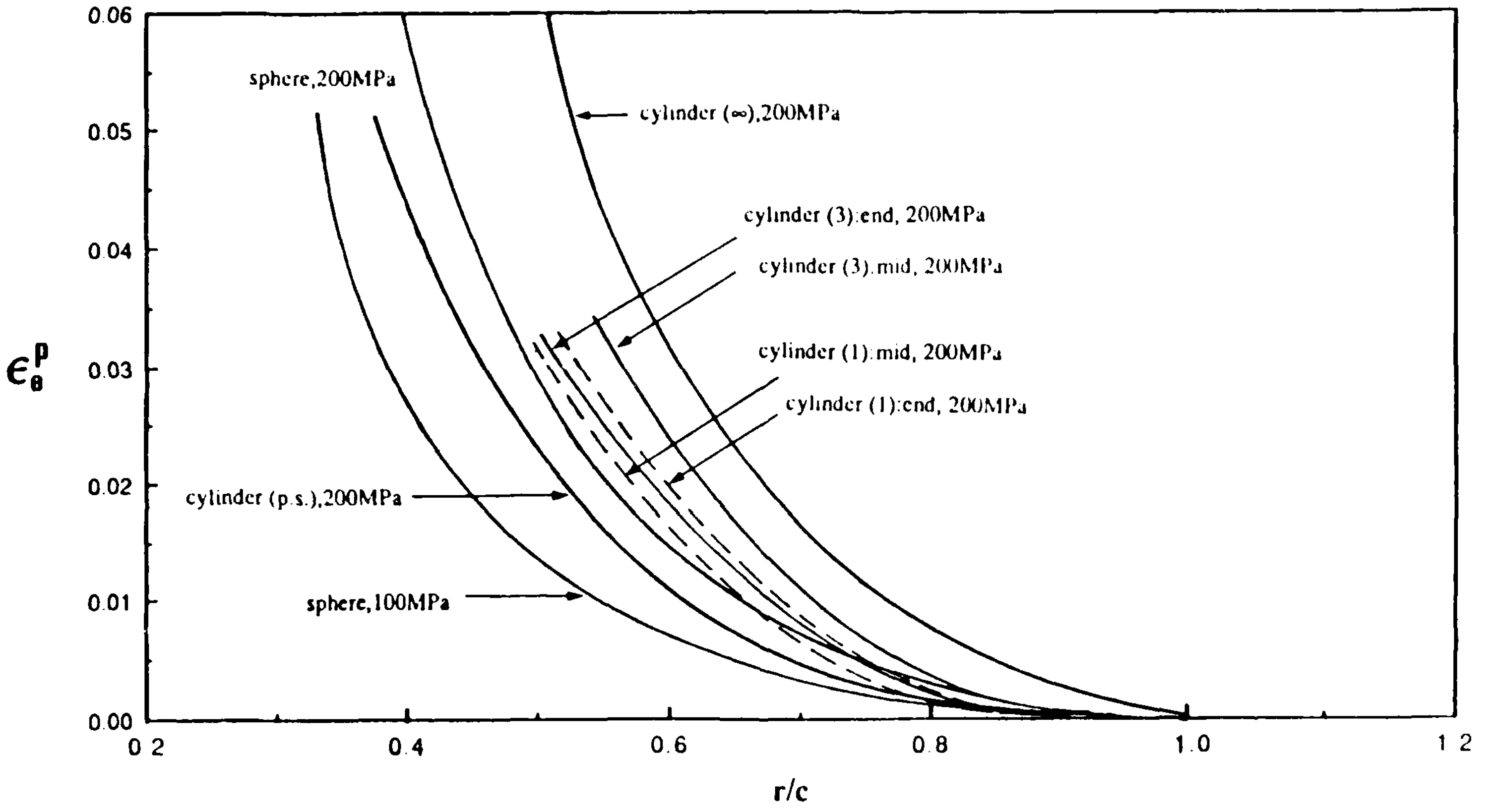

Figure 8 : Radial distribution of plastic strain (ϵ_e^p) away from the reinforcement for SiC reinforced aluminum (see Table for material parameters). For all geometries the plastic strain is greatest at the reinforcement-matrix interface (r/c=a/c) and decreases to zero at the elastic-plastic interface (r/c=1). Whereas decreasing the yield strength increases the plastic zone size (Fig.6), the plastic strain at a given r/c decreases, as shown for spherical reinforcements in matrices of yield strengths of 100 and 200 MPa.

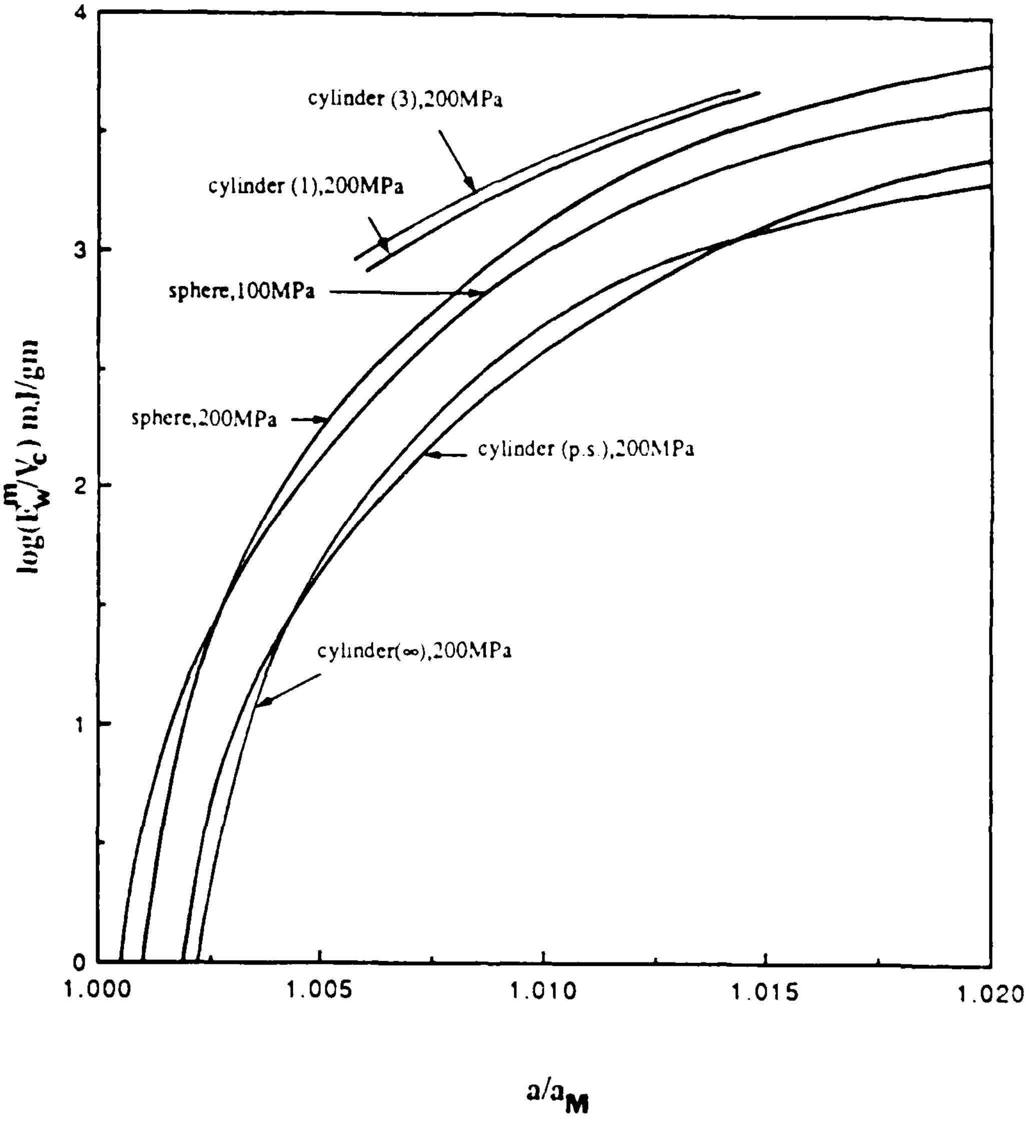

Figure 9 : A plot of the expended plastic work per unit composite mass per unit reinforcement volume fraction ($E_w{}^m/V_c$) as a function of relative matrix expansion (a/a_M) for SiC reinforced aluminum (see Table for material parameters). $E_w{}^m/V_c$ increases with increasing a/a_M. While weaker matrices yield earlier, they require less plastic work, resulting in smaller $E_w{}^m/V_c$ values at larger a/a_M, as evident from the curves for spherical reinforcements in matrices of yield strengths of 100 and 200 MPa.

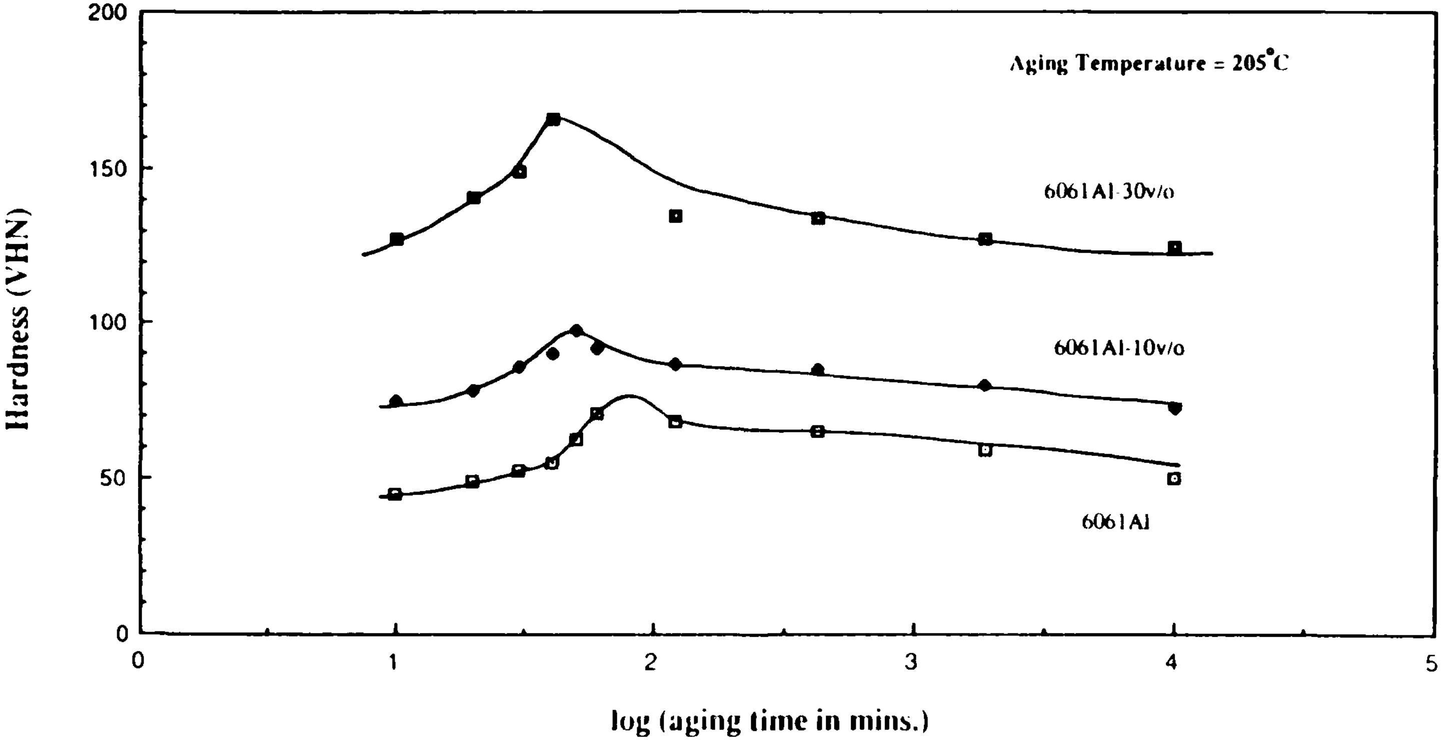

Figure 10 : Aging curves for 6061 aluminum without and with reinforcement with 10 and 30 volume percent SiC whiskers. The solutionizing temperature was 530°C ($\Delta T = 505°C$). The time to peak hardness decreases with increasing volume fraction.

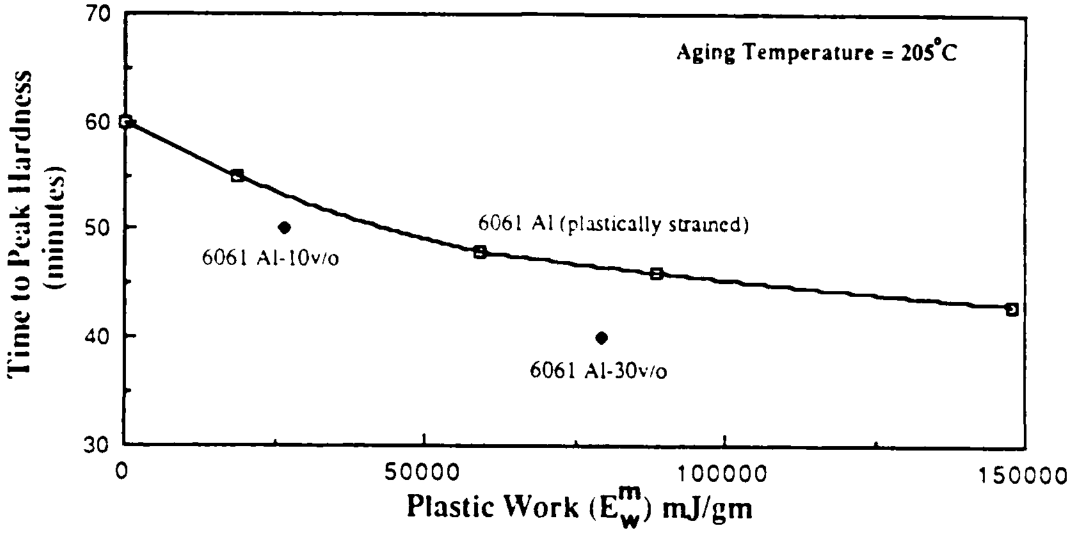

Figure 11 : Influence of expended matrix plastic work on the aging characteristics of 6061 aluminum. Open symbols represent monolithic 6061 plastically strained by varying amounts after solutionizing and quenching. The closed symbols represent 6061-SiC MMCs containing 10 and 30 v/o reinforcement. The extent of plastic work calculated from the model for the MMC is low relative to that required to produce the same time to peak hardness in the monolithic alloy.

LIST OF SYMBOLS

T_s = solutionizing temperature of matrix
T_{RT} = room temperature
a_D = radius of the free reinforcement at room temperature
a_T = reinforcement or matrix cavity radius at T_s
a_M = radius of the free matrix cavity at room temperature
a = radius of the constrained matrix or reinforcement in the composite
c = radius of the plastically deformed zone in the matrix
r = any arbitrary radial distance from the center of the reinforcement
z = length of fiber
α_D = thermal expansion coefficient of reinforcement
α_M = thermal expansion coefficient of matrix
σ_{ys} = matrix yield strength
E = matrix Young's modulus
v = matrix Poisson's ratio
ρ = matrix density
$\varepsilon_e{}^p$ = effective plastic strain in the matrix
$\varepsilon_e{}^E$ = effective elastic strain in the matrix
$\varepsilon_e{}^T$ = effective total strain in the matrix
S = spacing between adjacent fibers in a cubic array
V_c = volume fraction of reinforcement in the composite
E_w = plastic work expended in the deformation of the matrix by a single reinforcement
$E_w{}^m$ = expended plastic work per unit composite mass per unit reinforcement volume fraction
σ_θ = matrix stress in the θ direction in cylindrical or spherical coordinates
σ_ϕ = matrix stress in the ϕ direction in spherical coordinates
σ_z = matrix stress in the axial direction of the fiber in cylindrical coordinates

FIGURE CAPTIONS

Figure 1 : Direct comparison of the aging characteristics of 6061 aluminum with and without B_4C reinforcement. The aging responses are similar except that the reinforced material ages faster (ref. 1).

Figure 2 : A schematic of the composite solutionizing cycle, showing matrix, composite and reinforcement radii at room temperature T_{RT} and at the solutionizing temperature T_S.

Figure 3 : The finite element gridwork used to model non-plane strain infinite length cylindrical fibers, showing a perspective view as well as the plan and elevation views of the wedge shaped matrix element.

Figure 4 : The finite element gridwork used to model finite length cylindrical fibers. The gridwork was developed as part of the NASTRAN analysis. The gridwork shown was used to model a fiber of aspect ratio (length/diameter) three. The aspect ratio one reinforcement was modeled by eliminating layers 1,2,4 and 5.

Figure 5 : Composite with discontinuous unidirectional fibers arranged in a square array such that the ends of fibers in the lower array lie on the same plane as fiber ends on the upper array.

Figure 6 : Ratio of plastic zone radius to reinforcement radius (c/a) versus the relative matrix expansion (a/a_M) for SiC reinforced aluminum (see Table for material parameters) with the reinforcement aspect ratios indicated in parentheses. An increase in a/a_M produced by an increase in $(\alpha_M-\alpha_D)\Delta T$ (see equation 1) increases the plastic zone size for all reinforcement geometries. Decreasing matrix yield strength results in an increased plastic zone size as indicated by the curves for spherical reinforcements in matrices of yield strengths of 100 and 200 MPa.

Figure 7 : Relative plastic zone size and shape (dark area) as a function of reinforcement particle shape (light area) for the geometries studied.

Figure 8 : Radial distribution of plastic strain ($\varepsilon_e{}^P$) away from the reinforcement for SiC reinforced aluminum (see Table for material parameters). For all geometries the plastic strain is greatest at the reinforcement-matrix interface ($r/c=a/c$) and decreases to zero at the elastic-plastic interface ($r/c=1$). Whereas decreasing the yield strength increases the plastic zone size (Fig.6), the plastic strain at a given r/c decreases, as shown for spherical reinforcements in matrices of yield strengths of 100 and 200 MPa.

Figure 9 : A plot of the expended plastic work per unit composite mass per unit reinforcement volume fraction ($E_w{}^m/V_c$) as a function of relative matrix expansion (a/a_M) for SiC reinforced aluminum (see Table for material parameters). $E_w{}^m/V_c$ increases with increasing a/a_M. While weaker matrices yield earlier, they require less plastic work, resulting in smaller $E_w{}^m/V_c$ values at larger a/a_M, as evident from the curves for spherical reinforcements in matrices of yield strengths of 100 and 200 MPa.

Figure 10 : Aging curves for 6061 aluminum without and with reinforcement with 10 and 30 volume percent SiC whiskers. The solutionizing temperature was 530°C ($\Delta T = 505°C$). The time to peak hardness decreases with increasing volume fraction.

Figure 11 : Influence of expended matrix plastic work on the aging characteristics of 6061 aluminum. Open symbols represent monolithic 6061 plastically strained by varying amounts after solutionizing and quenching. The closed symbols represent 6061-SiC MMCs containing 10 and 30 v/o reinforcement. The extent of plastic work calculated from the model for the MMC is low relative to that required to produce the same time to peak hardness in the monolithic alloy.

BIOGRAPHICAL SKETCH

I. Dutta

Mr. Indranath Dutta obtained his B. Tech (Hons) from the Indian Institute of Technology at Kharagpur, India in 1983. He received his MS in Metallurgy and Materials Science from Case Western Reserve University in 1985, and is currently a Graduate Research Assistant in the Center for Materials Science and Engineering at The University of Texas at Austin, where he is working towards his PhD.

D.L. Bourell

Associate Professor Dr. David Bourell has been with The University of Texas since 1979, with a joint appointment in the Department of Mechanical Engineering and the Graduate Program in Materials Science and Engineering. He completed his BS in ME at Texas A & M University in 1975. He received MS and PhD degrees from Stanford University in 1976 and 1979, respectively. Dr. Bourell's areas of research interest are mechanical metallurgy, deformation processing and structure/property characterization of metals. He is a member of the TMS-Aime Shaping and Forming Committee. He was the 1986 recipient of the ASM Bradley Stoughton Award for Outstanding Young Teachers of Metallurgy.

D. Latimer

Mr. Doug Latimer was an undergraduate research assistant at The University of Texas at Austin in 1984 and 1985. He graduated with a BS in Mechanical Engineering in 1985. He is currently a Staff Engineer with Mechanical Repair and Engineering at Laporte, Texas.

Appendix J

A Theoretical and Experimental Study of 6061 Al-SiC MMC to Identify the Operative Mechanism for Accelerated Aging

I. Dutta and D. L. Bourell

I. Introduction

It has been proposed [1] that accelerated aging in Metal Matrix Composites (MMC) is a result of the increased dislocation density adjacent to the reinforcement. Increased dislocation densities next to the reinforcement were reported by several authors [2, 3], and it was found to be at least $10^{13}/m^2$. In the current work, 6061 Aluminum MMC reinforced with 10 v/o SiC fibers of variable aspect ratio (of the order of 5 to 25) was observed under the transmission electron microscope to study its precipitation behavior. Next, to determine the relative contributions of the dislocation or the residual stresses generated in the matrix due to differential thermal contraction, a theoretical model was developed to predict the rate of precipitation in the residual stress field of the matrix. This rate was then compared to the rate of precipitation due to an array of edge dislocations as predicted by Ham [4]. Finally, as a means to determine experimentally the contribution of the elastic stress field, monolithic 6061 Al specimens were plastically strained in uniaxial tension to match the matrix plastic work done in the composite material (as predicted in [1]) and then unloaded to believe the elastic strain. Differential scanning calorimetery was then done to obtain the activation energy for precipitation, and the result was compared to that of the composite.

II. Transmission Electron Microscopy

Observation using a JEOL 200 CX TEM at 200KV revealed a high dislocation density adjacent to the fibers of heat treated materials (Fig. 1). In the peak hardened material, the heavily dislocated areas next to the fibers show a high density of precipitate needles (Figs. 2a and 2b). The precipitate needles are oriented along the <100> of the aluminum lattice and are the first signs of zone formation in 6061. Some of the needles are found to have thickened into β' (transition Mg_2Si), also oriented along <100>. Figure 3 shows dislocations very close to the fiber-matrix interface, laced with needles and some rods. Figures 4a and 4b show two separate areas of overaged composite, one close to a fiber, and the other away from it. One of the grains in Fig. 4a, oriented in the proper 2-beam condition for viewing dislocations, reveals a considerably higher dislocation density closer to the fiber than away from it. It is also seen that the general density of Mg_2Si platelets (the black patches) is higher in the area next to the fiber (Fig. 4a). Fig. 4b represents the area of a triple grain boundary.

These TEM observations indicate strongly that zone and β' formation initiates on dislocations and the higher dislocation density generated next to the reinforcement while quenching from the solutionizing temperature is the principal contributor to accelerated aging.

III. Relative Effectiveness of dislocations and residual stresses

It has been reported [5] that the general sequence of precipitation in 6061 Aluminum is: supersaturated solid solution → vacancy-silicon clusters → vacancy rich Coherent Al-Mg-Si GP zones → disordered, partially coherent $<100>_{Al}$ needle shaped phase → ordered, partially coherent $<100>_{Al}$ needles → semicoherent, hexagonal (a = 7.05 Å, c = 4.05 Å) rods → semichoerent, hexagonal (a = 7.05 Å, c = 12.15 Å) rods → equilibrium β-Mg_2Si platelets. Thomas [6] also reported that the first indication of aging in Al-Mg-Si alloys is formation of Si clusters.

Since Si clustering is the first step in precipitation, its rate was studied theoretically in the residual stress field of the composite matrix, and then compared to its rate on an array of edge dislocations.

a. Si clustering in the residual stress field of matrix

Finite Element Analysis of a 6061 Al matrix reinforced with SiC fibers of a finite aspect ratio revealed the hydrostatic matrix residual stress to be compressive at the fiber-matrix interface. It climbed to a maximum (tensile) value at the interface of the plastically and elastically deformed zones in the matrix, and then tapered off to zero gradually. this is shown in Figure 5 at the middle of a fiber of aspect ratio 3. The nature of the hydrostatic stress distribution is consistent with that calculated by Evans and Ruhle [7] for a spherical reinforcement.

Since Si forms a substitutional solid solution with Al, its distortion field in the aluminum lattice can be assumed to be roughly spherical. Hence, the driving force of stress-assisted diffusion of Si in Al is relief of hydrostatic stresses [8,9]. Si has an atomic radius of 1-18 Å, and Al has an atomic radius of 1.43 Å. Hence the Si atoms will tend to diffuse towards the region of compressive residual stress, i.e., the reinforcement interface. But as Si diffuses to the interface, a concentration gradient builds up, opposing the stress assisted diffusion. The problem thus becomes one of diffusion in two opposing fields.

The equation of continuity is given by:

$$\frac{\partial p}{\partial t} = D\, \bar{\nabla} . \,(\bar{\nabla} p + \beta\, p\, \bar{\nabla}\, V) \qquad (1)$$

where p(r,t) = concentration of Si in the matrix as a function of time and distance from the fiber-matrix interface

D = diffusivity of Si in Aluminum

β = 1/kT where k = Boltzmann's const., T = absolute temperature

V interaction energy of the Si atom and the hydrostatic stress field

$$4\pi \left(\frac{r_{Si} - r_{Al}}{r_{Al}}\right) r_{Al}^{3}\, \sigma_h(r)$$

where r_{Si} = radius of the Si atom, r_{Al} = radius of the Al atom and σ_h = hydrostatic stress as a function of distance.

The diffusion of Si towards the fiber-matrix interface will continue till the concentration P attains a steady state. At any instant t, P can be obtained as a function of the radial distance r by solving equation (1) numerically. The instantaneous profile of p is shown in Figure 6. At any instant t, the amount of Si clustering is given by:

$$W(t) = \int_{r=1\ (\text{interface})}^{r=r_0(t)} p2\pi r dr - p_0\pi\, [\{r_0(t)\}^2 - 1] \qquad (2)$$

and the fraction of total Si clustered is given by:

$$x(t) = \frac{W(t)}{W(t_\infty)} = \frac{W(t)}{\displaystyle\int_{r=1}^{r=r_0(t_\infty)} p2\pi r dr - p_0\, \pi\, [\{r_0(t_\infty)\}^2 - 1]} \qquad (3)$$

where t_∞ = time taken by the concentration gradient to reach steady state. W(t) and X(t) were obtained by numerical integration after obtaining P as a function of r at different t's. the result is shown in Figure 7, where X(t) is plotted against t for Si clustering in Aluminum at 100°C (curve A).

b. Silicon clustering on a regular array of edge dislocations

Following Ham [4], a regular array of edge dislocations within a cylinder of radius r_s can be replaced by a single dislocation of effective capture radius R at the center of the cylinder. r_s is chosen such that $r_s = (\Gamma \rho_\perp)^{1/2}$, where $\rho_\perp$ = the dislocation density in the matrix. The fraction precipitated can then be expressed in terms of the lowest root (X_0) of an Eigenfunction expansion as follows:

$$X(t) \cong 1 - \exp(-X_0^2 Dt) \qquad (4)$$

except at very small t. Here

D = diffusivity of Si in Al and

$\lambda_0^2 \cong (2/r_s^2)\,[\ln(r_s/R) - 3/5]^{-1}$.

Assuming a matrix dislocation density of $10^{13}/m^2$ and a temperature of 100 °C, X(t) was plotted against t in Figure 7 (curve B).

Comparing curves A and B in Figure 7, it is seen that the rate of Silicon clustering in Aluminum is at least one order of magnitude faster in an array of edge dislocations ($P_\perp = 10^{13}/m^2$) than in the residual stren field of the fiber at 100 °C. Hence, it is inferred that the more rapid mechanism will dominate; that is, the high density of dislocations, and not the elastic strenfield of the fiber, is principally responsible for accelerated aging.

IV. Calorimetric Study

Differential scanning calorimetric (DSC) scans were run on three samples: (i) an unstrained monolithic 6061 Al specimen (ii) a monolithic 6061 Al specimen, plstically strained to 0.36% after solutionizing and before aging, and (iii) a 6061 Al - 10v/o SiC MMC. All samples were solutionized at 530 °C for 1 hour and water quenched before the test. the 0.36% plastic strain was imparted to the solutionized and quenched monolithic sample in uniaxial tension to match the calculated plastic work for the composite sample (assuming a fiber aspect ratio of 3) [1]. A typical DSC scan plot is shown for the composite material for a scan rate of 20 ° C/min. in Figure 8. The first exothemic peak was tentatively identified by electron microscopy as β′ (transition Mg_2Si) rod formation. The second exothermic peak is for equilibrium β-Mg_2Si formation, and the final endothermic peak is for β-Mg_2Si dissolution.

For analysis, the first exothermic peak was chosen. Figure 9 shows a TEM micrograph of the control 6061 Al alloy, solutionized, quenched, heated at 10 °C/min. to the end of the first peak, followed by cooling in flowing N_2. It is seen that the matrix is filled with rods and some plates, giving rise to streaking in the <100> direction in the diffraction pattern. This is consistent with the literature [6], which reports the rods to be β'-Mg_2Si and the plates to be β-Mg_2Si. Hence it is tentatively inferered that the first DSC peak is for β' formation. However, some plates have also formed, probably because the cooling rate was not fast enough.

The DSC data were converted into precipitated fraction versus temperature plots by partial area integration of the first exothermic peak, and then the activation energies for overall β' precipitation were calculated by making a plot of $\ln[(T_p-T_0)/Q]$ vs. $1/T_p$ [10,11] in Figure 10. Here T_p is the peak temperature, T_0 is the starting temperature of the DSC scan, and Q is the heating rate. It is seen from Figure 10 that while the activation energies for overall precipitation in the plastically strained monolithic alloy and the composite are almost the same (~21,000 cal/mol), the activation energy for β' precipitation in the unstrained monoithic alloy is considerably higher (~24,400 cal/mol). This once again leads to the conclusion that the dislocated matrix of the plastically strained 6061 Al and the composite matrix are equally conducive for β' precipitation, while the unstrained 6061 matrix is much unfavorable. Hence it is inferred that matrix dislocations are the principal contributors to accelerated aging in MMCs.

V. Conclusions

In this article, evidence is given to substantiate a dislocation mechanism for accelerated aging in precipitation hardening MMC, in deference to a residual stress mechanism. The material system was 6061 Al-SiC. It was shown theoretically that Si clustering, the first step in the aging process, is driven by dislocation enhanced diffusion more than the residual stress. A calorimetric study showed that the activation energy for aging of the MMC is identical to the activation energy for a uniaxially strained (and unloaded) monolithic alloy, both of which are lower than the activation energy of the annealed monolithic alloy.

References

1. I. Dutta, D. L. Bourell and D. Latimer, "A Theoretical Investigation of Accelerated Aging in Metal-Matrix Composites," submitted to the Journal of Composite Materials.
2. M. Vogelsang, R. J. Arsenault and R. M. Fisher, Met. Trans. A, 17A, (1986) 379.
3. T. Christman and S. Suresh, "Microstructural Development in an Aluminum Alloy-SiC Whisker Composite," Brown University Report No. NSF-ENG-8451092/1/87, June 1987.
4. F. S. Ham, J. Appl. Phys., 30 (1959) 915.
5. H. J. Rack and R. W. Krenzer, Met. Trans. A, 8A (1977) 335.
6. G. Thomas, J. Inst. Metals, 90 (1961-62) 57.
7. A. G. Evans and M. Ruhle, Mat. Res. Soc. Symp. Proc. Vol. 40 (1985) 154.
8. "Introduction to Dislocations," D. Hull, p. 235-236.
9. "Dislocations and Plastic Flow," A. H. Cotterell, p. 56-57.
10. J. A. Augis and J. E. Bennett, J. Thermal Anal., 13 (1978) 283.
11. H. Yinnon and D. R. Uhlmann, Journal of Non-Crystalline Solids, 54 (1983) 253-275.

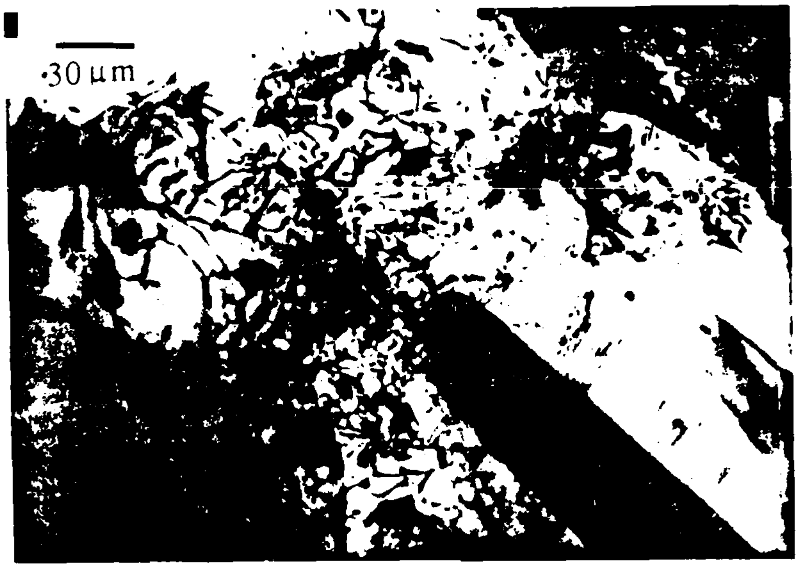

Figure 1: SiC fiber ends with adjacent dislocations

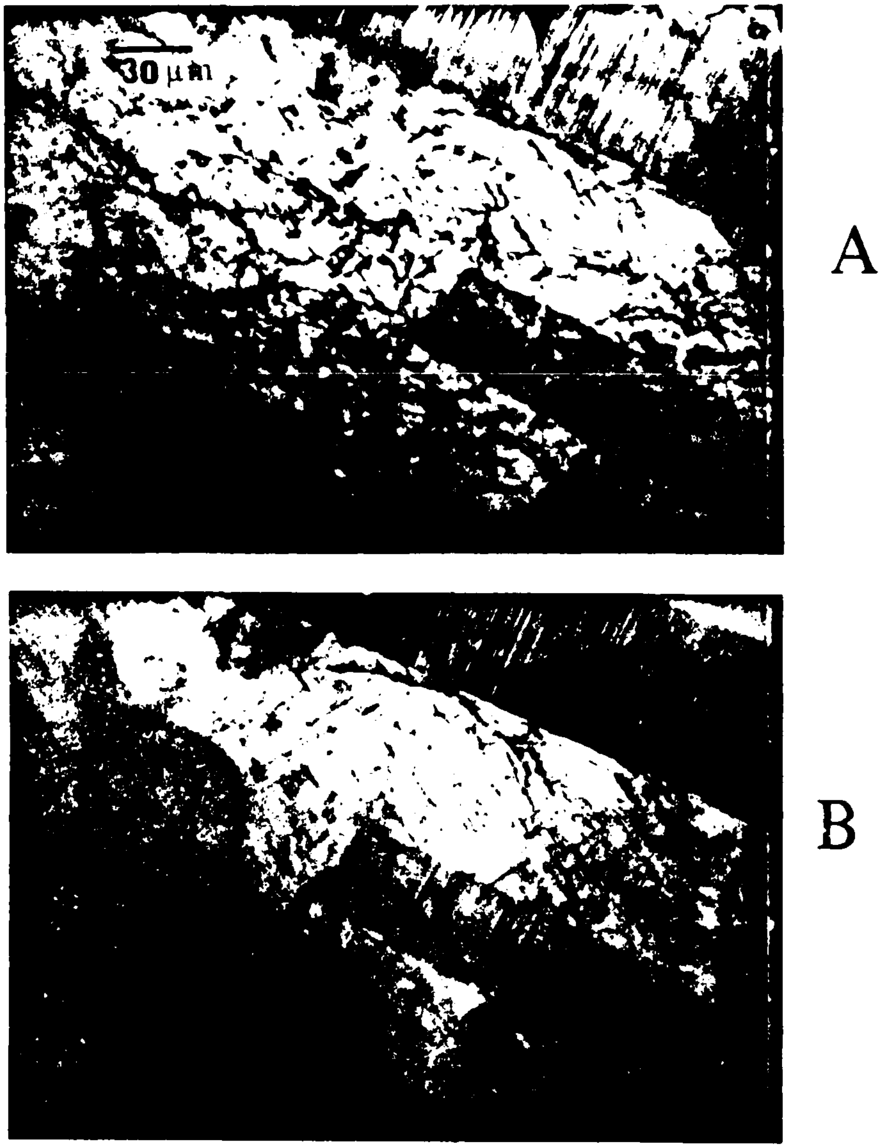

Figure 2: (A) Two SiC fibers with adjacent network of dislocations in the peak hardened material. Some precipitate rods and needles are also visible.

(B) The same area at a different orientation. The dislocations are not visible, but a high density of needles and some rods are seen where the dislocations were in A.

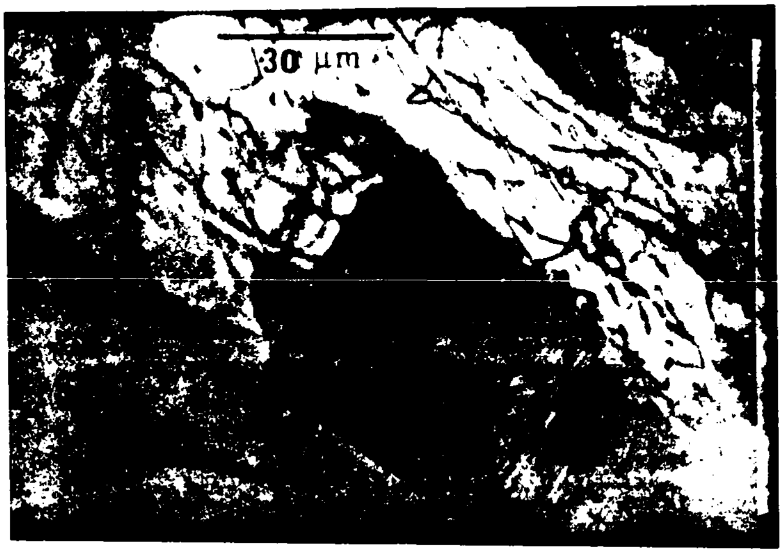

Figure 3: A SiC fiber end with adjacent dislocations laced with precipitate needles in the peak hardened material.

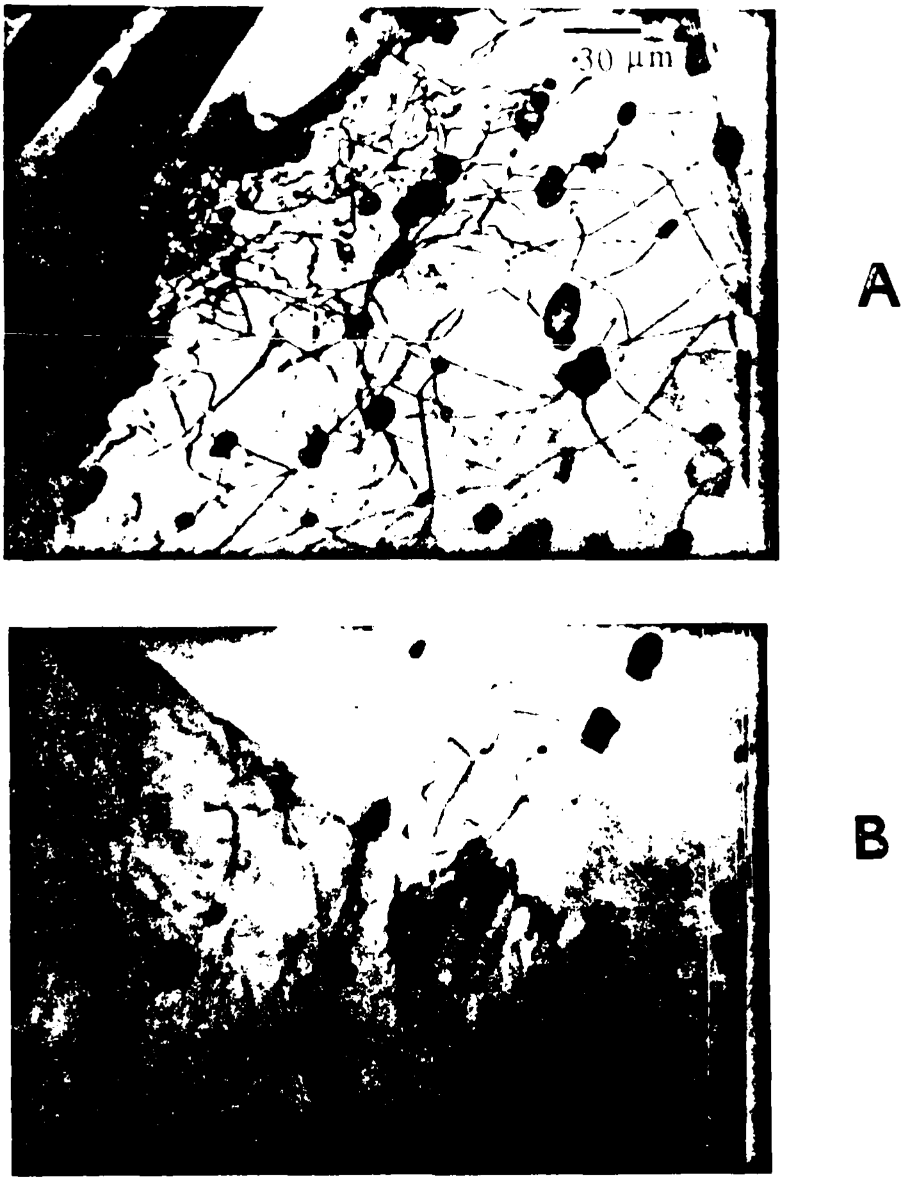

Figure 4: (A) The overaged specimen showing a grain next to a SiC fiber oriented properly for viewing dislocations. The dislocation density is higher closer to the fiber. A high Mg_2Si plate concentration is also seen. Some of the disloctaions seem to have been punched out of the precipitate particles.

(B) A triple grain boundary with no SiC fibers close by, showing a much lower dislocation density. Also, a considerably lower precipitate concentration is seen.

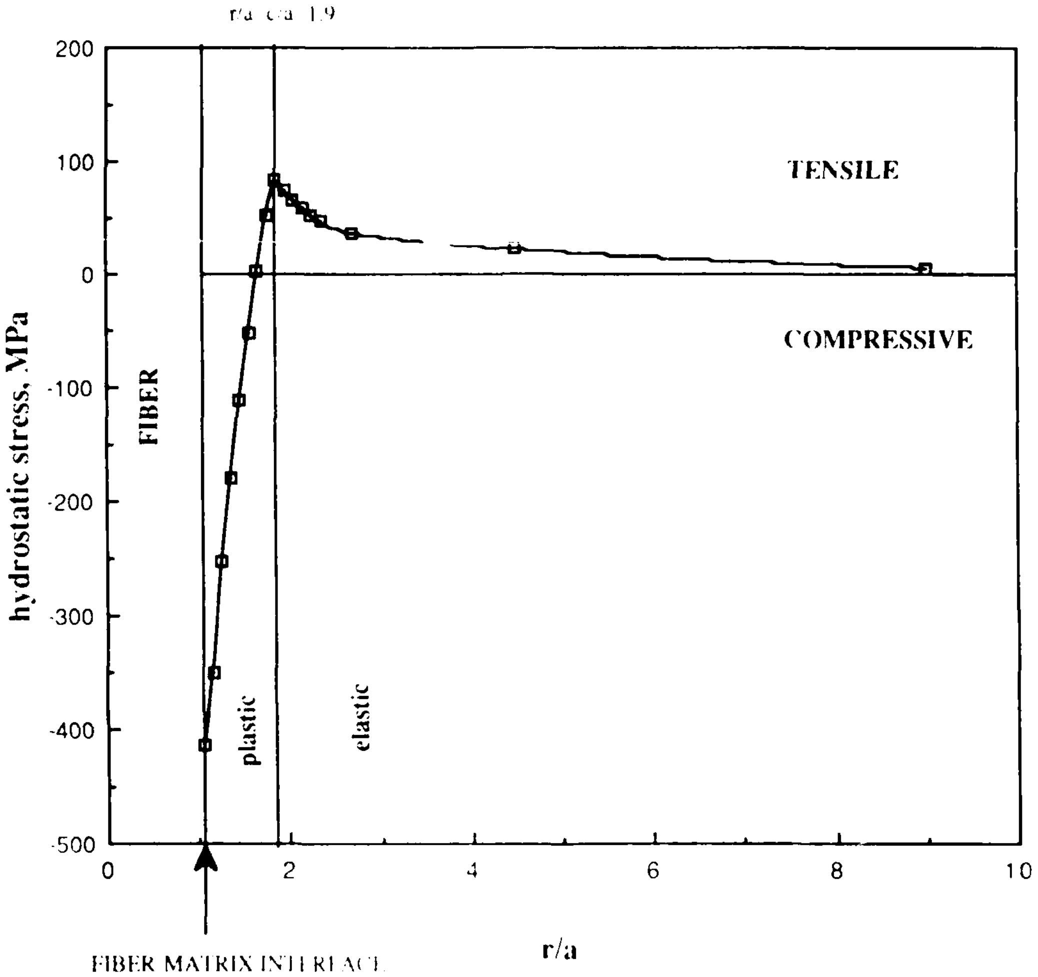

Figure 5: Hydrostatic stress distribution in the matrix next to the fiber. The stress is compressive within the plastically deformed zone, peaks out at the plastic-elastic interface, and gradually tails off in the elastic region.

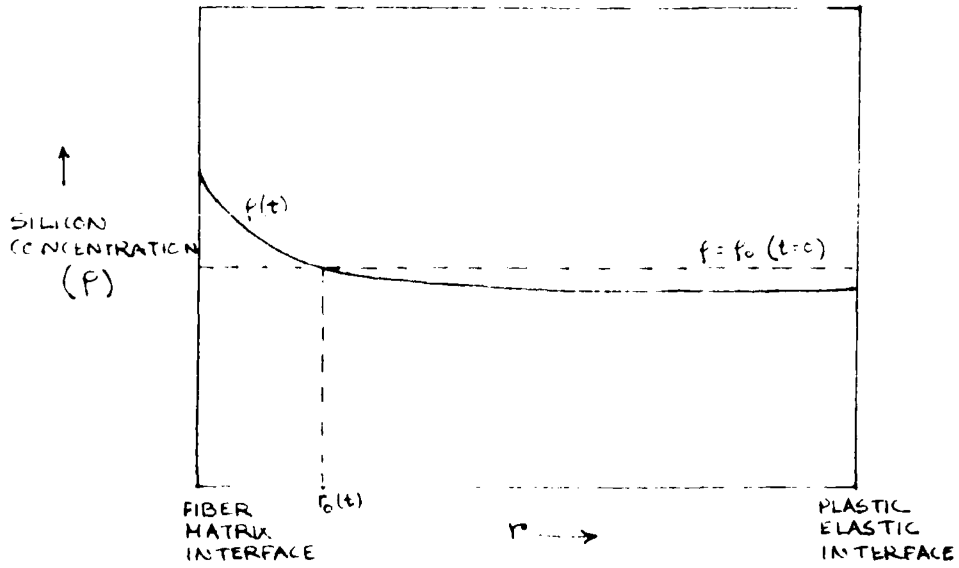

Figure 6: Transient Silicon concentration profile at time t. The initial uniform concentration is ρ_0. $r_0(t)$ is the distance from the fiber-matrix interface within which the Si concentration has risen above ρ_0 at time t, i.e., clustering has taken place.

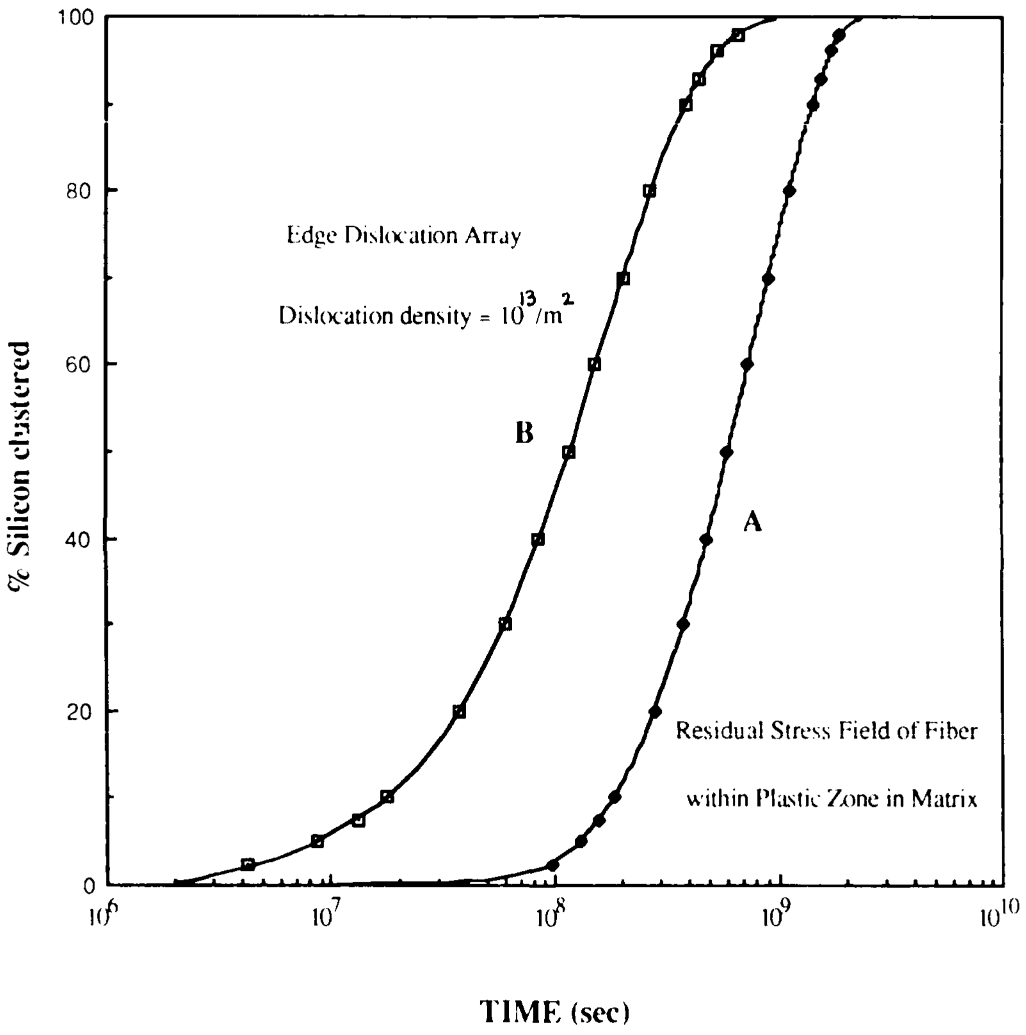

Figure 7: Compartaive Si clustering rates on an edge dislocation array of density $10^{13}/m^2$ and the residual stress field of the fiber in the composite at 100°C.

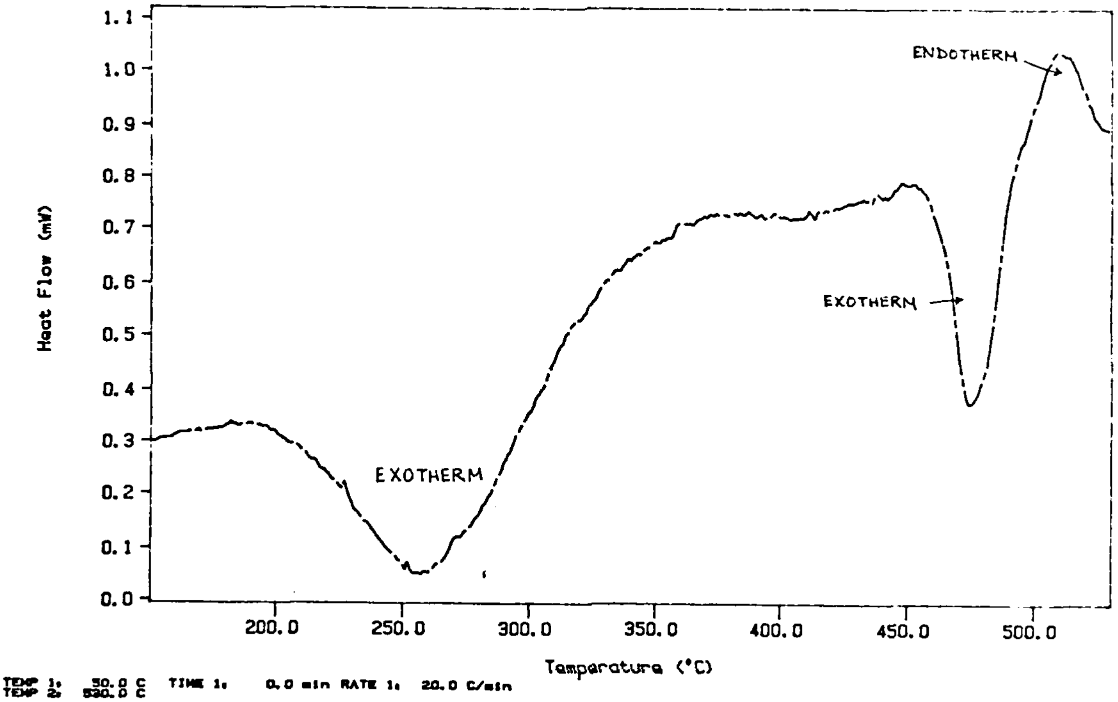

Figure 8 : DSC scan for the composite material at 20°C/min.

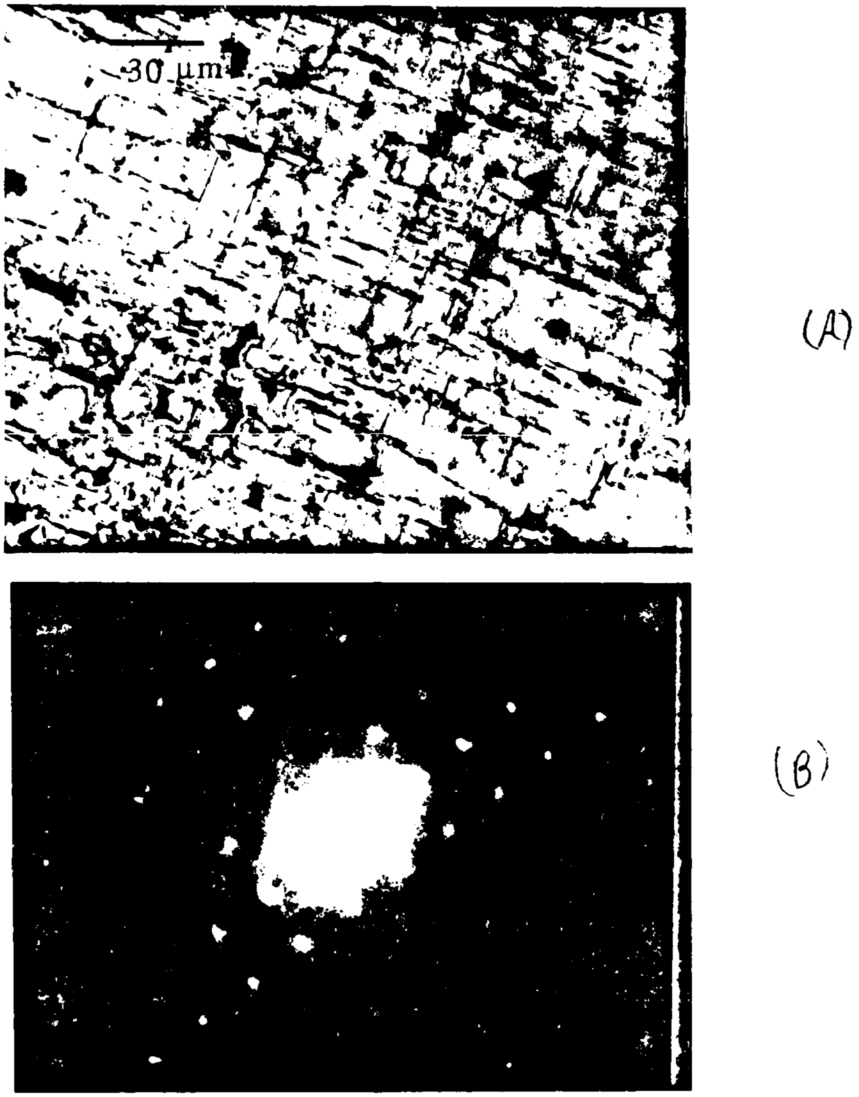

Figure 8: (A) The Control 6061 Al alloy after the first exothermic peak. The matrix contains a large density of rods and some plates. The rods are considered to be β' Mg_2Si and the plates β-Mg_2Si.

(B) The corresponding SAD pattern with the zone axis oriented along <001>. Streaks are seen along the <100> directions, indicating that the rods are oriented along <100> Al and the plates are on the {100} planes of Al.

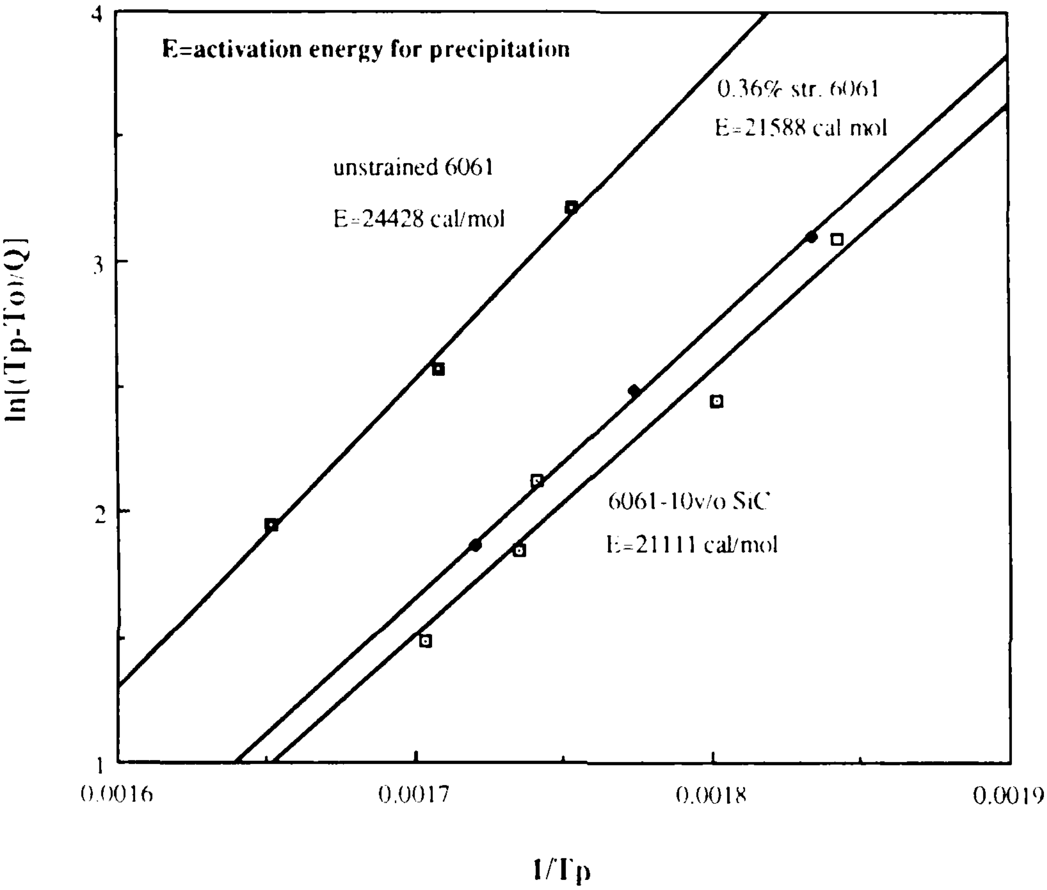

Figure 9: A plot of ln [(Tp-To)/Q] vs 1/Tp obtained from DSC scans at different heating rates. The slope of this curve gives the overall activation energy of β'-precipitation. It is seen that the unstrained 6061 has a considerably higher activation energy than the composite or the plastically strained 6061 alloy.

Appendix K*

HIGH ENERGY-HIGH RATE POWDER PROCESSING OF ALUMINUM-SILICON CARBIDE METAL-MATRIX COMPOSITES

G. Elkabir, C. Persad and H. L. Marcus

Approach

This study presents the results of an attempt to prepare optimized Al/SiC metal-matrix composites by incorporating SiC powders in an Al matrix while retaining the fine matrix microstructure obtained from the rapidly solidifed aluminum powders. To achieve this goal, a novel high energy-high rate type of processing was applied. The approach used a homopolar generator as the power source to supply a very short, high-current discharge pulse which when combined with an applied stress consolidates the powders compacts. The powder mixture is contained in an electrically insulated die and rapidly densified and metallurgically bonded due to the pulse resistive heating produced at interparticle interfaces, with total heating time of about one second. The material systems that were processed include several types of high-strength P/M aluminum alloys; X7091, CW67, 7064 and a high temperature Al-8% Fe-4% Ce alloy, combined with various types and grades of discontinuous silicon carbide with both α-hexagonal and β-cubic crystal structure.

This study focused on a detailed fundamental study of the processing/microstructure/property relationships, conducted in P/M SiC/Al composites with particular interest in microstructural evolution in the powder matrix, and in evaluation of the chemical nature of the metal (Al) - ceramic (SiC) interface. The interface bond characteristics have been correlated to the fracture properties of these materials. The microstructure and the phases that evolved during the consolidation were referenced to that of the microstructures of the pre-consolidated powders. The influence of the oxide present on powder particle surfaces have been examined and related to post-consolidation properties

---

*Details of this work are documented in a PhD dissertation. Reference: G. Elkabir, High Energy-High Rate Powder Processing of Aluminum Silicon Carbide Metal-Matrix Composites, The University of Texas at Austin, August, 1987.

Results

1. Powder Characterization.

The Al alloy particles are irregular in shape with a microstructure consisting of primary dendrites characterized by 0.5 µm arm-spacing, surrounded by an intercellular solute-rich phase network. Most of the particle surfaces are covered with an oxide layer approximately 70 Å thick. This oxide is rich in Al, Mg and O with smaller amounts of elemental Si.

The silicon carbide powder particles were covered with SiO_x type of oxide with some minor impurities such as P, Cl, S, Fe and Al. The α-SiC powder was analyzed by X-ray diffraction and found to be composed of two polytypes, belonging to the hexagonal system: Moissanite-6H SiC II and the 8H variants. In addition, the powder is not pure α-single phase but contains some small amounts of β-phase SiC. The β-phase SiC was categorized as (SiC) 8F polytype, belonging to the cubic system. This type of powder contains also some amount of elemental carbon which was identified as the graphite - 4H polytype.

2. Microstructure.

Processing/structure/property correlations have shown specific input energy and applied pressure to be crucial in controlling the type of microstructure and properties obtained from the consolidated materials. Energy inputs of 400 kJ/kg to 2,500 kJ/kg at applied pressures of 100 MPa to 450 MPa have resulted in consolidated forms with densities of 85% to 99% of theoretical, accompanied by a hardness value as high as 88 Rb. For low energy compaction (up to about 800 kJ/kg) the consolidated material has a low density (≅ 88% of theoretical) and can be still considered to be a green compact. At higher compaction energies (up to 2,500 kJ/kg) densities greater than 95% of the theoretical value have been achieved. At the highest energy input some interparticle melting assists in densification. The hardness and strength increases with the measured density except for the very low density consolidated material which can be regarded as a nearly green compact and therefore the hardness readings are not conclusive.

This high energy-high rate powder consolidation process proved to be capable of retaining, to a large extent, the original fine microstructure of the rapid solidified rate Al powders. No excessive increase in the size of the microstructural features was observed. At the low specific energy input (~400 kJ/kg) the consolidated X7091 Al has a fine, dendrite structure with copper-rich and cobalt-rich phases primarily in the interdendritic regions. This morphology is very similar to that of the as-received powder which has a dendrite-arm spacing of approximately 0.5 µm. Occasionally a cobalt-rich dispersoid phase was found within a dendrite arm. The intermediate energy input specimens (~800 kJ/kg) show the beginning of solute-particles at the margins of the prior interdendritic regions. Most of the prior interdendritic regions are transformed to small angle grain boundaries. Microdiffraction from both sides of these boundaries indicates a misorientation angle of less than 5 degrees. At high energy input (~2,500 kJ/kg) the material becomes partially recrystallized. It has a fine substructure with cobalt-rich insoluble particles (dispersoids) decorating the small angle boundaries. Most of the dispersoids were found to be based on the $(Co, Fe)_2 Al_9$ phase with Co:Fe ratio of about 4:1. The $(Co, Fe)_2 Al_9$ particles are essentially spherical in shape with a size in the range of 0.05-0.2 µm. Other types of dispersoids such as $Al_7 Co Cu_2$ have also been identified in the consolidated X7091 Al. A large fraction of the copper-rich phases seem to have been dissolved during the highest energy pulses as almost all the remaining particles are

$(Co, Fe)_2 Al_9$. Elemental microanalysis of the matrix showed that no significant amount of cobalt and iron is present, indicating that these elements have been almost completely precipitated out of the matrix. No significant coarsening of the dispersoids was observed. In almost all cases the precipitates were incoherent with respect to the matrix. The lack of coarsening is attributed to the relatively short time at temperature and the low solubility of the elements in the Al alloys limiting the solute flux between particles. TEM analysis of thin foils of 7064 Al consolidated material revealed that the intercellular regions have a glassy characteristic with some microcrystallinity, identified as γ - Al_2O_3 or $MgAl_2O_4$ - spinel.

The microstructure of the Al-matrix in CW67 Al-MMCs consists of fine primary dendrites, bounded by an intercellular network enriched with Zn, Mg, and Cu. Most of the insoluble particles were identified as $(Ni,Fe)_2 Al_9$ having similar morphology to the $(Co,Fe)_2 Al_9$ identified in the X7091 Al. MMCs (CW67 + α - SiCp) which were consolidated at the highest energy level ($\geq$ 2,500 kJ/kg) revealed fine, needle-shaped precipitates in the CW67 Al matrix. These precipitates were identified as the metastable, partially coherent, η'-phase, which possesses an orientation relationship with respect to the Al-matrix along the [111] direction. This structural feature is consistent with a rapid heating to a high temperature, following by fast cooling, similar to a solution heat treat and quench cycle. Good bonding was found to exist at the interface between the ceramic phase and the Al-matrix, as observed in TEM. This interface is continuous with thickness of about 100 Å.

3. Interface Analysis

Surface and interface studies of several of the Al/SiC MMC systems were conducted using Auger-electron spectroscopy. In general, the fracture path of all MMCs was found to be associated with an oxide layer, rich in Mg (predominantly), Al, O and C in the "graphitic" form containing small amounts of elemental Si and S. This oxide layer is in the form of mixed crystalline ternary or quarternary oxides of unknown stoichiometry as well as complex oxide glass. The complex oxide phase apparently involves the existence of a spinel - $MgAl_2O_4$ compound, but the thin layers were difficult to analyze. For MMC samples which were post-consolidated heat treat (300 °C for 1 hour) the oxide thickness associated with the fracture path was increased. This observation could be linked to the agglomeration of the interparticle oxide layer found when tensile specimens were heat treated in the same manner. As inert ion sputtering of the fracture surface proceeds towards a SiC particle, the peak signal associated with MgO_x was diminished, while more AlO_x/AlC_y ("carbidic") mixture phase was observed. It was also observed that the signal associated with the AlC_y increased as the peak associated with the AlO_x decreases as sputtering further continued towards the SiC particle. Sputtering towards the Al-matrix revealed a mixture of AlO_x/AlC_y ("graphitic") with a high concentration of Cu, Zn and Si (elemental) at the beginning of the sputtering. The final stage involved a significant reduction in the oxygen content and simultaneously an increase in the metallic Al peak as determined by Al peak shape and energy. A schematic pictoral representation of the characteristics of this interface is given in Figure 1.

Conclusions

The following conclusions can be made from the research reported in this work:

1. Al/SiC discontinuous composites with densities of up to 99% of the theoretical density were made in a processing time of about one second, using a high energy-high rate powder consolidation method. In densities greater than 95% of the theoretical, some very local interparticle melting contributes to densification at the highest energy level.

2. Several MMC systems have been successfully consolidated, including two different Al-matrices (X7091, CW67 and Al-8% Fe-4% Ce alloys) with various type and grades of discontinuous silicon carbide reinforcement (both whisker and particulates) in volume fraction of up to 30 percent.

3. Using the graphite-enriched β - SiC enabled an increase in the volume fraction of the ceramic reinforcing phase. This was due to a better electrical conductivity associated

with the graphite on its surfaces. The influence of graphite lubricity may also play a role in the process.

4. There is a direct correlation between the density, hardness and tensile fracture stress, and the specific-energy input associated with the high energy-high rate consolidation process.

5. SiC/Al metal-matrix composites consolidated at specific energy inputs of less than about 400 kJ/kg tend to retain the original rapid-solidified rate powder microstructure, but act as a green compact. At higher energy input the solute-rich phase between dendrite arms spheroidize and/or dissolve; and small Co-rich (in X7091 Al) and Ni-rich (in CW 67 Al) dispersoids are retained with very little coarsening.

6. The ductility of the MMCs was very low and is attributed to the lack of plastic deformation during the processing of these materials. Subsequent, in-situ, high rate processing such as forging or extrusion appear to be an appropriate approach to be taken in order to up-grade the mechanical properties of the composites.

7. The nature of bonding between the SiC to the Al-matrix, based on transmission electron microscopy study and Auger-electron spectroscopy analysis appear to be good, showing a continuous interface layer, approximately 100 Å thick.

8. The fracture path of these composites is not a random one, but it is governed by an oxide layer, rich in Mg (predominantly), Al and O with C having a "graphitic" nature present. The oxide layer is in the form of mixed crystalline ternary or quarternary oxides of unknown stoichiometry as well as a complex oxide glass.

END

JAN.

1988

DTIC